A STUDY ON VARIOUS FABRICATION ROUTES FOR PREPARING MULTILAYERED CUBIC BORON NITRIDE FILMS AND SP^3-LIKE BORON NITRIDE FILMS

SUBMITTED BY

WONG SING FAI

"A thesis submitted in partial fulfillment of requirements for the Degree of Doctor of Philosophy"

AT THE DEPARTMENT OF APPLIED PHYSICS

The Hong Kong Polytechnic University

October 2005

CERTIFICATE OF ORIGINALITY

I hereby declare that this thesis is my own work and that, to the best of my knowledge and belief, it reproduces no material previously published or written, nor material that has been accepted for the award of any other degree or diploma, except where due acknowledgement has been made in the text.

Wong, Sing Fai

Abstract

Cubic boron nitride (cBN) has a sp^3-bonded structure which leads to excellent mechanical properties. Though cBN-rich films have been successfully fabricated by using many ion assist techniques, the adhesion of the films on most substrate materials is still unsatisfactory. The maximum sustainable thickness of cBN-rich films with good adhesion is widely reported to be around 200 nm, so many practical applications of cBN coatings are hindered. The poor adhesion arises from (i) the appearance of a weak sp^2-bonded BN layer prior to the cBN nucleation; (ii) high compressive stresses evolved in the deposits; (iii) possible existence of excessive B causing reaction of the film materials with the moisture in the atmosphere.

In this study, we designed a series of deposition schemes in a logical sequence, in order to explore whether some of the above problems can be solved, or other structural forms of BN with potential applications can be made, and to gain more fundamental understanding on the mechanisms controlling the growth of various phases observed in the films prepared. Various fabrication processes were employed according to the following sequence:

1. A single-step process was used to find out the maximum tolerable thickness of the cBN-rich films prepared by our own system, compare with the widely reported result, i.e. 200 nm.
2. A multilayered deposition process was used to add a thick gradient sp^2-bonded BN buffer layer in order to support a thicker cBN-rich layer on top.

3. An advanced multilayer process with subsequent annealing process was used to remove the sp^2-bonded buffer layer through solid state reaction with a pre-deposited zirconium (Zr) metal layer.
4. Ion assist deposition at unheated condition was used to create composite BN films containing sp^3 nanoclusters in a sp^2-bonded matrix.

Experimentally, a dual ion beam deposition (DIBD) technique was used to prepare samples. In this technique, one ion beam was generated to sputter a B target, while another ion beam was produced to bombard the growing film surface. To characterize the film structure, we employed infrared absorption (IR) to analyse the phase composition; X-ray photoelectron spectroscopy (XPS) to determine the elemental composition and chemical state; and transmission electron microscopy (TEM) to directly observe the microstructure. Electron energy loss spectroscopy (EELS) was conducted by both XPS and TEM techniques. For the EELS(XPS) analysis, a new method was developed to quantitatively determine the volume fractions of different BN phases in a film sample. It was assumed that a BN film normally consisted of a cBN phase, a hexagonal BN (hBN) phase, and a highly disordered amorphous BN (aBN) phase. We found that the EELS(XPS) method was more effective in detecting the nano-sized sp^3 structure in a film, compared to the IR absorption technique. The EELS method conducted by TEM system can identify whether the BN material in a tiny region ($\approx$ 1 nm) is mainly sp^2-bonded or sp^3-bonded.

Results obtained from Process 1 showed that the maximum thickness of cBN-rich film obtainable with our DIBD system (183 nm) was consistent with that widely reported in the literature, suggesting that new processes were required to produce

thicker cBN-rich films. The application of Process 2 verified our idea that the addition of a thick gradient sp^2-bonded BN buffer was relatively deformable, and hence some stresses would be released during the growth of a cBN-rich top layer so as to allow a thicker cBN-rich layer with acceptable adhesion to grow on top. The optimum assist beam energy was identified to be 450 eV (at 680^{o}C), and a simple model taking account of the equilibrium between the generation and annihilation of defects was applied to explain the results. Process 3 showed the effectiveness of removing the sp^2-bonded layer, and resulted in a boride / cBN-rich layer film on tungsten carbide substrate. Process 4 produced composite BN films containing sp^3 nanoclusters embedded in a sp^2-bonded matrix. The IR technique was not sensitive enought to detect sp^3 nanoclusters, but their presence was verified by the results of high resolution TEM analysis, EELS(XPS) analysis, EELS(TEM) analysis and hardness measurements. In particular, the sp^3 content can be over 30 vol.%, with a hardness of 20 GPa compared to 0.9 GPa of a pure sp^2-bonded BN. The influences of the assist beam energy and substrate temperature on the generation of the sp^3 nanoclusters were investigated in detail. Interestingly, by observing the annealing effects on the structure and mechanical properties of the films, we concluded that the volume fraction of the sp^3 phase dropped with increasing annealing temperature, verifying that some of sp^3 nanoclusters were metastable. Two theoretical models were applied to describe the formation mechanisms of these nanoclusters.

List of Publications

Wong, S.F, Ong, C.W., Pang, G.K.H. and Baba-kishi, K.Z. “Effects of the insertion of a thick *sp*^{2} buffer layer on the adhesion of *c*BN-rich film”. *Journal of Vacuum Science and Technology A,* Vol. 22, pp. 676-682 (2003).

Wong, S.F., Ong, C.W., Pang, G.K.H, Li, Q. and Lau, W.M. “Removal of sp^2-boron nitride transition layer in the growth of cubic boron nitride films”. *Diamond and Related Materials,* Vol. 13, pp.1632-1637 (2004).

Wong, S.F., Ong, C.W., Pang, G.K.H., Li, Q. and Lau, W.M. “Complexity of the microstructure evolution for optimization cBN growth in a four-step ion-assisted deposition process”. *Thin Solid Films,* Vol. 489, pp.63-67 (2005).

Ma, D., Ong, C.W. and Wong, S.F. “New relationship between Young’s modulus and nonideally sharp indentation parameters”. *Journal of Materials Research,* Vol. 19, pp.2144-2151 (2004)

Ma, D., Ong, C.W., Wong, S.F. and He, J. “New method for determining Young’s modulus by non-ideally sharp indentation”. *Journal of Materials Research,* Vol. 20, pp.1498-1506 (2005)

Ma, D., Ong, C.W. and Wong, S.F. “Evaluation of macro-hardness from nanoindentation tests”. Journal of Materials Science, Vol. 40, pp.2685-2687 (2005).

Acknowledgements

I would like to acknowledge Dr. C. W. Ong, my chief supervisor, for his invaluable advice and his close supervision in my study period. I also gratefully acknowledge for his suggestions in editing the content and organization of this thesis.

I am especially indebted to Prof. W. M. Lau, Leo of The Chinese University of Hong Kong for fruitful discussions with him and his enlightening suggestions on my research work.

I would like to greatly thank Dr. K. H. Pang, Geoffery of this university and Prof. Li Quan of The Chinese University of Hong Kong. They taught me how to prepare TEM samples and worked out fruitful TEM pictures. I would also like to thank Mr. B. Zheng of The Chinese University of Hong Kong for his assistance in performing the XPS experiments.

Thanks are also due to Dr. D. J. Ma for his assistance in analysing the results of nanoindentation. Moreover, I would like to thank Mr. M. N. Yeung of Materials Research Centre and the staff of our department for their technical support.

The work described in this project was substantially supported by a grant from the Research Grants Council of the Hong Kong Administrative Region (Project No.: PolyU 5141/00E, account code: B-Q362).

Table of contents

Chapter 1

Introduction

1.1 Background

Cubic boron nitride (cBN) is a material not existing in nature, but it was first artificially synthesized in 1957. It usually exists in powder form, and it has been available commercially for grinding applications and making cutting inserts for metal work since 1970 [Hugh, 1996].

Boron and nitrogen atoms can combine with two different hybridizations, namely sp^2- and sp^3-hybridizations. The corresponding coordination numbers are 3 and 4 respectively. In the B-N material system, there are two crystalline sp^3-bonded phases, namely cBN and wurtzite BN (wBN) (Fig. 1.1). cBN has a zinc-blende structure, analogous to diamond. The wBN structure has a hexagonal lattice structure. Referring to Fig.1.1, one may regard both structures as stacks of buckled BN planes, but with different registrations. For cBN, the planes are arranged with their common normal in the [111] direction of the zinc blende structure; and that of the wBN is in the [0001] direction of the hexagonal structure. Importantly, they are sp^3-bonded and so have similar mechanical properties like high hardness. On the other hand, there are two sp^2-bonded crystalline phases in the B-N system, i.e. rhombohedral BN (rBN) and hexagonal BN (hBN) consisting of graphic planes arranged in the “A B C” sequence and “A B A” sequence respectively (Fig. 1.1). In particular, the hBN is structurally equivalent to graphite. Since the basal planes are linked by weak van der

Waals force, these phases are much softer than the sp^3-bonded phases. The structure of BN films is more complicated, which commonly show some deviations from the above standard phases. The first is the concept of turbostratic BN (tBN), which refers to a sp^2-bonded structure consisting of graphitic planes stacking together with random rotation about the c-axis. The second is the concept of amorphous phase (aBN), which refers to a highly disordered sp^2-bonded structure.

sp^3-bonded BN	**sp^2-bonded BN**
cBN: 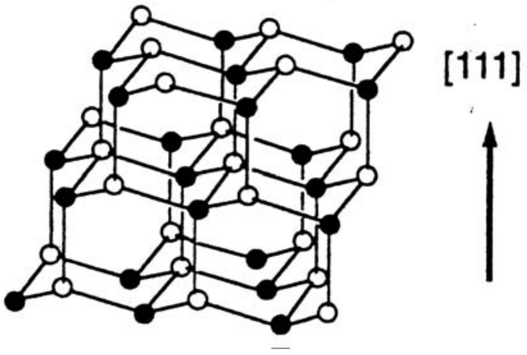 	rBN: 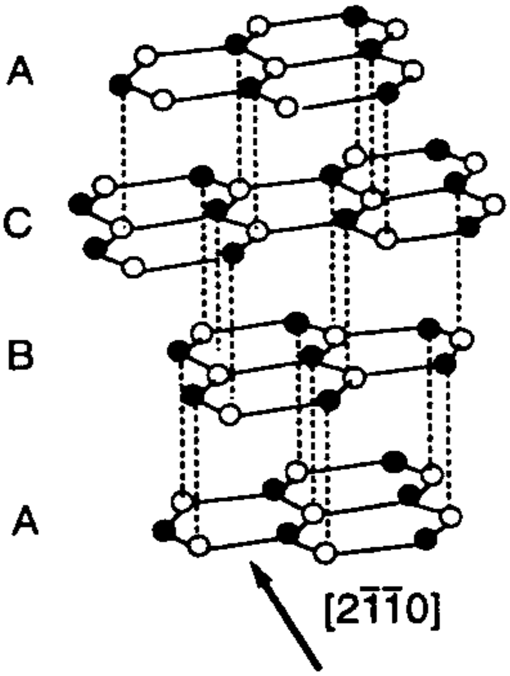
wBN: 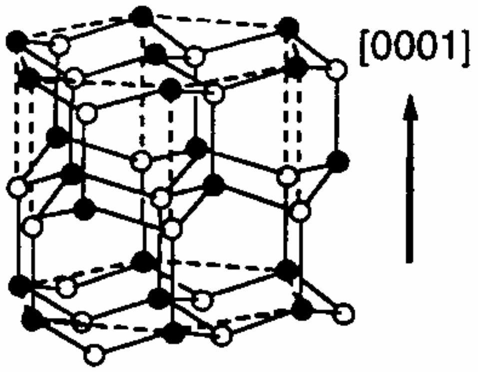 	hBN: 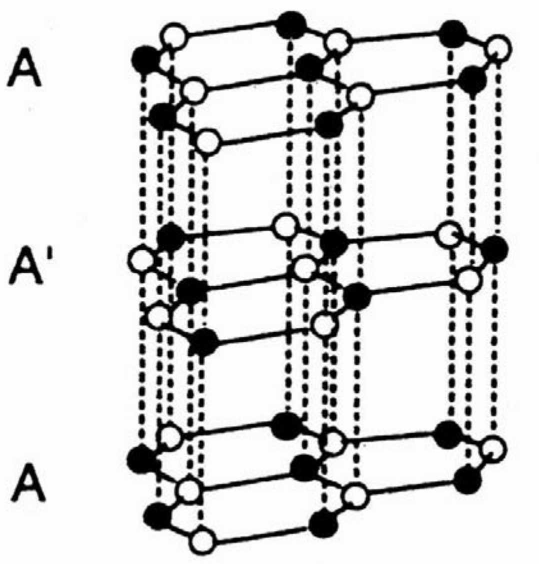

Fig. 1.1 Structures of the sp^3-bonded cBN, wBN and sp^2-bonded rBN, hBN [Mirkarimi, 1997]

Like other superhard materials, there is a great interest in fabricating cBN films to serve as surface protective coatings on work pieces of various shapes. Although a cBN-rich coating is not as hard as diamond, its chemical inertness is high enough to make it more attractive than a diamond coating in some important applications [Riedel, 1994]. This suggestion is based on the fact that a cBN cutting insert remains chemically stable and does not react with iron-containing work pieces in air up to 1300^{o}C [Mirkarimi, 1997]. On the contrary, a diamond cutting insert is readily oxidized in air at 600^{o}C or above, and the carbon atoms would diffuse into ferrous work pieces with a considerable high speed and react with the iron atoms [Riedel, 1994]. Considerable efforts have been made to find the conditions for synthesizing high-quality cBN-rich coatings. Nowadays, high-quality cBN-rich films have been successfully prepared by many physical vapour deposition (PVD) techniques, but it is widely reported that samples with thicknesses exceeding 200 nm peel off very rapidly from the substrate [Li, 2002; Matsumoto, 2000; Keunecke, 2001; Kulisch, 2000; Walter, 1999]. This problem hinders many potential applications of cBN films in the cases where thickness of around 1 μm or above is required. Although a number of carefully designed methods has been employed to make relatively thick cBN films, the methods are still rather tedious, and unfavourable for mass production.

It is widely recognized that there are basically three reasons responsible for the poor adhesion of cBN-rich films on substrates. Firstly, ion beam bombardment is found to be necessary for assisting the formation of the cBN phase. According to the stress model, ion bombardment has the effect of creating compressive stresses in the deposits so as to force the sp^2 structure to convert into the sp^3 structure. However, the ion-induced stresses could be accumulated to such an extent that the film itself cannot sustain and result in peeling off. Secondly, a soft sp^2-bonded layer is commonly found to appear prior to the nucleation and growth of the cBN phase [McKenzie, 1991]. Such an interfacial layer would be a weak link between the cBN-rich top layer and the substrate. Thirdly, according to the suggestion of Kim *et al.* [Kim, 1998], residual boron atoms on cBN films surface would react with moisture via the following reaction:

$$\frac{13}{2}O_2 + 8B + H_2O \rightarrow 2[(B_2O_3)_2(OH)], \quad \Delta G = -2800 \text{ kJ / mol.}$$

Dangling bonds are created by the excessive boron atoms at the film surface, and tend to react with oxygen. The reaction would cause volume expansion and additional compressive stresses are induced to speed up the delamination of the film from substrate. This conjecture is supported by the fact that cBN films are more stable in vacuum or dry air comparing to the case in atmosphere [Inagawa, 1989]. Cardinale *et al.* [Cardinale, 1994] placed cBN films in different humidity environment and found that the films under high humidity environment would delaminate within one day. This verifies that moisture-induced oxidation would affect the stability of cBN-rich films significantly.

In the following, we describe some efforts in preparing cBN-rich films. We stress that adhesion of cBN-rich films thicker than 200 nm is still a problem. More recently, some carefully designed deposition schemes have been employed, but most of them are rather tedious and unpractical in real application.

Weissmantel *et al.* [Weissmantel, 2001] used ion-assisted pulsed laser deposition technique to synthesize cBN-rich film. In this technique, a KrF excimer laser was used to ablate an hBN target. Concurrently, an ion beam containing both nitrogen and argon ions was generated to bombard the deposits. cBN-rich films with a thickness of 350 nm could be formed. The Vickers microhardness was measured to be 42 GPa. The coating rate was 50 nm min^{-1}. With this configuration, the deposition rate and ion flux can be independently controlled. However, the area with uniform thickness on the film is very small. This restricts extensive use of this technique in commercial production.

Radio frequency (RF) and direct (DC) magnetron sputtering were used by Schütze *et al.* to fabricate cBN-containing films [Schütze, 1995]. He demonstrated that films containing 60 vol.% of cBN phase could be deposited on Si substrate. Either hBN or B_4C was used as the target for the deposition. A mixture of Ar and N_2 gases is commonly used as the sputtering gas in reactive sputtering processes. Johansson *et al.* [Johansson, 1996] demonstrated that films containing 80 vol.% of cBN could be produced with DC magnetron sputtering. A Kaufman-type ion gun and/or electron cyclotron resonance (ECR) ion source were employed to provide energetic particle bombardment on the growing film surface to assist the formation of the cBN phase. Mirkarimi *et al.* [Mirkarimi, 1997] used this method to fabricate cBN-rich films with thickness around 0.7 μm. The hardness of their samples was found to be 60-70 GPa.

The use of DC-bias-assist chemical vapor deposition (CVD) system showed a breakthrough to fabricate thick cBN-rich films of 20 μm thick [Matsumoto, 2001]. The cBN fraction contained in the films was measured to be 90 vol.%. The coating rate was as high as 0.3 μm min^{-1}, which is 10 times higher than that of other PVD or CVD methods used for the fabrication of cBN-rich films. The extremely high coating rate of this technique and high quality of cBN films produced indicate that this method has great potential in commercial application. Nevertheless, the drawback of this technique is the use of hazardous reactant gases, and the coating is highly non-uniform.

Recently, different deposition schemes have been designed in order to fabricate thick cBN films on silicon substrates. Techniques such as the introduction of buffer layer [Keunecke, 2001; Murakawa, 1990], lower substrate bias in magnetron sputtering [Li, 2002], bombardment with high assist ion energy during growth [Ulrich, 1995], reduction of assist ion energy after the complete formation of a continuous cBN template layer [Litvinov, 1997; Litvinov, 1999], high substrate temperature above 1000°C [Litvinov, 1997; Litvinov, 1999; Matsumoto, 2000], post-annealing [Donner, 1998], post-ion irradiation with energetic ions [Widmayer, 1997], and addition of foreign elements [Zhao, 1997] were used. Hybrid approaches were also proposed to combine some of the above techniques [Mirkarimi, 1997]. These ideas were developed with the intention for releasing the stresses and strengthening the binding capacity between the substrate and the cBN-rich layer.

Besides employing the approaches of compositional modifications, more recently, structural modification has emerged as an important approach for promoting the mechanical properties of coatings. Distinctive examples are to make films with nano-layered superlattice structures and nanocomposite structures. Materials with hardness exceeding 40 GPa were achieved [Sinn, 1992; Helmersson, 1987; Makowiecki, 1990; Brazhkin, 2002; Anderson, 1999; Weertman, 1999]. Some other novel properties, like high oxidation resistance and wear resistance are obtained. The most widely studied film materials include Ti–Si–N [Veprek, 1995;

Rebouta, 2000], Ti–Si–Al–N [Carvalho, 2001], Zr–Y–N [Musil, 2000] and W_2N – Si_3N_4 systems [Vepřek, 1996] etc. Vepřek *et al.* claimed that a film containing nc-TiN/a-Si_3N_4/a- and nc-$TiSi_2$ nanocomposites had hardness of 80-100 GPa [Vepřek, 2000]. The reason for these structures to give such a high hardness is that the presence of the boundaries between the nanograins can block the propagation of cracks initiated in the materials. This effect becomes prominent only when the size of the nanograins is less than 10 nm [Vepřek, 1995; Chen, 2001]. Related to the B-N system concerned in the present study, the synthesis of BN film with nanocomposite structure composed of sp^2 and sp^3 phases may not be impossible. The realization of such a conception has not been reported in literature.

1.2 Scope of Study

Recognising the superior mechanical properties of cBN and the huge commercial potential of cBN films, we conducted the present project with the aim of implementing several deposition schemes designed in a logical sequence. We intend to fabricate thick cBN-rich films or films containing sp^3 BN clusters with acceptable mechanical properties. In addition, the material structures and properties of the films deposited with different schemes were characterized, and the formation mechanisms of different features observed in the materials were discussed.

The first deposition scheme used a single-step process, in which all the deposition parameters were not altered, to prepare a serious of samples with different thicknesses. The purpose of employing this scheme is to verify whether the maximum sustainable thickness of cBN-containing films produced by our system is close to that reported by other authors.

With the above result as a reference, we employed a second deposition scheme in which a thick sp^2-bonded BN gradient buffer layer was depoisted on the substrate prior to the deposition of a cBN-rich top layer. This scheme was proposed based on the expectation that the thick and soft sp^2-bonded BN buffer layer would have some degree of deformability such that it can release some stresses in the cBN-rich layer deposited on top.

On the basis of the above results, a third scheme was employed, which was a multilayered approach with some subsequent post-treatments. First, a zirconium layer, a thick sp^2-bonded BN gradient buffer layer and a thick cBN-rich top layer were deposited in sequence (Fig.1.2). A high-temperature annealing process was used to promote the reaction between the zirconium layer and the soft sp^2 buffer layer to form a hard boride. Some residual stresses are expected to be released. Finally, the film surface was irradiated with nitrogen ions, with the intention of activating any possible excessive boron to form boron nitride, so as to reduce the reactivity of the material with moisture.

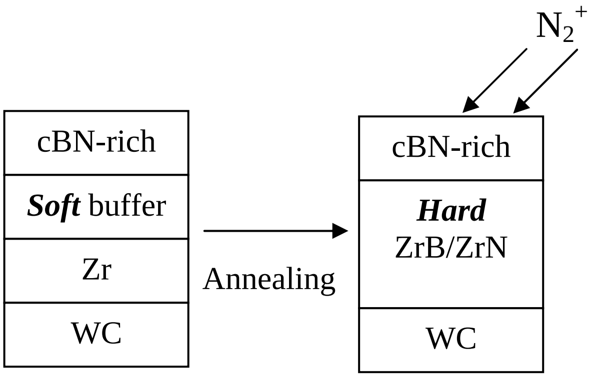

Fig. 1.2 A schematic diagram of the third scheme.

The last scheme is entirely a different approach from all the above. It is a single-step process conducted on unheated substrates. This scheme was inspired by some facts, which implied the possibility of forming sp3-bonded nanoclusters in a sp^2-bonded BN matrix. The first is the accidental finding of some sp^3 nanoclusters in the sp^2-bonded BN gradient buffer layer during the implementation of the second and third schemes. The second clue comes from the BN phase diagram, which indicates that low temperature environment favours the formation of the sp^3 phase. With the substrate being unheated and under ion bombardment, we hope that a nanocomposite structure containing sp^3 nanoclusters embedded in a sp^2-bonded BN matrix can be obtained (Fig. 1.3). With the inclusion of the sp^3 phase, we expected the hardness of the films would be prominently higher than that of a pure sp^2 film. If successful, these films would have advantages compared to a polycrystalline cBN film, such as a simpler deposition process and a lower deposition temperature to save the cost of fabrication. With the presence of some sp^2 content, the stress is expected to be lower than that of a polycrystalline cBN film, but the hardness may not be as high as a cBN polycrystalline film.

Experimentally, a dual ion beam system was used for the sample fabrication. The films structure was characterized by using Fourier transform infrared absorption (FTIR) spectroscopy, X-ray photoelectron spectroscopy (XPS), cross-sectional transmission electron microscopy (TEM), and electron energy loss spectroscopy (EELS) with both the XPS system and TEM system. The mechanical properties of the film samples were determined by using nanoindentation and stress measurements. In particular, a new method was developed by observing the EELS data of the N 1s photoelectrons collected with the XPS system to give quantitative phase composition analysis. The volume fraction of the sp^3 nanoclusters in the films deposited on unheated substrates can be determined.

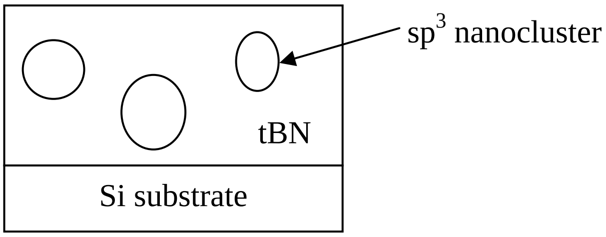

Fig. 1.3 The final structure of the second route for fabricating applicable BN film

Due to the complexity of the material system, we expect the microstructure of the BN films would strongly depend on the deposition conditions. The parameters most likely to give greatly influence on the film structure are the substrate temperature and assist ion beam energy. Hence, in this part of the study, the films are correlated to the deposition conditions, and the possible physical mechanisms resulting in the film structure are discussed.

Chapter 2

Sample Preparation and Characterizations

2.1 Sample Preparation

In this study, BN films were synthesized by using a dual ion beam deposition system (DIBD). In this technique, one ion gun is used to generate an ion beam to sputter a target, whereas another gun is used to produce an assist ion beam to irradiate the substrate. The assist beam is used for pre-cleaning the substrate; injecting nitrogen for formation of nitride; and bombarding the growing film for introducing stresses which are shown to be necessary for the formation of the sp^3 structure with physical vapour deposition (PVD) techniques. DIBD technique is distinctive for synthesizing new materials because it allows the beam energy and current to be varied independently in broad ranges, and so can provide very stringent preparation conditions. As illustrated in Fig. 2.1 (a), our DIBD system has a vacuum chamber, which can be pumped down to a base pressure of 10^{-6} Torr. The system is evacuated with a turbo-molecular pump backed with a mechanical rotary pump. The chamber is equipped with two 3-cm Kaufman ion guns (Ion Tech. 3-1500-100).

During deposition, 99.99% purity argon gas was admitted into the sputtering gun with a flow rate of 30.0 standard cubic centimetres per minute (sccm). An argon ion (Ar^+) beam (sputtering beam) was then generated and directed to sputter a 4-inch target. For most of the films, the sputtering beam energy and current were set at 1200 eV and 70 mA, respectively. The incident angle of the sputtering beam is 45° from the target normal.

Concurrently, the assist beam containing nitrogen and argon ions was directed to bombard the growing film surface. The ranges of assist beam current and energy were variable in the ranges of 20 - 40 mA and 100 - 550 eV respectively. The use of assist ion beam was generally recognized to be necessary for the growth of the sp^3-bonded cubic BN phase, and the microstructure was found to be very sensitive to the setting of the assist beam. The incident angle of the assist beam is 16° from the normal of the substrate. This angle has been optimized for minimizing resputtering of the deposits.

The target holder can be rotated about an axis by a motor. For the preparation of multi-layered samples, two different target materials were mounted on two opposite sides of the holder for sequential sputtering without breaking the vacuum [This process is illustrated schematically in Fig. 2.1 (a)]. In addition, the target holder was water-cooled to avoid cracking of the targets due to the heating generated during sputtering.

Two substrate materials were used. The first was 525 μm-thick (100) silicon (Si) wafer. Si is infrared (IR) transparent and so is favourable for the observation of the IR absorption of a film deposited on it. The second was tungsten carbide (WC) slice, which was used in order to evaluate the performance of BN films made on a real cutting tool material. The WC slices were cut from a ceramic cutting tool (Sandvik, Coroment P35) by a precision diamond saw (Struers Accutorn-50). They were made to be about 300 μm thick, and were then polished manually with 0.25 μm diamond paste. The slices were then cleaned by ethanol and acetone. The organic residues were removed in oxygen plasma in a plasma processing reactor (Bromson / IPC, series 2000) at a power setting of 300 W for 10 minutes.

Now we describe the substrate holders. Two substrate holders were fabricated and used for the deposition of the film samples. The first is water-cooled for preparing the samples at a low temperature. With this system, the substrate temperature was normally maintained at 80°C under ordinary ion assist conditions. Another substrate holder is equipped with a heater instead of water-cooling system. When the heater was not turned on, under normal ion assist conditions, the substrate temperature was stabilized at above 100 – 210°C. By turning on the substrate heater, substrate temperature can be varied to a maximum value of 850±1°C. The temperature was automatically stabilized with a proportion-integration-differentiation (PID) temperature controller (Omega, CN4400) in conjunction with a power regulator (Shimaden, PAC26C416-021P01410). Fig. 2.1 (b) shows the block diagram of the temperature controlling system. Both of the substrate holders can be rotated during deposition to ensure the uniformity of the film thickness.

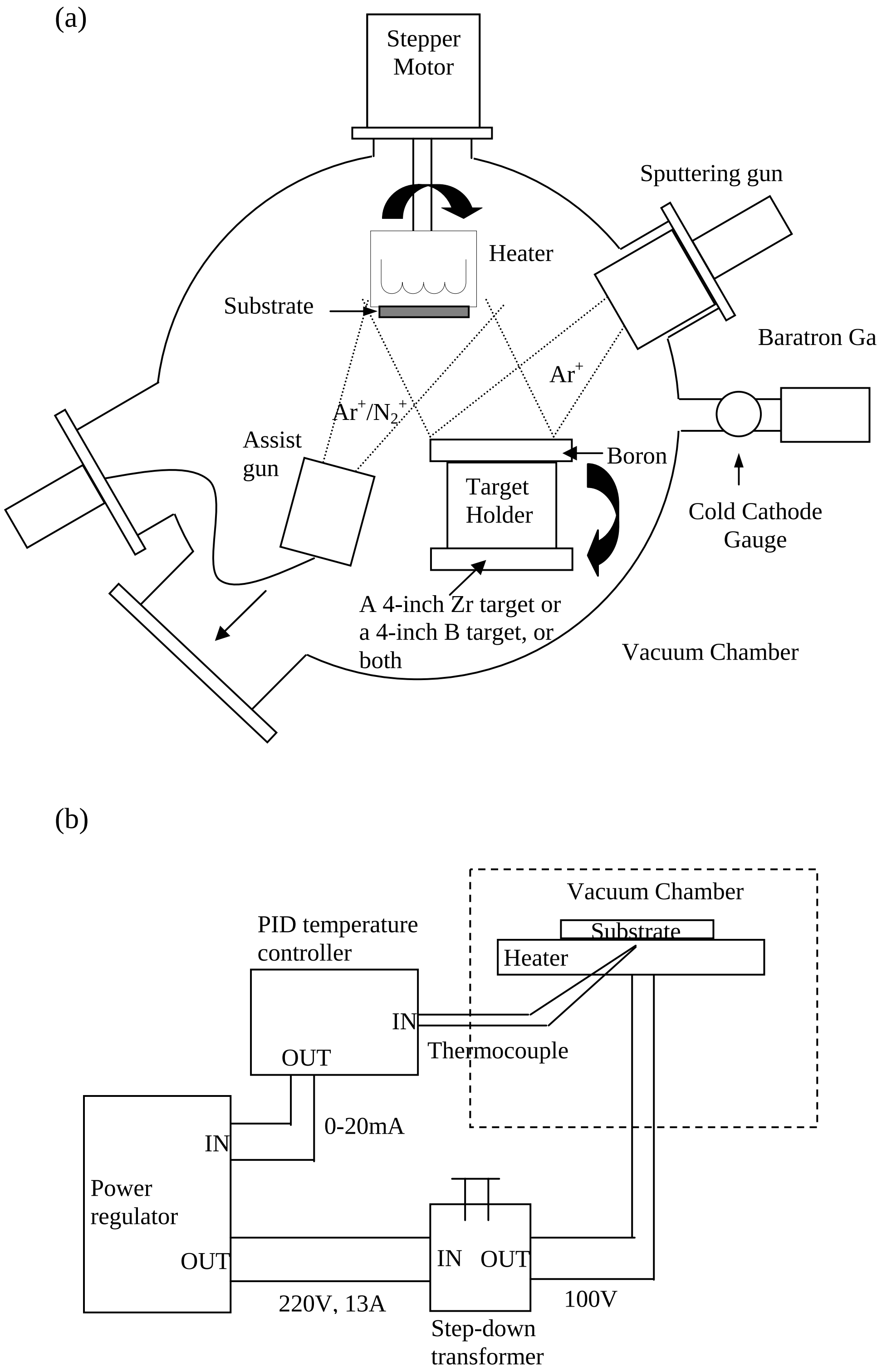

Fig. 2.1(a) Schematic diagram of the dual ion beam deposition (DIBD) system.
(b) Schematic diagram of the substrate temperature controlling system.

2.2 Structural and Compositional Characterizations

In this section, the experimental techniques and set-ups for the analyses of the structure and elemental composition of the film samples are described.

2.2.1 Film thickness measurements

A surface profiler (KLA-Tencor P-10) was used to measure the film thickness. This system is designed to detect a small vertical displacement of a stylus when it is driven to climb across a step, such as the edge of film relative to the substrate surface (Fig. 2.2). The vertical movement is converted into an electrical signal which reflects the film thickness by means of some calibration procedures. The resolution of the measurement is in the order of 0.1 nm.

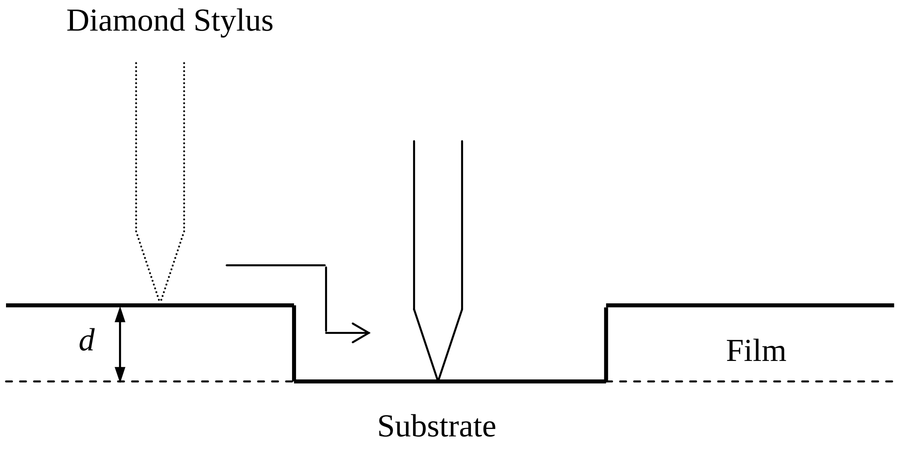

Fig. 2.2. The principle of film thickness measurement by using a surface profiler

2.2.2 Transmission electron microscopy

Transmission electron microscopy (TEM) was used to investigate the microstructures of some selected samples. Both micrographs of cross sections and electron energy loss spectra (EELS(TEM)) of some selected film samples were analyzed.

Two TEM systems were used for the study. The first one is a JOEL 2010 system with a LaB_6 electron source. Electrons were emitted from the electron source and accelerated to 200 keV. They were diffracted and formed an image or diffraction pattern after passing through the samples. The theoretical resolution and electron beam size are 0.194 and 0.5 nm. The maximum magnification is 1.5 million times. The smallest aperture size used for producing images was 120 nm. Dark-field imaging technique was employed to map the distribution of a specific group of grains with a certain orientation.

Another TEM system (JEOL 3000 FEG-TEM) is equipped with a field emission electron gun. The electron beam can be focused to a size in the range of 2 – 100 nm. The beam energy for this study is about 300 keV, with a resolution of ~ 1 eV. The beam quality is good enough to provide high resolution images to show detailed microstructure. The system is equipped with a Gatan imaging filtering (GIF) system for analyzing the electron energy loss spectrum (EELS(TEM)). From the EELS(TEM) data, one can distinguish the sp^2-bonded BN phase and sp^3-bonded BN phase in a region with a dimension around a few nanometres. This information is very important in analyzing the formation mechanisms of the sp^3-bonded structure as seen in the following chapters.

To prepare a TEM sample, two small cross-sectional slices were first cut from a sample (Fig. 2.3 (a)). They were then glued together face-to-face (Fig. 2.3 (b)). The specimen was then thinned by manual grinding, followed by double-sided dimpling with a Gatan 656 Dimpler. It was then transferred to a copper grid and further thinned by using an ion milling system (Gatan 691 Precision Ion Polishing System) until a thickness of about a hundred nanometres was achieved. In this process, the beam energy was reduced to 3.0 keV and the incident angle of the milling ion beam was varied progressively from 8 to 4 degrees. Lower energy and smaller incident angle were employed in the last step to reduce any undesired damages of the specimen.

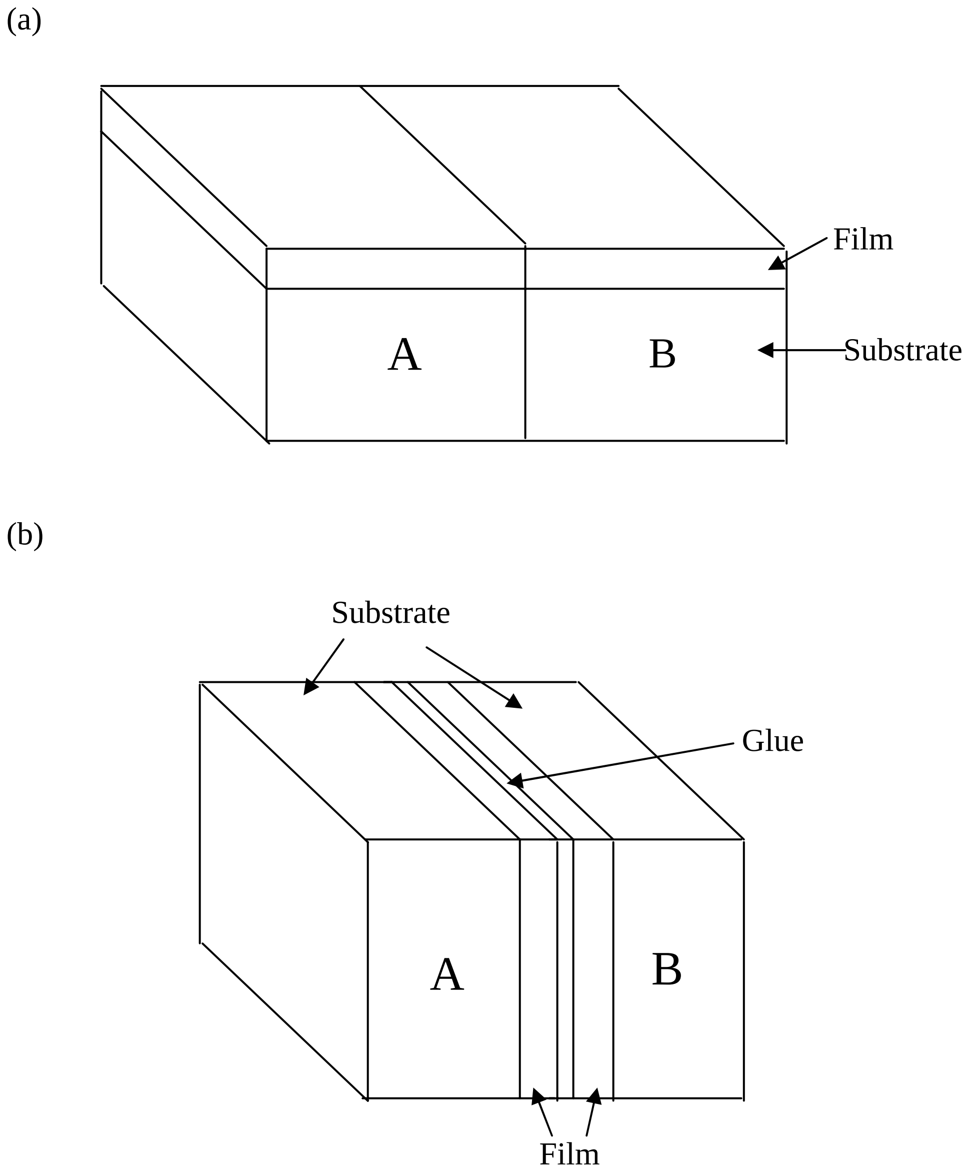

Fig. 2.3 (a) Sample cut into two pieces
(b) A TEM sample formed by gluing two slices face-to-face.

2.2.3 *Compositional analyses by x-ray photoelectron spectroscopy*

A PHI Quantum 2000 system was used to record the XPS spectra of our samples for compositional analysis. Measurements were conducted in an ultrahigh vacuum environment at a pressure of 10^{-9} Torr. X-ray photons are generated from an X-ray source with an aluminium (Al) anode being bombarded by 15 keV electrons. X-ray photons with a characteristic energy of $h\upsilon$ = 1486.6 eV are emitted. The detected area is roughly around 100 x 100 μm^2.

In principle, when a photon hits a core electron of an atom, the core electron can be knocked out and escapes with a kinetic energy equal to:

$$U_k = h\upsilon - U_B - \Phi \qquad (2.1)$$

where U_B is the binding energy of the electron, and Φ is the work function of an electron energy analyser. The value of Φ can be obtained according to some calibration procedures. U_k is detected experimentally by an electron energy analyser, such that U_B can be determined from equation (2.1). The value of U_B should correspond to the characteristic binding energies of different elements, such that the types of the elements contained in the sample can be identified. To conduct a quantitative elemental analysis, considering a typical BN film as an example, the photoelectron spectra of the B 1s, N 1s, C 1s, O 1s were collected. After the background was subtracted from the spectra, the areas under the spectrum lines were integrated by means of software MultiPak V6.0A (Physical Electronics, Inc.).

The relative atomic percentage of a certain kind of atoms labelled by "i" is:

$$C_i = \frac{A_i / S_i}{\sum_j A_j / S_j} \tag{2.2}$$

where A_i is the area under the corresponding spectrum line after removing the background. The index "j" is varied to scan through all the elements detected. S_j's are the sensitivity factors, reflecting the relative intensities of XPS signals generated by different types of elements under the same excitation conditions. Their values are determined through standard calibration procedures in the factory. For example, the sensitivity factors of B 1s and N 1s photoelectrons are 0.133 and 0.499, respectively.

If more and more photoelectrons are emitted from the surface of an insulating surface, the surface could be charged up. The surface condition would then affect the energy of the electrons emitted thereafter, and causes substantial shift of the peak positions of the spectrum lines. To diminish this effect, a charge neutralizer is activated during measurement to generate "soft" electrons to compensate the surface charge.

In addition, the system has an ion gun generally used to generate argon ions (Ar^+) for two major purposes. The first is to pre-clean the sample surface since many kinds of absorbents are easily absorbed at the surface. The second is to sputter the materials for depth profile analysis, where data are collected between successive sputtering processes.

The penetration depth of X-ray photon into a solid is in general in the order of a few microns. However, the travelling range of photoelectrons with energies in the range of concern is only as small as a few nanometres, which is actually the escape range of photoelectrons. For this reason, XPS is a surface sensitive analysis technique. Therefore, the surface of a sample must be pre-cleaning before measurements. One standard process is to wash the sample with methanol in an ultrasonic bath. It is then rinsed with deionized water and blown by dry nitrogen. In addition, the surface contamination would be removed in vacuum by sputtering with an argon ions (Ar^+) from an ion gun in the XPS system. In this study, the Ar^+ beam was set at 4 keV and 20 mA, and the sputtering process lasted for 3 minutes.

2.2.4 Chemical state analyses by x-ray photoelectron spectroscopy

The peak position of a photoelectron spectrum is normally determined by referring to a standard reference, such as the peak position of the Au 1s line from pure gold. Nevertheless, it is usually found that the same type of element in specimens of different compositions and structures could give photoelectrons of different binding energies. This is because the atoms are surrounded by different chemical environments in different solids. For example, an N atom has a stronger electron affinity than a B atom, so that in a boron nitride solid, a B1s photoelectron escaping from a B atom would have a higher electric potential compared to that of pure boron. This results in a higher B 1s binding energy of 190.5 eV of boron nitride, comparing to 189.4 eV of that from the elemental boron. Moreover, for a multi-element or multi-phase solid, the same type of atoms could be surrounded by different chemical environments. This would give a spectrum line of more subtle features. It is therefore possible to extract more detailed chemical structure information by deconvoluting the spectrum line into components.

2.2.5. Quantitative analysis of the volume fractions of different BN phases by using XPS electron energy loss spectroscopy

In this study, we developed a method to give quantitative structural phase analysis of a BN film by using electron energy loss spectroscopy collected by XPS system (denoted as "EELS(XPS)"). An EELS(XPS) spectrum of a certain group of photoelectrons (N 1s in this study for example) would contain information on plasmons, which are generated by the photoelectrons travelling in a solid. Each plasmon mode has a characteristic energy related to the structural phase from which it is generated. In most studies, reported in literature, the plasmon data are just used for qualitative structural phase identification. However, in the present study, we employed a more careful approach from which the volume fractions of different structural phases contained in a BN film can be derived according to the features of the whole plasmon spectra.

The method developed in this study is based on the assumption that a boron nitride film is composed of cBN (cubic) phase, hBN (hexagonal) phase and highly disordered aBN (amorphous) phase. The first step of the analysis is to collect three standard EELS(XPS) spectra of N 1s photoelectrons from three reference specimens having the above structures. Then, the EELS(XPS) spectrum of the N 1s photoelectrons of the sample is collected and best fitted by a linear combination of the above three reference. We use the following formula to represent such a fitting, namely, the intensity of the EELS(XPS) spectrum of the sample at a particular energy is:

$$I_{\mathrm{sample}} = a\, I_{\mathrm{cBN}} + b\, I_{\mathrm{hBN}} + c\, I_{\mathrm{aBN}} \qquad (2.3)$$

where I_{cBN}, I_{hBN} and I_{aBN} are those of the three standard samples, and a, b and c are the fitting coefficients. The magnitudes of a, b and c are assumed to be proportional to the volume fractions of the corresponding phases η_{cBN}, η_{hBN} and η_{aBN} contained in the film sample. For the convenience of discussion, they are normalized to have a sum of 1.

In practice, the cBN reference specimen is a single crystal purchased from De Beers with a size of about 0.6 mm, which gives reference data associated with the sp^3-bonded zinc blende structure. The grain was embedded into a copper foil with the (111) face to be exposed for analysis. The standard EELS(XPS) spectrum exhibits characteristic peaks at 27 and 34 eV and a shoulder at about 15 eV (Fig. 2.5) [Trehan, 1990; Loh, 1998; Ilias, 1998; Xu, 1991]. They are attributed to the bulk plasmon loss, and interband transition between the valence band and conduction band respectively [Loh, 1997; Xu, 1991].

The hBN reference specimen is a single crystal purchased from Good Fellow, which is expected to give reference signal associated with the sp^2-bonded hexagonal structure. Different from that of the cBN phase, the EELS(XPS) spectrum of the hBN phase shows a major peak at 25 eV and a shoulder at about 36 eV, which are believed to come from the plasmon loss [Loh, 1997; Loh, 1998; Ilias, 1998; Tarrio, 1989]. A peak at 15 eV is also seen, and is suggested to originate from the σ-σ and π-σ transitions. In addition, a peak at 9 eV is identified, and is related to the π-π^* transition which is regarded as a signature of the presence of sp^2 bonds [Loh, 1997; Loh, 1998].

Material of aBN structure is not available in the market. However, we found that such a structure can be obtained in the form of thin film by using dual ion beam deposition on unheated substrates, ion bombardment at low beam energy (U_{assist} = 100 eV) and low beam current (I_{assist} = 20 mA). We note that the assist beam current should be set at a level to ensure that the B-to-N ratio in the film is very close to 1:1. Low assist beam energy is used to prevent from creating stresses which may cause some orderly arrangement of the atoms. Though the substrate heater was not turned on during deposition, however, the substrate temperature (T_s) was still risen and stabilized at 112°C due to ion bombardment. The sample prepared with these conditions was named as aBN031, and the thickness was measured to be 320 nm. XPS analysis showed that the B-to-N ratio was close to 1:1. The TEM image and the electron diffraction pattern of the sample as shown in Fig. 2.4(a) and (b) are found to be featureless, verifying that the sample's structure is highly disordered. The infrared absorption spectrum shows the characteristic absorption peaks of sp^2-bonded BN. Combining all these results, we assert that Sample aBN031 has a highly disordered sp^2 structure, and is qualified to serve as the reference standard of the "aBN" structure.

One technical concern is that ion bombardment was frequently used in analysis, such as for surface pre-cleaning and sputtering for depth profile analysis. Ion bombardment can alter the structure of the surface, such as converting some sp^3-bonded phase into the sp^2-bonded phase. A method is therefore required to remove any ion-induced damages. According to the experience gained from some tests, it was found that the ion-induced damage can be removed by irradiating the damaged surface with an Ar^+ beam of 500 eV and 180 nA for 10 min; and then 300 eV and 8 nA for 30 min; and finally 100 eV and 11 nA for 60 min.

To analyze a spectrum, the background was first removed according to Tougaard’s method [Tougaard, 1991; Tougaard, 1987; Tougaard, 1998; Tougaard, 1997]. The area under the spectrum line was calculated and normalized to unity. Finally, the best fit to the spectrum line was obtained, and the corresponding fitting parameters a, b and c were obtained to represent the respective volume fractions of the phases.

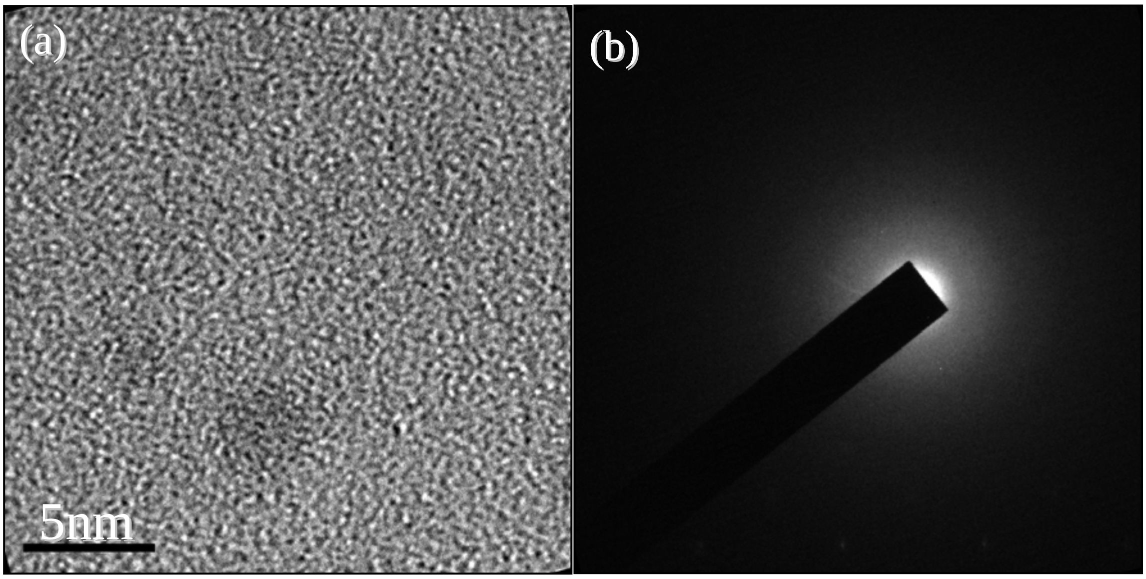

Fig. 2.4(a) HRTEM image and (b) electron diffraction pattern of the aBN reference (aBN031).

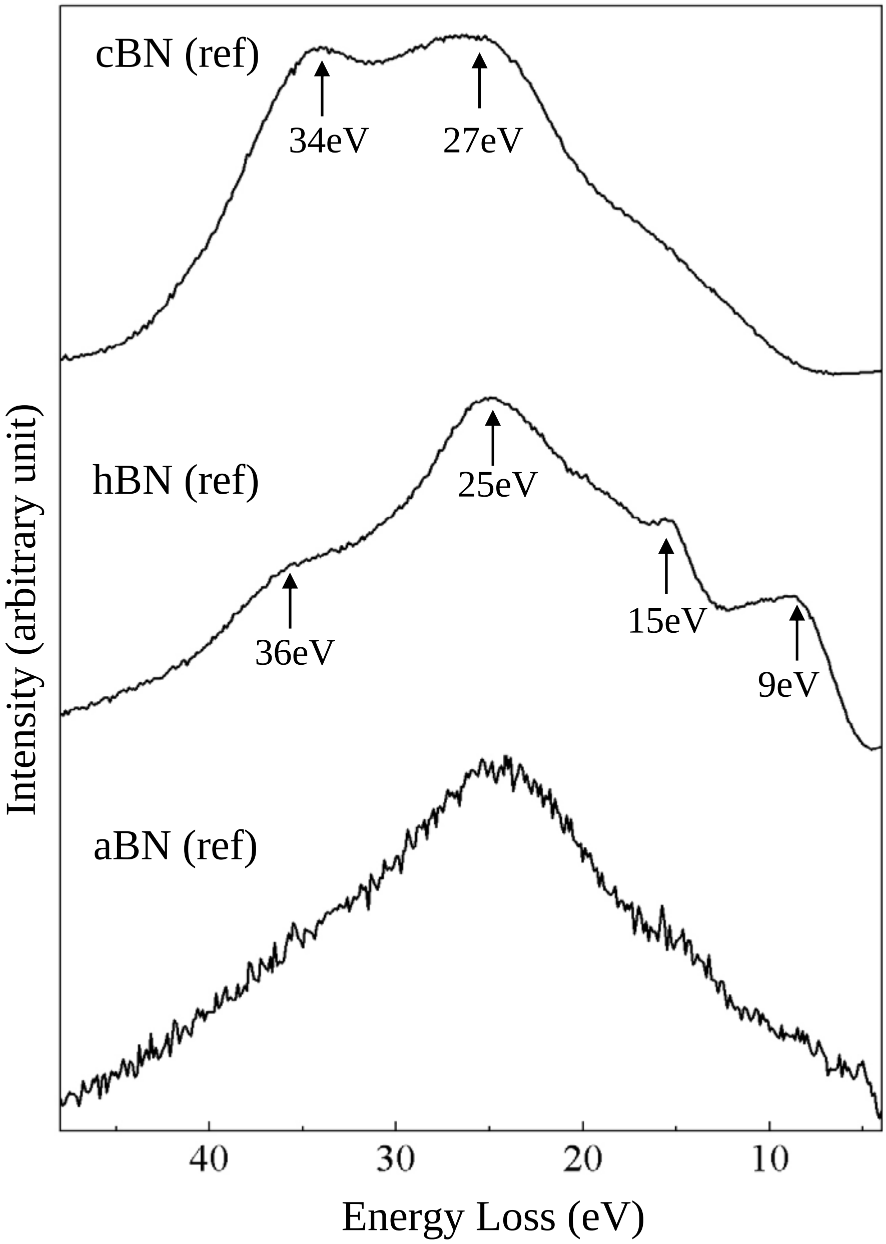

Fig. 2.5 Three reference EELS(XPS) spectra (from XPS N1s photoelectron spectra) of the standard specimens: single crystal cBN, single crystal hBN and aBN film.

2.2.6 Bonding analyses by Fourier transform infrared absorption spectroscopy

Fourier transform infrared absorption (FTIR) experiments in the wavenumber range of 400 – 4000 cm^{-1} (wavelength from 25000 to 2500 nm) were performed by using a Nicolet's Magna-TR^{TM} System Model 750 FTIR spectrometer. Infrared absorption occurs when the frequency of the incident photos matches with the resonance frequency of a vibration mode of chemical bonds formed in the material. It is therefore a very powerful tool to examine the types of chemical bonding in a solid.

The central part of a Fourier transform IR absorption spectrometer is a Michelson interferometer, which structure is presented schematically in Fig. 2.6. The incident beam is split into two beams having similar intensities. A beam is reflected by a stationary mirror and another one is reflected by a movable mirror. Constructive and destructive interference are produced when the movable mirror moves back and forth. The detector measures the variation of the intensity of the IR beam reflected from the stationary mirror. The IR absorption of the sample at different wavelengths can thus be derived.

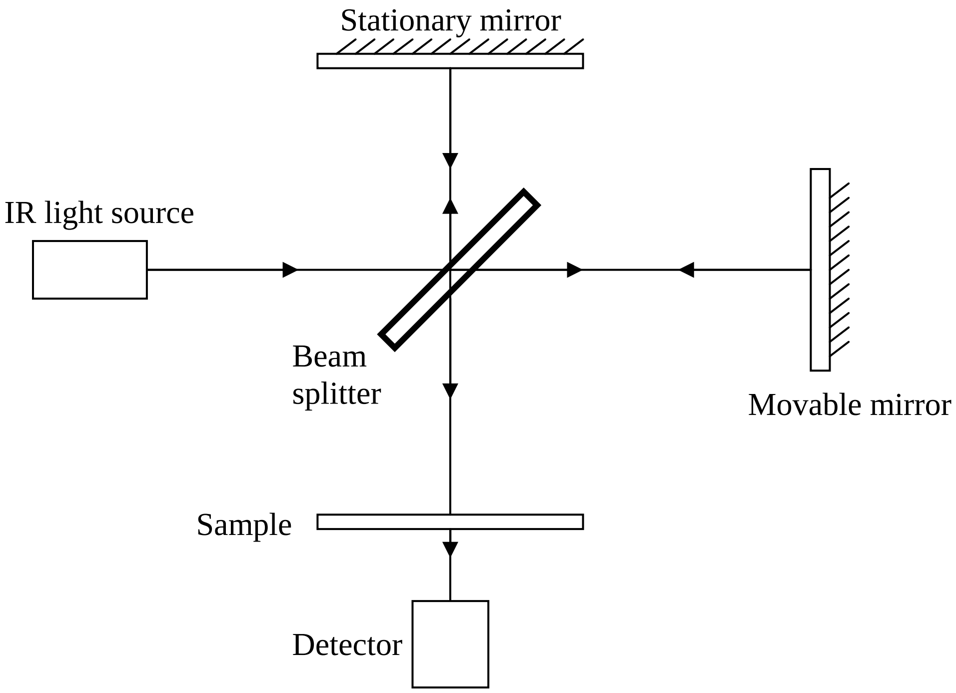

Fig. 2.6 The basic configuration of an FTIR spectrometer.

For boron nitride material system, three characteristic peaks are of most concern. They appear at wavenumbers of 1390 cm^{-1}, 1080 cm^{-1} and 780 cm^{-1}, and are associated with different vibration modes of chemical bonds. The peak at 1080 cm^{-1} is associated with the transverse optical (TO) mode of sp^3-bonded BN (i.e. cBN) structure. Its appearance gives a signature for the formation of the cBN phase in a specimen. The IR peaks 1390 cm^{-1} and 780 cm^{-1} are related to the out-of-plane B-N-B bending mode and the in-plane B-N stretching mode of the sp^2-bonded BN respectively. Moreover, the relative volume fraction of cBN can be calculated by using the relationship:

$$\eta_{\mathrm{cBN-IR}} = \frac{\mathrm{I}_{1080}}{\mathrm{I}_{1080} + \mathrm{I}_{1390}} \tag{2.4}$$

when I_{1080} and I_{1390} are the heights of the IR absorption band at 1080 and 1390 cm^{-1} respectively. This method is widely used to estimate quantitatively the content of the sp^3-bonded phase. Fig. 2.7 gives an example to show how the background of an IR spectrum of a sample is subtracted, and the heights of the IR bands are measured.

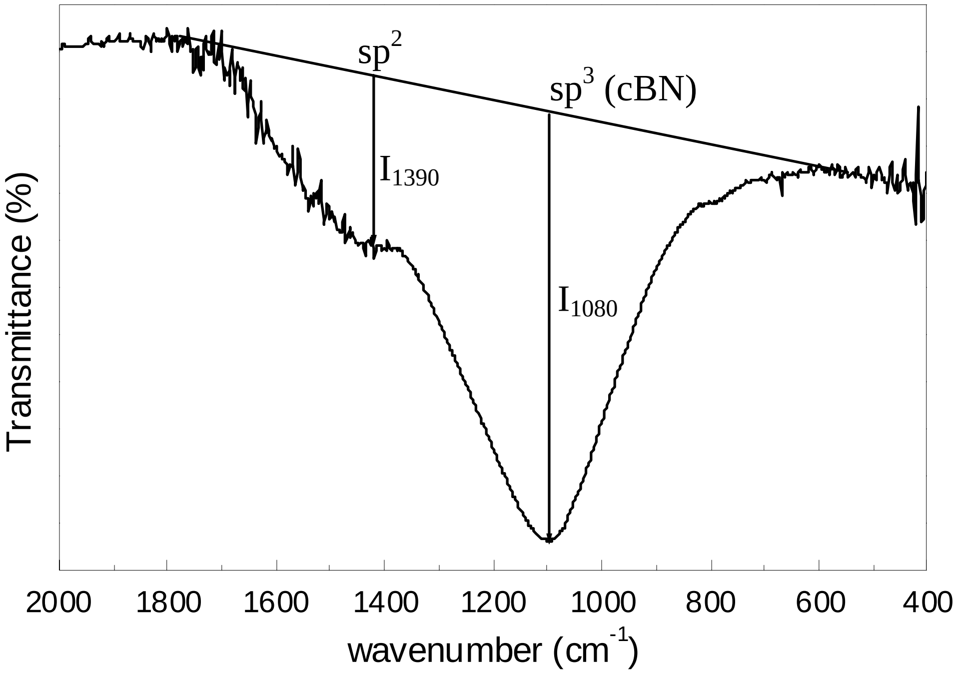

Fig. 2.7 A typical FTIR absorption spectrum of a BN film

2.3 Measurements of Mechanical Properties

2.3.1 Hardness and elastic modulus measurements by nanoindentation

A nanoindentor (Nano Instruments Inc., Model IIs) equipped with a Berkovic 3-sided diamond indenter tip was used to evaluate the hardness (*H*) and elastic modulus (*E*) of the film samples. Each surface of the tip makes an angle of 65.3^{o} to its central axis. The tip was mounted at the lower end of a vertical shaft. The upper end of the shaft has a permanent magnet, which is coupled to an external coil. Load is applied to the shaft by passing a current through the coil. Concurrently, the displacement of the tip head is measured by a capacitive displacement gauge. The displacement of the tip is converted into an electrical signal, which is real-time recorded by a computer. The theoretical resolution of displacement is claimed to be as good as 0.04 nm.

Fig. 2.8 shows the typical features of loading and unloading curves. Referring to the model proposed by Oliver *et al.* [Oliver, 1992], the hardness *H* of a sample is related to the maximum load P_{max} and contact area $A(h_c)$ by the relationship:

$$H = \frac{P_{max}}{A(h_c)} \tag{2.5}$$

The contact area $A(h_c)$ is evaluated at the maximum contact depth h_c at the maximum load. The reduced elastic modulus E_r is obtained by using the following formula:

$$S = \frac{2}{\sqrt{\pi}} E_r \sqrt{A(h_c)} \qquad (2.6)$$

where S is the stiffness equal to the slope of the unloading curve at the maximum load as shown in Fig. 2.8. The reduced elastic modulus E_r is related to the elastic modulus E of the film by the relationship:

$$E_r = \left[\frac{1-\nu_i^2}{E_i} + \frac{1-\nu_s^2}{E} \right] \qquad (2.7)$$

where ν_i and E_i are the Poisson's ratio and elastic modulus of the diamond tip, i.e. 0.07 and 1141 GPa respectively. ν_s represents the Poisson's ratio of the film and is set to be 0.25. The value of E can thus be calculated.

Six different indentation experiments were designed. Each experiment contained twelve segments, including three loading segments with successively increasing normal loads. A typical time dependent profile of load is showed in Fig. 2.9. A 10-second-hold segment was added to follow each load segment to allow the deformation to be stabilized. The reason for the addition of a longer hold segment at the end of an experiment is to monitor and correct for the thermal drift. The values of the maximum loads set in the six experiments are listed in Table 2.1. Each experiment was repeated ten times at ten different positions on a film surface to get an average result. A complete test on a specimen contains 60 indents arranged in a 10 x 6 array. Two adjacent indents were separated by a distance of 50 μm. Data points obtained with the same experimental setting show some scattering, because of the vibration of the system, and the roughness and uniformity of the sample surface. The degree of scattering of the data points gives estimates of the error bars.

A fused quartz standard with known hardness and modulus was used as a reference to monitor the performance of the system. The calibration of tip area function and load frame stiffness were carried out very carefully according to the procedures proposed by Oliver *et al*. [Oliver, 1992].

Table 2.1 The setting of maximum loads assigned in the six nanoindentation experiments.

Experiment	Indentation	Maximum load (mN)		
1	1 – 10	0.15	0.2	2.2
2	11 – 20	1	2	3.4
3	21 – 30	3	7.5	15
4	31 – 40	30	60	90
5	41 – 50	100	200	300
6	51 – 60	95	250	400

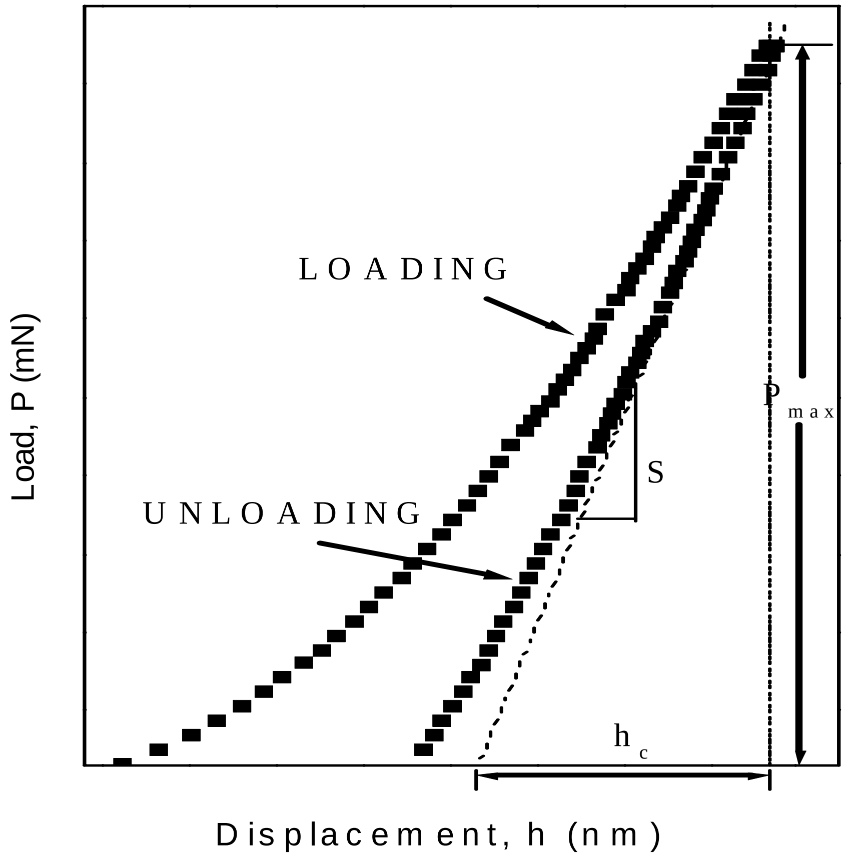

Fig. 2.8 Typical load-unload curves obtained in a nanoindentation test

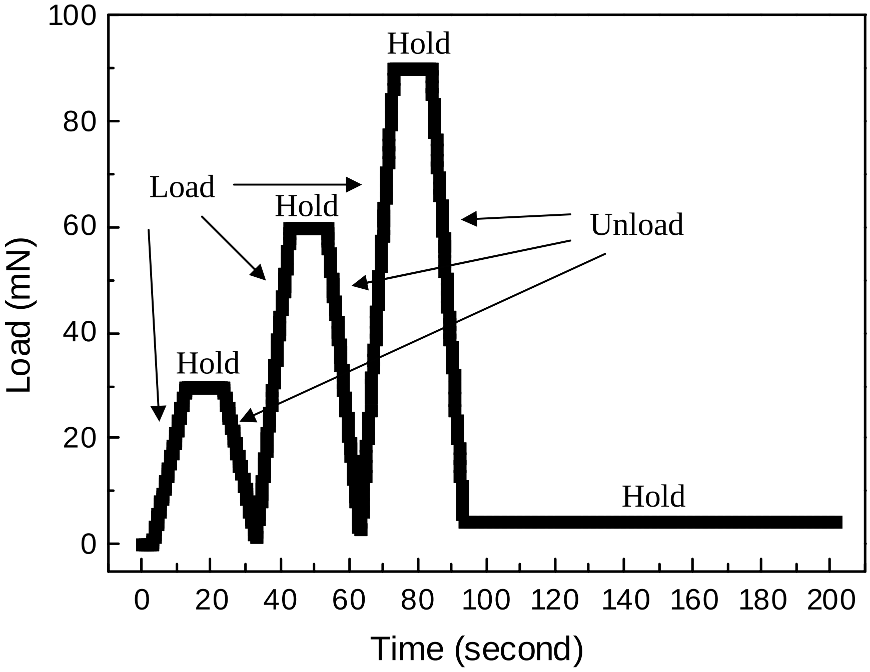

Fig. 2.9 A typical time dependent profile of load; Peak load = 30, 60, 90 mN

2.3.2 Stress analyses

The residual stress of a film is determined from the measurement of the radius of curvature of the film-on-substrate configuration. In this study, the radius of curvature of a specimen was measured by a surface profiler (KLA-Tenscor P-10). The stylus of the surface profiler was driven to scan across the film surface by a distance of 0.8 mm. 8000 data points of the vertical displacement of the stylus were recorded during the scan. The radius of curvature (R) of the sample could be found by fitting the surface profile with the equation of a circle:

$$x^2 + y^2 = R^2 \qquad (2.8)$$

The residual stress of the film (σ_f) is calculated from the Stony equation [Nix, 1989]:

$$\sigma_f = \frac{E_s}{(1-\nu_s)} * \frac{{d_s}^2}{6 \times R \times d_f} \qquad (2.9)$$

where E_s and ν_s are the Young’s modulus and Poisson’s ratio of the substrate, respectively. $d_s = 525$ μm is the thickness of the substrate, and d_f is the thickness of film. The value of $E_s/(1-\nu_s)$ is set at 180.5 GPa for (100) Si substrate. For each sample, four surface profiles were collected to produce an average result. In addition, from the direction of bending, one can identify whether the stress is compressive or tensile. By convention, a positive R represents a concave bending, indicating that a compressive stress exists in the film. On the contrary, a negative R represents a convex bending, indicating that a tensile stress exists in the film.

According to Reinke *et al.* [Reinke, 1996] and Fitz *et al.* [Fitz, 2002], the conventional Stoney's equation (Equation 2.9) can be modified to derive the internal stresses of the individual layers in a multilayered structure. For i-layered film system:

$$\sum_{n=1}^{i} \Theta_n d_n = \sigma_f d_f \tag{2.10}$$

where Θ_n is the stresses in the n^{th} layer and d_n is the thickness of corresponding layer. In the equation, d_f is the total thickness of a film and σ_f is the nominal overall stress of a film determined by equation 2.9.

Consider the analysis of the stresses in a two-layered film as an example. We started from looking at a film of the first layer only. The stress in this layer Θ_1 is first determined. Next, the overall stress σ_f of a film having both layers is measured. Then, the stress in the second layer Θ_2 is calculated from the equation: $\Theta_1 d_1 + \Theta_2 d_2 = \sigma_f d_f$.

Chapter 3

BN Films Deposited by Single-Step Processes

3.1 Motivation of Preparing BN Films with Single-Step Processes

Cubic boron nitride (cBN) is attractive because of its high hardness, and the chemical inertness against ferrous materials at high temperature [Riedel, 1994; Matsumoto, 2000; Matsumoto, 2001; Mirkarimi, 1997]. cBN-containing films are therefore supposed to have great potential to work as protective coatings on cutting tools for machining iron-containing substances. However, this potential application is greatly hindered by the poor adhesion of cBN films to most substrate materials. A general finding is that cBN-rich film thicker than 200 nm cannot be fabricated because the film would peel off readily after exposure to atmosphere [Matsumoto, 2000; Matsumoto, 2001; Keunecke, 2001; Kulisch, 2000; Li, 2002; Litvinov, 1999; Litvinov, 1997; Walter, 1999; Litvinov, 1998]. As a starting point of the whole project, we performed a preliminary test to investigate how thick of the cBN-rich film with good adhesion could be prepared by using our own ion beam system. We employed single-step processes in the sense that all the deposition parameters were not varied throughout a single run. This approach facilitates direct comparison of the result with the generally acknowledged level as published (i.e. ≈ 200 nm as mentioned above). In addition, the result will also be used as a reference to compare with the results obtained by using other deposition schemes to be described in the following chapters.

3.2 Sample Fabrication

In a single-step process, the substrate was first pre-cleaned by an assist Ar^+ beam of 600 eV and 54 mA. To start deposition, the boron target was sputtered with an Ar^+ beam of 1200 eV/70 mA from the sputtering gun, and concurrently the substrate was bombarded with an assist ion beam containing N_2^+ and Ar^+ ions at an energy of 450 eV and a current of 30 mA respectively. The substrate temperature was maintained at 680^{o}C. As a single-step process, all these settings were kept constant throughout the whole deposition process. A series of samples was produced by varying the deposition time in the range between 5 and 120 minutes to control the film thickness. The deposition conditions and the properties of the five samples in this series were summarized in Table 3.1.

Table 3.1 Deposition conditions and the properties of the BN films prepared with single-step processes.

Sample	I_{spu} / U_{spu} (mA / eV)	I_{assist} / U_{assist} (mA / eV)	t (min)	d (nm)	$\eta_{cBN\text{-}IR}$ (vol.%)	H (GPa)	E (GPa)	Coating rate (nm min^{-1})
cBN009	70/1200	30/450	5	19	22	10.7	153.3	3.80
cBN008	70/1200	30/450	10	27	29	10.9	162.9	2.70
cBN007	70/1200	30/450	30	183	43	23.7	233.7	6.10
cBN006	70/1200	30/450	60	362	56	Peel-off		6.03
cBN005	70/1200	30/450	90	507	64	Peel-off		5.63
cBN004	70/1200	30/450	120	658	65	Peel-off		5.48

I_{spu}: sputtering beam current

U_{spu}: sputtering beam energy

I_{assist}: assist beam current

U_{assist}: assist beam energy

t : deposition time

d : film thickness

E: Elastic modulus

H: Hardness

$\eta_{cBN\text{-}IR}$: volume fraction of cBN phase estimated by IR absorption

3.3 Thickness Dependence of the Film Properties

As shown in Table 3.1, the deposition time *t* was the only parameter varied in the deposition, which increased from 5 to 120 min. Correspondingly, the film thickness *d* increased steadily from 19 to 658 nm.

Fig. 3.1 shows the IR absorption spectra of the films with increasing film thickness. Results show that for thin samples, the spectra mainly contain two absorption bands at 780 cm^{-1} and 1390 cm^{-1} respectively, which are known to come from the out-of-plane B-N-B bending mode and in plane B-N stretching mode of the sp^2 BN structure. With increasing film thickness, an absorption band at 1080 cm^{-1} is observed, which is associated with the transverse optical mode of the sp^3 structure. This result immediately implies that thin sample (e.g. cBN009) is mainly constructed of sp^2 phase, and the volume fraction of the sp^3 phase increases with increasing film thickness. According to Eq. (2.4), the volume fraction of the sp^3-bonded phase increased from 22 to 65 % when the film thickness increases from 19 to 641 nm (Fig. 3.2). Since all the deposition parameters (other than the deposition time) were not changed, this result illustrated that the formation of the sp^3 phase required an incubation process. The ion-induced stresses in the deposits would be accumulated concurrently. A direct consequence is that the microstructure of the film is non-uniform along the direction of growth.

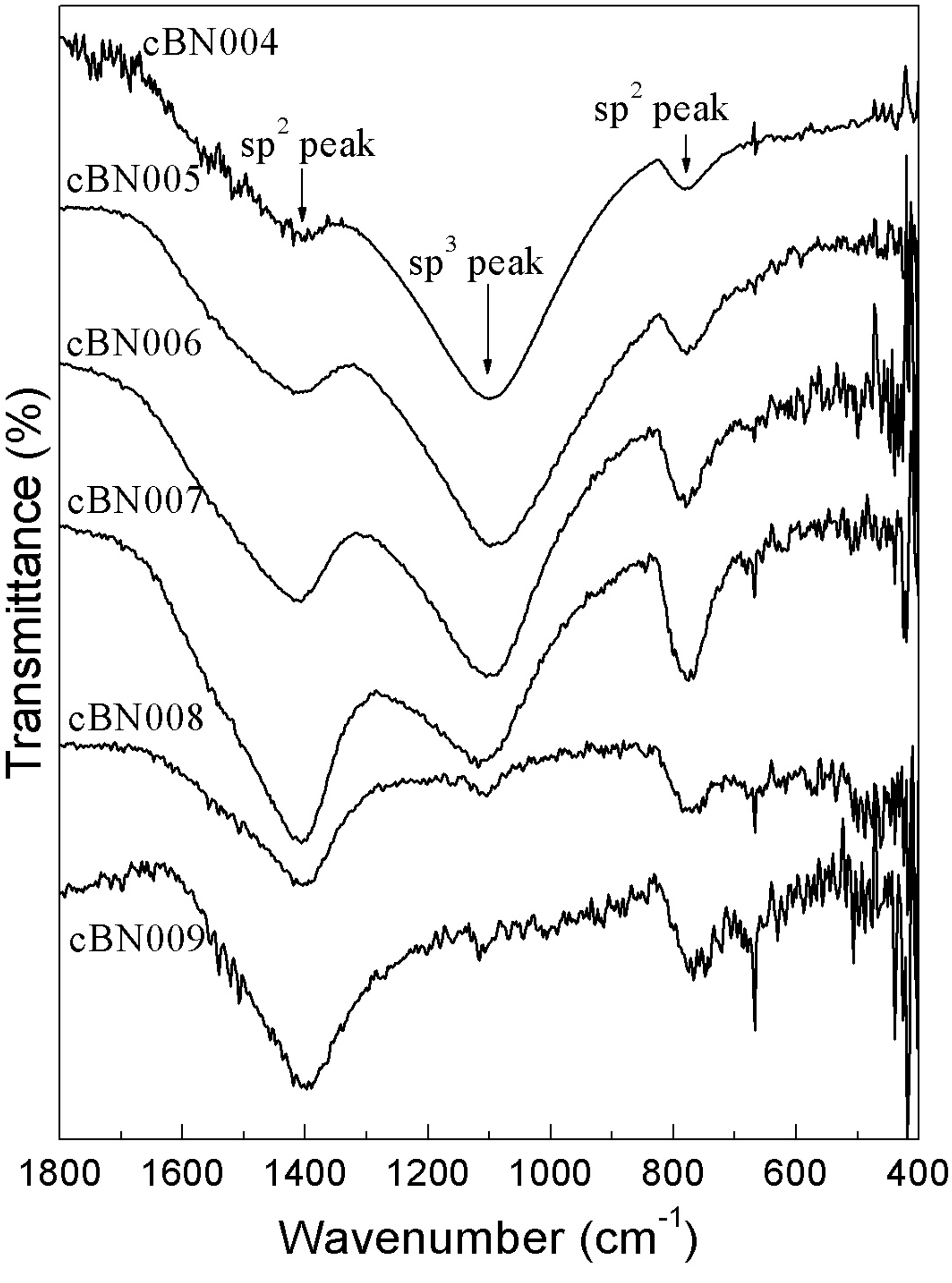

Fig. 3.1 FTIR absorption spectra of the samples of different thicknesses.

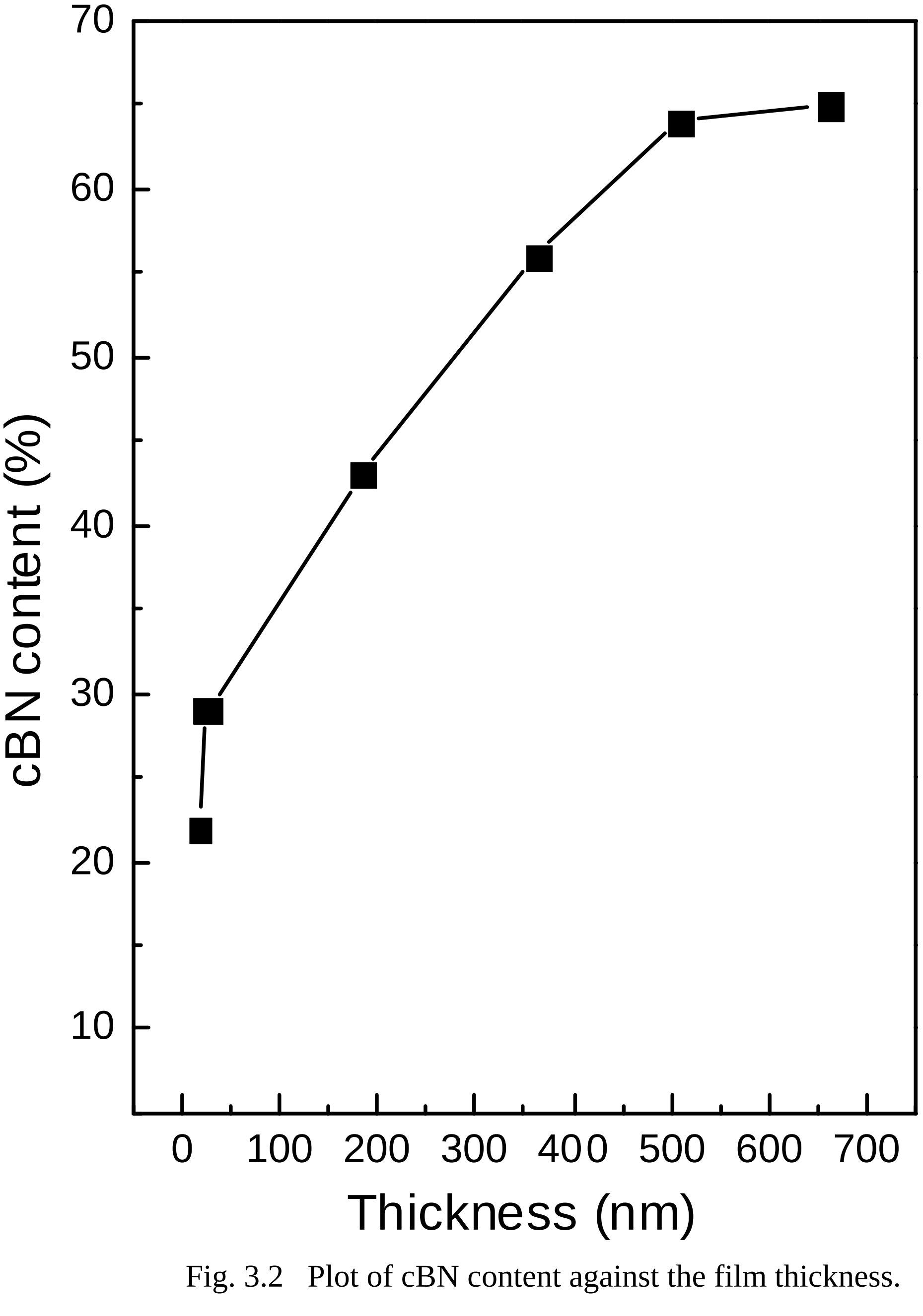

Fig. 3.2 Plot of cBN content against the film thickness.

Another consequence related to the increase in the sp^3 content with increasing film thickness is the rise in both hardness and elastic modulus of the films. In particular, the hardness of Sample cBN009 containing 22 vol.% cBN phase was just 10.7 GPa. However, for Sample cBN007 containing a higher cBN volume fraction of 43 % has a much high hardness of 23.7 GPa.

It is also interesting to see how the coating rate depends on the sp^3 content as shown in Fig. 3.4. For the films with sp^3 contents ≤ 30 vol.%, the coating rate is small because the sp^2 phase dominates in the film structure, which is relatively soft and more readily to be sputtered under the assist beam bombardment. On the other hand, for the films having sp^3 content > 30 vol.%, the coating rate rises abruptly and is finally stabilized at a level of 5.5 - 6 nm min^{-1}. This is because the sp^3-bonded structure is much harder, and the films of higher sp^3 content exhibit a lower resputtering rate compared to that of the films of sp^2 structure.

The most important conclusion drawn from this part of study is that the films thicker than 183 nm (cBN006, cBN005 and cBN004) would peel off very quickly after deposition and exposure to the atmosphere. As such, the maximum thickness of cBN-rich film with good adhesion obtainable by using our own ion beam system with a single-step process is 183 nm, which is basically consistent with the generally acknowledged level ≈ 200 nm as reported in literature [Klett, 2001; Kester, 1993; Park, 1997; Ichiki, 1996]. We shall use this value as a reference in the following discussions.

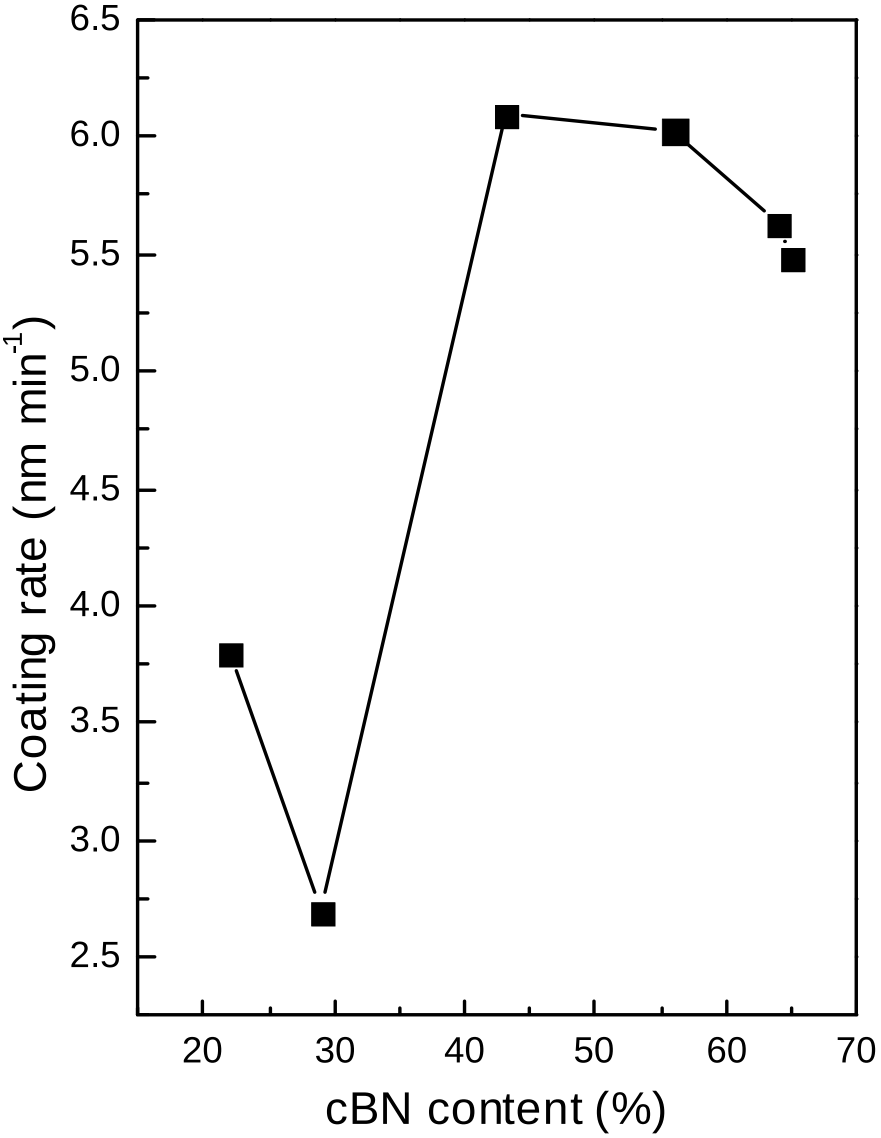

Fig. 3.4 Coating rate versus the cBN content in the BN films.

Chapter 4

Multilayered BN Films with sp^2 BN Buffer Layers

4.1 Motivation of Adding a sp^2 BN Buffer Layer

Results of the previous study described in Chapter 3 show that a cBN-rich film prepared by a single-step ion assist deposition process would peel off from the substrate when the thickness exceeds around 180 nm. Therefore, if cBN-rich film thicker than this value is required, some new deposition schemes have to be employed in order to get a better adhesion between the film and the substrate. One intuitive idea is to add a thick sp^2 BN buffer layer first, which has a smaller shear strength (especially along the basal plane direction) compared to that of the cBN structure, and so is more deformable under stresses. Therefore, when a cBN-rich layer is added on top, the sp^2 buffer layer would deform to some extent so as to release some stresses created in the cBN-rich layer. As a BN material, the buffer layer is considered to be able to adapt better to the cBN-rich layer.

This chapter reports the fabrication of film samples with the addition of thick sp^2 BN buffer layers. Results of structural characterization and mechanical property measurements are presented and discussed. The possible formation mechanisms of the microstructure as observed are interpreted based on some theoretical models.

4.2 Fabrication of Multilayered Films with sp^2 BN Buffer Layers

In Section 4.2 to 4.4, we present the results of a typical sample cBN023, which features are found to be common to all of the samples prepared with the scheme described in this chapter. Sample cBN023 is selected because its cBN-rich layer is the thickest among the samples in the series. The procedures for preparing Sample cBN023 are described as follows, where the values of the deposition parameters are summarized in Table 4.1. Other samples in this series share the same procedures and parameter values, except the deposition time (and hence the thicknesses) of the layers are different.

Step 1 The (100) silicon (Si) substrate was first heated up to 680^{o}C, and then was pre-cleaned by an argon ion (Ar$^+$) beam of energy U_{assist} = 600 eV and current I_{assist} = 54 mA.

Step 2 A three-step process was then employed to deposit a gradient BN buffer layer, which was finally verified to be sp^2-bonded. In this step, a boron target (99.9% purity) was sputtering with an Ar$^+$ beam of energy U_{spu} = 1200 eV and current I_{spu} = 70 mA. The substrate was bombarded simultaneously by an assist beam containing argon and nitrogen ions (Ar$^+$ and N_2^+). In particular, the assist beam was generated by admitting Ar and N_2 gases into the assist ion gun with flow rates in a ratio of 1.2 : 1. The U_{assist} value was increased successively from 200 to 280, and then to 360 eV (Table 4.1), each lasting for 20 min. A three-sub-layered buffer layer was expected to be produced.

Step 3 U_{assist} was then further increased to 450 eV to deposit a top layer, which was verified finally to be cBN-rich. I_{assist} was fixed at 30 mA. This step lasted for 180 min.

Table 4.1 Deposition parameters used to fabricate Sample cBN023. Other samples in the series shared the same data, except that the deposition time t is different.

Step	Purpose	t (min)	I_{spu} / U_{spu} (mA / eV)	I_{assist} / U_{assist} (mA / eV)	T_{s} ($^{\text{o}}$C)
1	Cleaning	10	NIL	54 / 600	680
2	Gradient BN buffer layer	20	70 / 1200	20 / 200	
		20	70 / 1200	20 / 280	
		20	70 / 1200	20 / 360	
3	cBN layer	180	70 / 1200	30 / 450	

U_{spu} : sputtering beam energy
I_{spu} : sputtering beam current
U_{assist} : assist beam energy
I_{assist} : assist beam current
t : deposition time
T_{s} : substrate temperature

4.3 Preliminary Inspection of the Layered Structure

A low magnification cross-sectional transmission electron microscopy (TEM) image of the sample is shown in Fig. 4.1. It verifies that the film has a layered structure in accordance with the design of the deposition process. The figure illustrates a clear boundary between a 492-nm buffer layer and a 643-nm top layer.

Fig. 4.2 shows the infrared absorption (FTIR) spectra of the buffer layer and the top layer respectively. The buffer layer sample for this measurement was prepared separately with the same conditions used for preparing the buffer layer of Sample cBN023. The spectrum of the top layer was obtained by removing the contributions from the buffer layer and substrate. For the buffer layer, two absorption bands at 1390 and 780 cm^{-1} are found, which are attributed to the sp^2-bonded structure. For the top layer, a strong absorption band at 1080 cm^{-1}, associated with the cBN structure is observed. It is thus verified that the two layers are sp^2- and sp^3-bonded respectively. According to equation 2.4, the volume fraction of cBN phase in the top layer is as high as 87%.

In addition, the hardness and elastic modulus of the top layer are measured to be 57 GPa and 612 GPa, which are very high and consistent with the high volume fraction of the cBN phase as measured in IR absorption experiment.

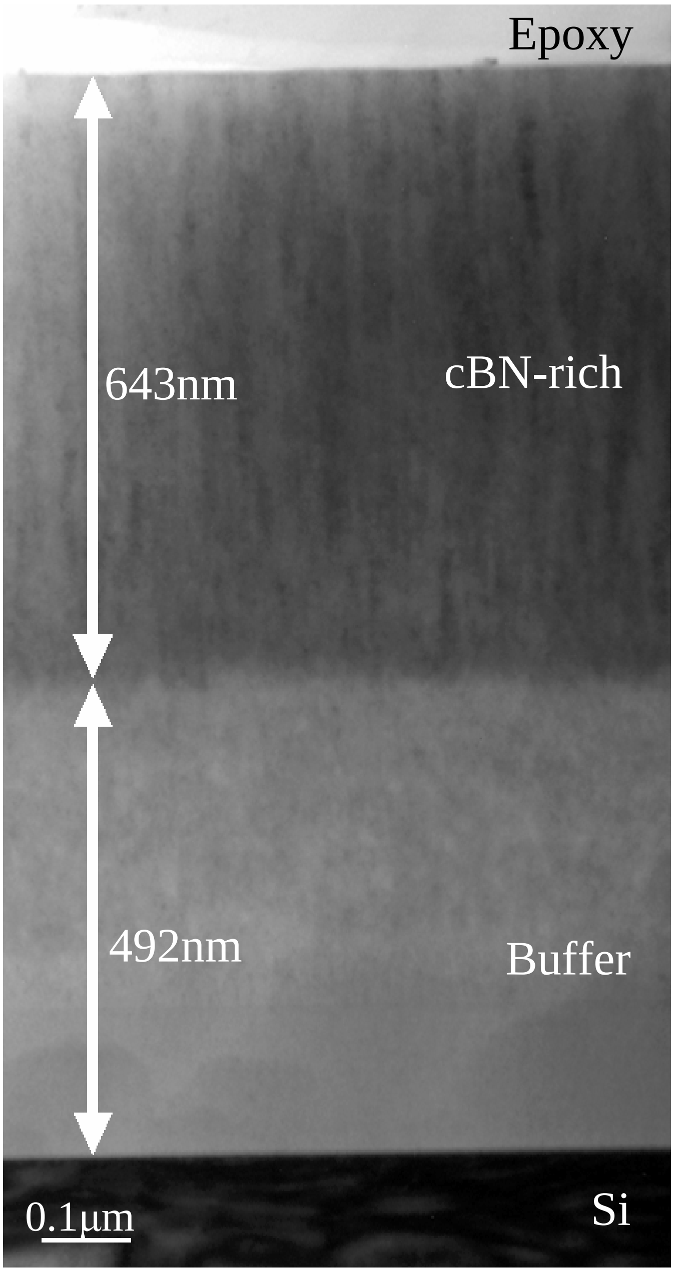

Fig. 4.1 TEM micrograph showing the layered structure of Sample BN023 (typical to all samples prepared with this deposition scheme).

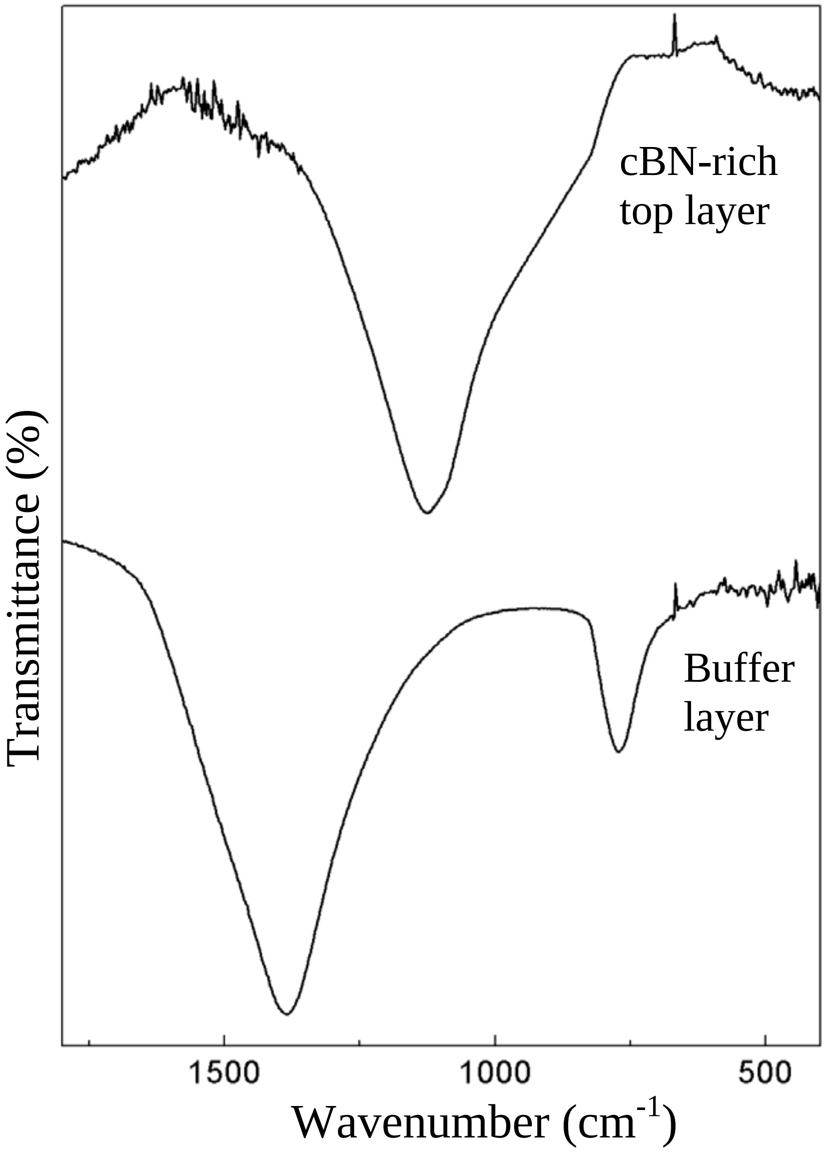

Fig. 4.2 FTIR absorption spectra of the top layer and buffer layer of cBN023.

4.4 Detailed Analysis of Individual Layers

According to the data of higher magnification TEM images captured from different locations across the cross section of Sample BN023, it is found that the microstructure of the film is highly inhomogeneous along the growth direction, and is much complicated than the low-magnification image as displayed in Fig. 4.1. This section is written to describe in detail the microstructures of the individual layers.

4.4.1 Substrate-buffer interface

Fig. 4.3 (a) is actually the same as Fig. 4.1, but some layer markers are made to illustrate the expected locations of the boundaries between and the thicknesses of different layers according to the procedures of deposition. We start from looking at the interface between the substrate and the film material. A high resolution TEM (HRTEM) image of this region is taken and shown in Fig. 4.3 (b), which indicates a highly disordered interfacial layer with a thickness of 3.8 nm is formed on the substrate surface right at the beginning of the deposition process. Similar interfacial layers have been observed by other groups, and often interpreted as the “amorphous” BN (aBN) layer [Djouadi, 2001; Guiot, 2001; Kester, 1994; Li, 2002; Takamura, 1999; Yang, 2002]. Hofsäss *et al*. gave an explanation by suggesting that it was actually an ion mixing layer containing the atoms from the substrate, deposits and the bombarding ions [Hofsäss, 1995]. This idea has not been directly verified experimentally [Mirkarimi, 1997], however, the following theoretical estimation seems to imply this conjecture is reasonable. According to the simulations with

TRIM, the projected range of the incident species (Ar^+ and N_2^+ ions of 200 eV for depositing the 1st sub-buffer layer) in the target materials (the BN deposits and Si substrate) is about 1.2 - 1.7 nm (Fig. 4.4). Further, the end of range should be larger, estimated to be 2-3 times longer. Hence, the region affected by the intruding ion would have a size around 2.4 – 5.1 nm. The mean value is very close to the thickness of the interfacial layer. The ion-mixing theory is thus supported. In our case, mixing layer could contain boron atoms, nitrogen atoms, silicon atoms and probably a small amount of Ar atoms.

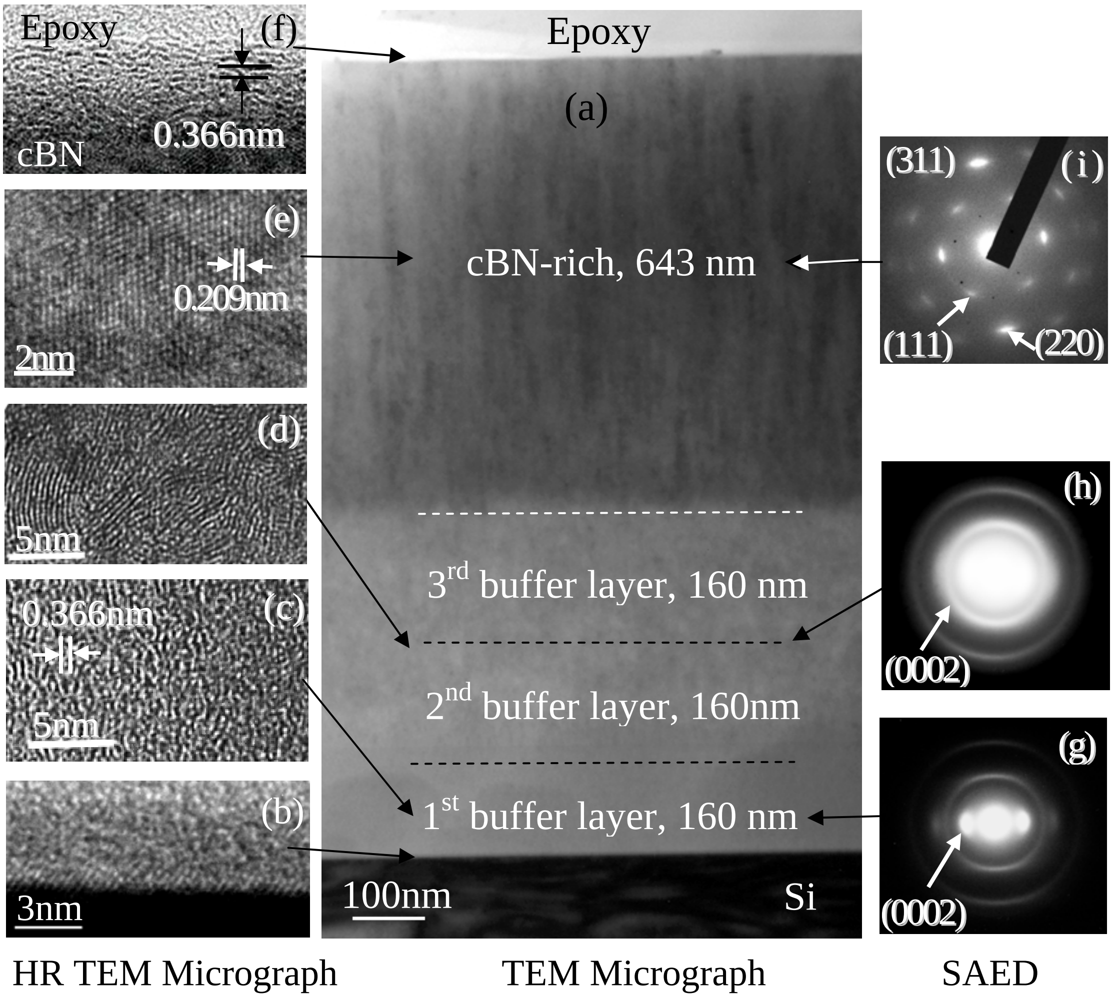

Fig. 4.3 (a) Low magnification TEM image of the cross section of Sample BN023.
(b) – (f) High magnification TEM images of selected areas at different points.
(g) – (i) SAED patterns taken at different points.

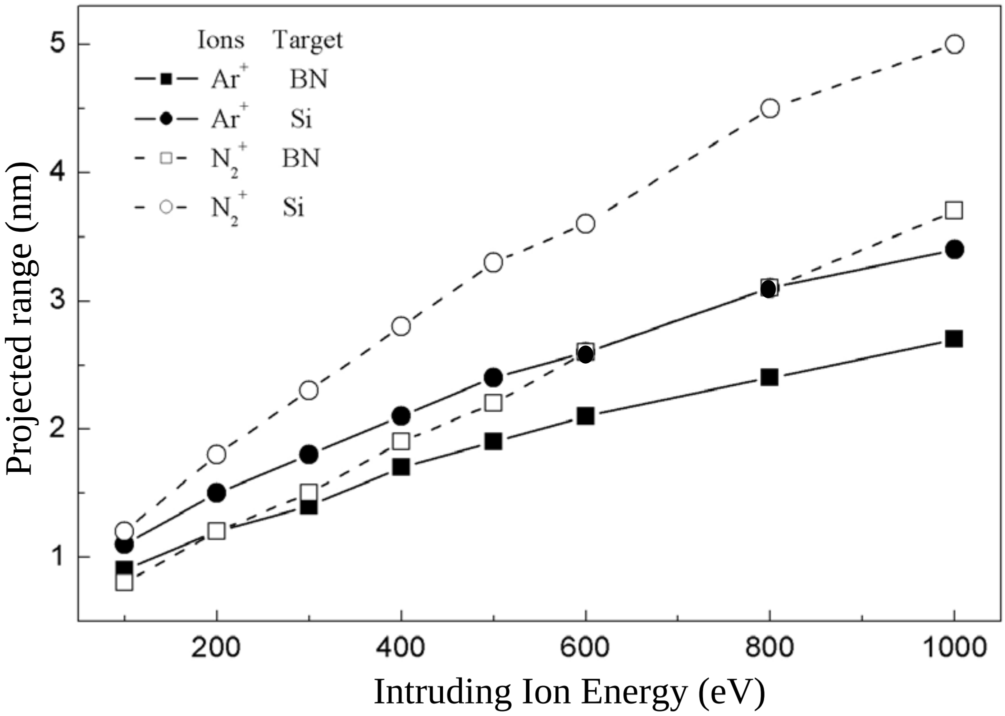

Fig. 4.4 Projected range of intruding ions with different energies simulated by TRIM

4.4.2 Buffer layer

In Fig. 4.3 (a), some layer markers have already been made to roughly differentiate the sub-layers in the buffer layer according to the successive increase in U_{assist} from 200 to 360 eV as assigned in the deposition scheme (Table 4.1). A dark field TEM image of the buffer layer (Fig. 4.5) was produced to map the sp^2-bonded grains with their basal planes preferentially aligned along the substrate normal direction. The grains of this preferred orientation are decorated with a bright contrast in the micrograph. The image further illustrates the boundary between the 1st sub-buffer layer deposited at U_{assist} = 200 eV and the 2nd sub-buffer layer deposited at U_{assist} = 280. No clear boundary between the 2nd and 3rd is observed, but a layer marker is still made by assuming that the deposition rates of the two layers are approximately equal.

Consider the 1st sub-buffer layer first. Fig. 4.3 (c) shows the HRTEM image of this region. One observes some fringes with an average separation of 0.366 nm. This distance is identical to the lattice spacing of the (0002) planes in the hexagonal BN (hBN) structure, verifying that this regions are mainly sp^2-bonded. The HRTEM image shows that the sp^2 basal planes are relatively short and roughly aligned along the substrate normal direction. This feature is consistent with the selected area electron diffraction (SAED) pattern in which two diffused diffraction spots associated with the sp^2 planes are located in a line in parallel with the substrate surface (Fig. 4.3 (g)).

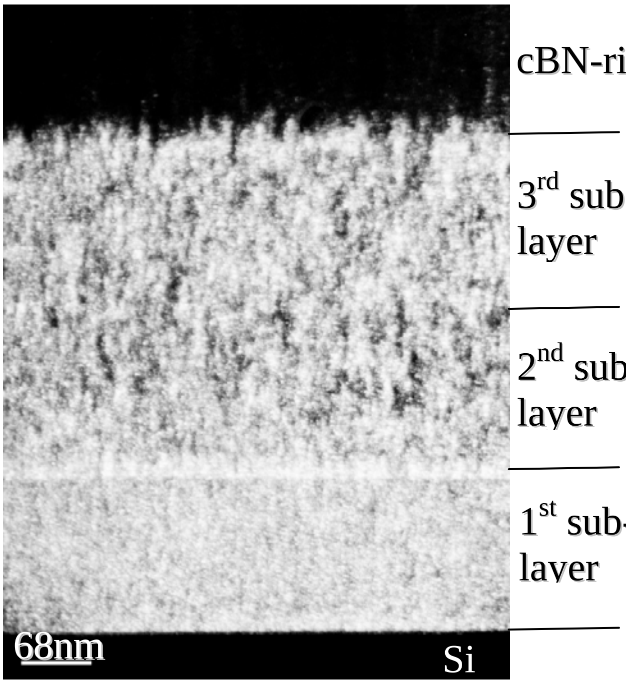

Fig. 4.5 Dark field image of the buffer layer. The bright areas represent the sp^2-bonded regions with the (0002) planes aligned along the substrate normal.

We further note that the 1st sub-buffer layer exhibits some features of the so called "turbostractic BN" (tBN) generally quoted in the literature. The tBN structure is defined as a stack of sp^2 basal planes with random rotation about their c-axis. However, the HRTEM image of the 1st sub-buffer layer shows that the basal planes are short and rather defective, and so the "tBN" concept may not be completely suitable to be used to describe the structure of this sub-layer.

We then focus on the interface between the 1st and 2nd sub-buffer layers. The dark field image (Fig. 4.5) illustrates that there is a 20-nm thick layer at this interface showing rather bright contrast. This indicates that the graphitic basal planes across the interface are arranged more orderly compared to those in other regions. We notice that this interface is at the depth where U_{assist} is switched from 200 to 280 eV during deposition. A model is proposed to explain this finding. When a bombarding ion with kinetic U_{assist} intrudes into the deposits, it would displace the atoms along its trajectory to create some biaxial stresses in the film. The biaxial stresses could extend to affect a region with a dimension larger than the travelling range of the ion. Under the influence of the biaxial stresses, the basal planes in this region could have different forms of deformations, such as kinking, sliding or rotation, and so are driven to have the preferential alignment as observed [McCarty, 1997; Hofsäss, 1995]. We assume that an incident ion affects a region with a spherical shape having a radius R. From the TRIM analysis, it is known that an incident with a typical energy around 280 eV would stop at a depth 1.5 nm (Fig. 4.4) below the film surface. Then the value of R would be roughly equal to the thickness of the "orderly" aligned region observed. The strain ε is approximately equal to r_o/R, where r_o is roughly equal to the size of an atom (e.g. $r_o = 0.098$ nm for a B atom). The elastic energy density in the deformed region is $E\varepsilon^2/2$. The elastic energy stored in the film associated with the intrusion of a bombarding ion is therefore $(E\varepsilon^2/2)(4\pi R^3/3)$, which is approximately equal to the energy carried by the ion U_{assist}. The elastic modulus for the sp^2-bonded phase is known to be $E = 110$ GPa, according to the result of nanoindentation tests. By setting $U_{\text{assist}} = 280$ eV, R is estimated to be 20 nm, roughly equal to the thickness of the observed "orderly" aligned region between the 1st and 2nd sub-buffer layers as shown in Fig. 4.5.

Now let us discuss the 2nd and 3rd sub-buffer layers. The HRTEM image Fig. 4.3 (d) illustrates that the layers are constructed of sp^2 basal planes with an average spacing identical to that of hBN. Different from the 1st sub-buffer layer, the basal planes in the 2nd and 3rd sub-buffer layers are not aligned quite orderly, but exhibiting some degree of curling. The SAED pattern as shown in Fig. 4.3 (h) further illustrates the randomness induced by the curling of the basal planes, in which some diffused halos in the shape of full circles are seen. In addition, the dark field TEM image (Fig. 4.5) shows less bright contrast compared to the 1st sub-buffer layer, reflecting that the basal planes in the 2nd and 3rd sub-buffer layers are not aligned as orderly as those in the 1st sub-buffer layer. Indeed, curling of sp^2 planes in BN films has been reported by many other groups [Cardinal, 1997; Collazo-Davila, 1997; Collazo-Davila, 1999; Banhart, 1994; Li, 2002]. Different mechanisms have been proposed to explain the curling of basal planes. It is proposed that ion-induced biaxial stresses could be accumulated to high level to cause kinking of basal planes [McCarty, 1997]. On the other hand, Collazo-Davila *et al.* suggested that energetic particle bombardment could induce knock-on events and atomic displacements, which led to the formation of BN nanoarches [Collazo-Davila, 1997; Collazo-Davila, 1999]. This is possible since the value of U_{assist} is in the range of 200 – 360 eV, which is much higher than the energy required displacing an atom in a solid (≈ few eV's). Though the real mechanism responsible to the curling of basal planes is still not clear, the most important implication of this finding is that a thicker sp^2 layer would have larger deformability. As such, during the growth of the top cBN-rich layer, the stresses in the film are progressively evolved, and with the presence of a thick sp^2-bonded buffer layer, the buffer layer can be deformed to result in relaxation of some stresses in the layered structure. This explains why a 643-nm thick cBN-rich layer with good adhesion can be made in Sample BN023 with the introduction of a thick sp^2 buffer layer. Such a thickness is over 3 times of the maximum attainable thickness of the cBN-containing films prepared by single-step process as described in the previous chapter.

The deliberately introduced 3rd sub-buffer layer appears to be the most interesting. From the HRTEM image taken from the middle of the sub-layer (Fig. 4.6 (a)), both the hexagonal (hBN) and rhombohedral (rBN) phases are seen. For example, the rhombohedral BN (rBN) structure is seen in the "t" region, as identified by the presence of two sets of fringes having d-spacings measured to be 0.354 and 0.206 nm respectively, and mutually intercepting with 65°. They are identified to be the (003) and ($10\bar{2}$) planes of the rBN structure [Yamada-Takamura, 1999]. Most interestingly, some regions with not clearly defined structure were observed, as labelled by "p" in Fig. 4.6 (a). These "p" regions are commonly observed at the top regions of the buffer layers of all the samples prepared with similar conditions, and are not occasionally found by chance. The HRTEM image (Fig. 4.6 (a)) suggests that the structure of the "p" region is so disordered that not fringes can be identified. The image is so blurred that no accurate d-spacing between atomic planes can be derived. However, the electron energy loss spectra (EELS(TEM)) of the t and p regions were collected and analyzed by using the Gatan imaging filtering (GIF) installed in the TEM system (JEOL 3000 FEG-TEM), from which very useful information is obtained. From the EELS(TEM) spectra, one observes the onsets of the B K and N K edges at 188 eV and 401 eV, respectively. For a region t, the strong 1s-π^* peak at ~ 191 eV indicates the existence of sp^2-bonded BN. The intensity of the 1s-π^* peak decreases to a large extend in the EELS(TEM) spectrum taken from region p, although the spectroscopy conditions are not changed when taking the spectra. The results indicate that the p regions should possess sp^3-bonded BN short-range order. Since the sizes of the p regions are in the order of around a few nanometres, it is therefore claimed that the p regions are sp^3-bonded BN nanoclusters. This term will be used throughout the following text. To our knowledge, this structure has not been reported in the literature to date. Since it emerges at the regions where structure starts to transition from the sp^2 phase to sp^3 phase, we may imagine that it is an intermediate stage involved in a sp^2-to-sp^3 transition, and so could also be named as the “precursors” of cBN nucleation or the cBN nucleation sites. One important issue is that the IR absorption spectrum of the buffer layer (Fig. 4.2) does not show any signal from the sp^3 phase. This may imply that the IR absorption technique is not sensitive enough for the detection of very small sp^3 inclusions. Further explanation on the efficiency of using IR absorption to detect nano-sized sp^3 clusters will be given in Chapter 6.

Finally, the p regions disappear when approaching the 3rd sub-buffer layer / cBN-rich layer interface. Instead, the interface itself is rough. Well-defined small cBN crystallites are observed and coexist with the sp^2-bonded BN. Fig. 4.7 shows the intermixing of the different BN structures close to the buffer / cBN interface. The d-spacing measured from the high-resolution image are 0.209 nm and 0.366 nm, agreeing with the spacing of the cBN (111) planes and hBN (0002) planes, respectively.

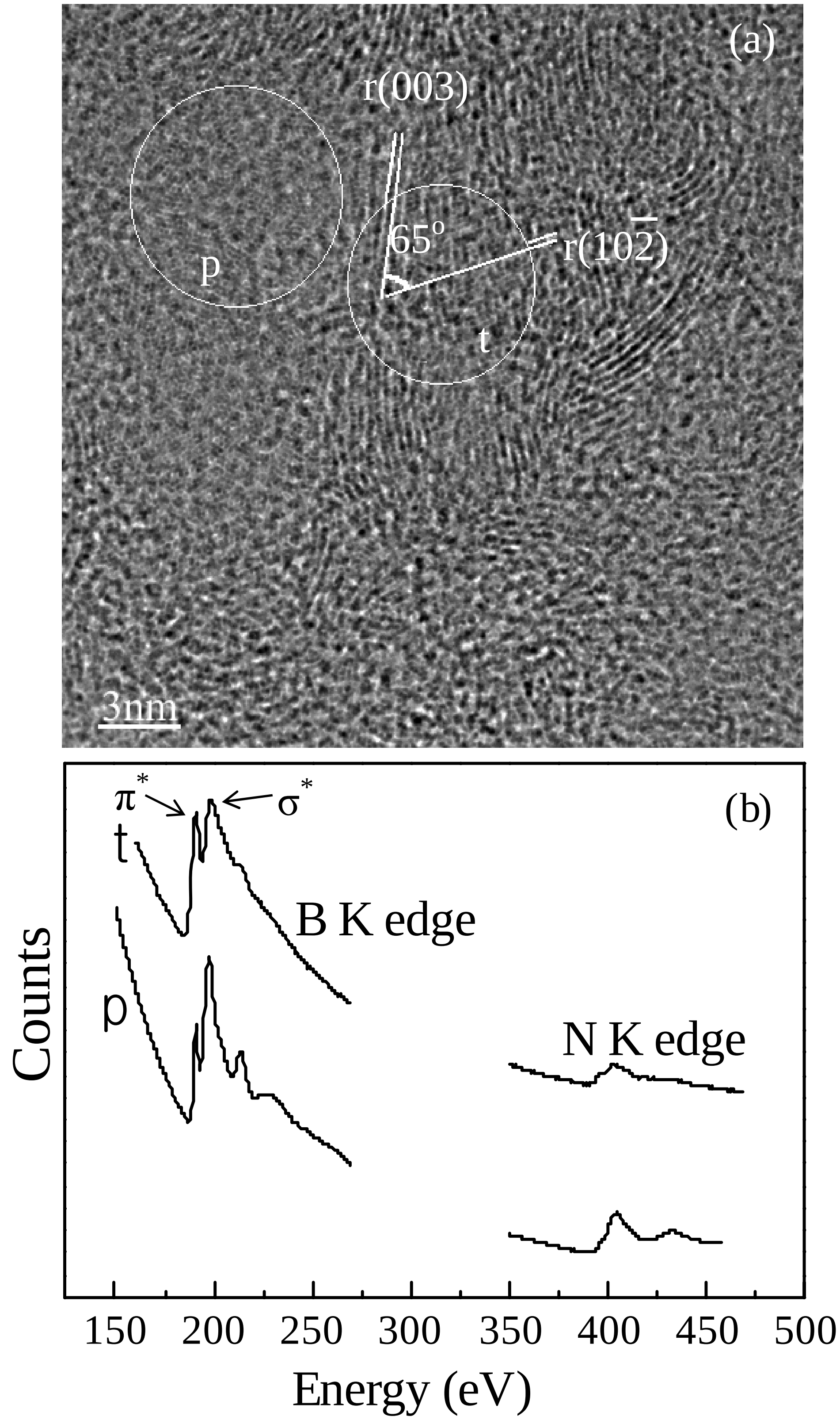

Fig. 4.6 (a) High magnification image showing the fringes of rBN, and (b) TEM-EELS spectra taken at the t and p regions.

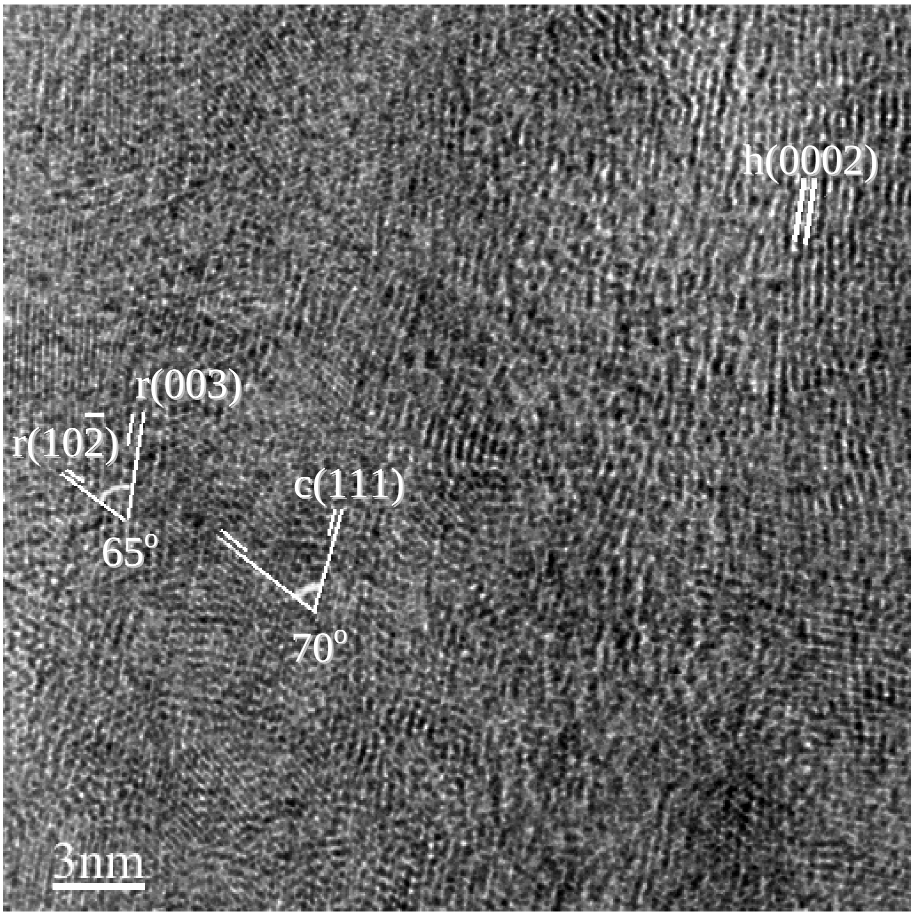

Fig. 4.7 High magnification image taken at a region close to the 3rd sub-buffer layer / cBN-rich layer interface.

We mentioned previously the concept of “tBN”, which is widely quoted in literature as if it is a well-defined single phase of boron nitride. However, according to the TEM images and electron diffraction patterns of three sub-buffer BN layers, we learned that a sp^2-bonded structure could show a broad spectrum of variation. We therefore suggested that “tBN” is actually a fuzzy concept which is too simple to describe a real sp^2 structure in a film. Additional complications of a real sp^2 structure in a film material observed in the present study include:

(i) random alignment and curling of sp^2 basal planes;

(ii) inclusion of sp^3 BN nanoclusters which are indiscernible by IR absorption;

(iii) coexistence of cBN, hBN, rBN and aBN phases.

We therefore suggest not to apply the concept “tBN” to describe an apparently random sp^2 structure, instead, it is more reasonable to treat an sp^2 structure in a film material as if it is a composite possible possessing the above structural features.

4.4.3 cBN-rich layer

Now, we look at the interface between the 3rd sub-buffer layer and the top cBN-rich layer. In this region, the material transits from the sp^2 phase to the sp^3 phase. HRTEM image shows a 2 : 3 matching between the basal planes and the cBN (111) planes. Entering the top-layer region, the IR absorption data (Fig. 4.2) shows that the top layer contains 87 vol.% cBN phase. Correspondingly, the hardness reaches a spectacularly high level of 57.1 GPa. The HRTEM image (Fig. 4.3 (e)) shows that the structure is dominated by cBN grains with the (111) planes aligned along the growth direction. The sharp boundary between the 3rd sp^2 sub-buffer layer and the top cBN-rich layer implies that there an abrupt and massive nucleation of cBN grains occurs. We adopt the stress model [Reinke, 1995] to explain this process, where the model states that the sp^2-to-sp^3 transition would occur once the compressive stresses in a sp^2-bonded structure are accumulated to reach a threshold level high enough for the transition [Li, 2002]. We further point out that some sp^2 structure exists between the cBN grain boundaries. This is directly shown by the HRTEM image shown in Fig. 4.8.

Fig. 4.9 shows the dark-field image of top layer created by analyzing the electron diffraction spot from the (111) cBN planes (Fig. 4.3 (i)). One immediately sees that the cBN grains are aligned with their (111) planes along the substrate normal. A magnified image of a selected region shows that there are a lot of stacking faults in the top cBN-rich layer. The average lateral size of the stacks is used to represent the grain size of the cBN grains. It is roughly estimated to be 50 nm.

However, the size of the two grains along the growth direction is much smaller, and is close to the travelling range of the incident particles.

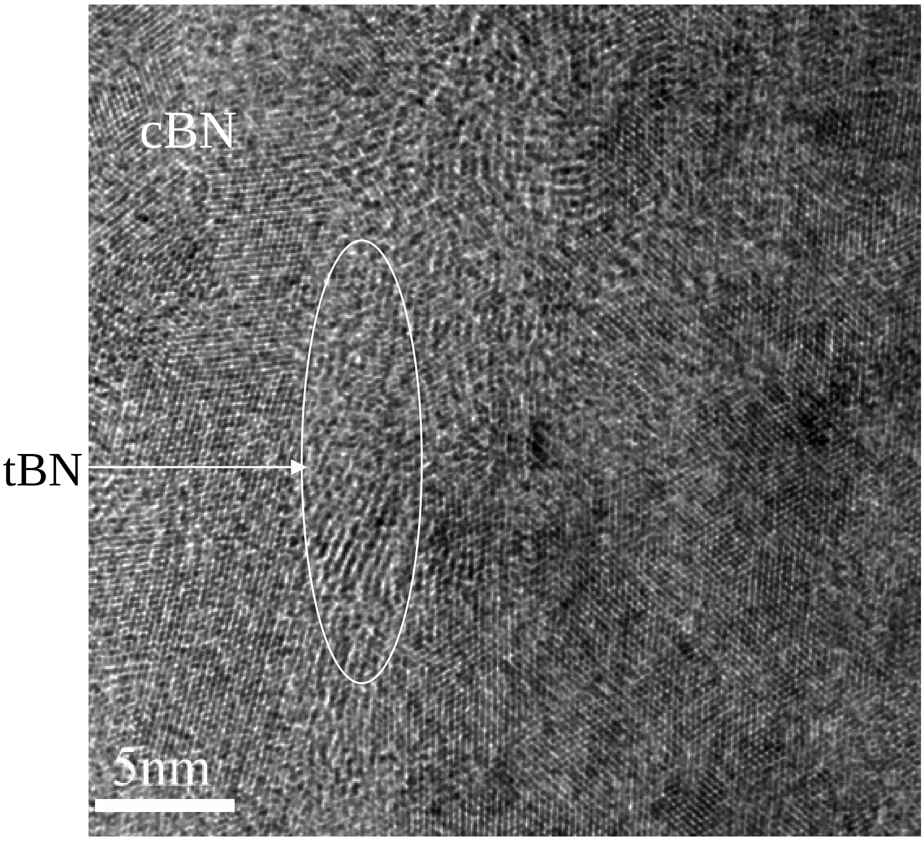

Fig. 4.8 HRTEM image showing the presence of sp^2-bonded phase at the boundaries between the cBN grains.

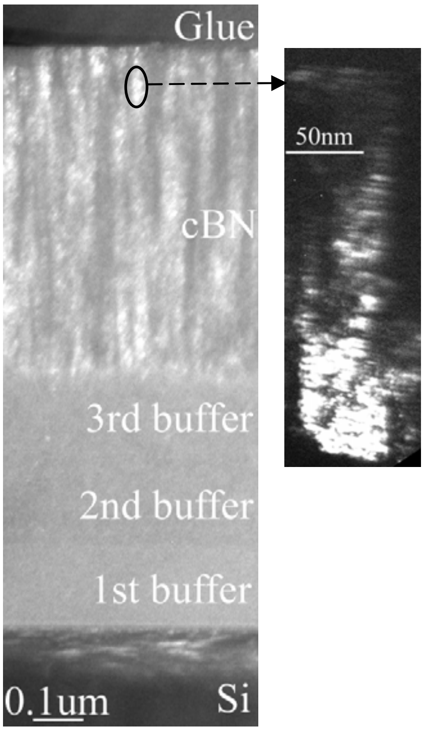

Fig. 4.9 Dark-field images obtained from the cBN (111) diffraction ring.

4.4.4 Thin sp^2-bonded layer at the surface of the cBN-rich layer

There is a very special layer appearing at the top surface of the cBN-rich layer. According to the high-resolution TEM image taken from this region (Fig. 4.3 (f) and Fig. 4.10), it is found that there is a ~ 3 nm thin layer at the top of the cBN-rich layer. Fringes are observed in this layer, where the spacing between them is 0.366 nm, identical to that of the sp^2 structure. The EELS(TEM) spectrum (Fig. 4.10 (b)) taken with an electron beam with a probe size of ~ 2 nm shows two edges at 191 eV and 401 eV, corresponding to the characteristic energy K edge loss of boron and nitrogen, respectively. The π^* peak at 191 eV is signature of the sp^2 structure. All these data verify that this special top layer covering the cBN-rich layer is sp^2-bonded. Similar top layer was also discovered by other authors [McKenzie, 1993].

It is interesting to note that orientation of (0002) planes of this surface sp^2 layer is either random or roughly in parallel with the film surface, and so is different from that of the sp^2-bonded regions in the 1st buffer layer and the cBN-rich layer. We note that a surface sp^2 layer was also observed by Hofsäss *et al.*, but they reported that the (0002) planes in the layer were aligned perpendicular to the film surface [Hofsäss, 2002]. Intuitively, in our case, the arrangement of the basal planes contains less dangling bonds, and thus the surface energy would be lowest. More detailed studies on the sp^2 basal planes on the surface of cBN-rich films deposited at different conditions would provide clues revealing the growth mechanisms of cBN grains.

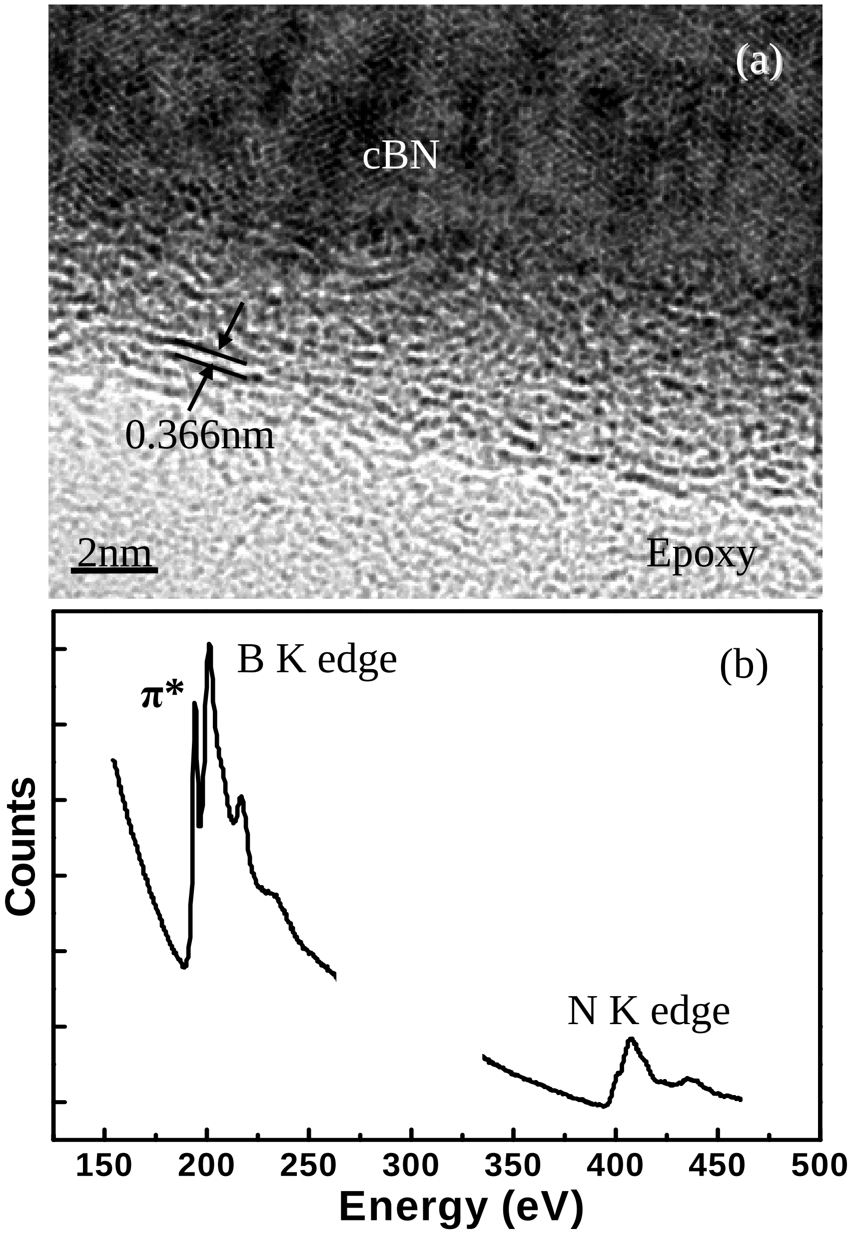

Fig. 4.10 (a) HRTEM image and (b) TEM-EELS spectrum of a non-cBN layer covering the top of the cBN-rich layer of Sample cBN023.

4.5 Discussions on the Growth Mechanisms of the cBN-Rich Layer

The growth process of the cBN-rich layer is considered to be rather complicated, in which energetic ion bombardment plays essential role in affecting the microstructure of the films through the following mechanisms. The first is the momentum transfer to the constitutional atoms through collisions, causing the atoms to displace and result in damages of the original cBN structure in the deposits (ion irradiation damage). The second is the arrangement of the atoms to their lattice positions to retain the cBN lattice (ion annealing). These two effects are opposite in the sense that they generate and remove defects, resulting in an increase and relaxation of the internal stresses. In addition, the assist beam may also damage the sp^3 structure and convert it into the sp^2 structure. Moreover, resputtering of the deposited atoms could happen. All these effects may coexist to give an overall result in determining the final features of the microstructure. Some of them may dominate at a particular deposition condition, but nowadays, there is not a prevailing theory to explain the growth process. In this section, we present the U_{assist} dependence of the properties of the cBN-rich layer, and the features of a thin sp^2 surface layer on the top of the cBN-rich layer, and discuss the related implications of the growth mechanisms of the cBN-rich layer according to the data observed.

4.5.1 U_{assist} dependence of the growth of the cBN-rich layer

In order to investigate the influence of the setting of U_{assist} on the growth and properties of the cBN-rich layer, we prepared a series of cBN-rich film by varying the U_{assist} in a broad range. All the films were deposited on the same template consisted of Si substrate, buffer layer and followed by a cBN-rich seed layer. In particular, the buffer layer is sp^2-bonded with a thickness of d_{buf} = 279 nm. A cBN-rich seed layer with a thickness of d_{seed} = 80 nm was added on top. This seed layer was added in order to promote the nucleation of cBN. Each layer was deposited with a duration of $t_{\mathrm{buf}} = t_{\mathrm{seed}}$ = 30 min. On this same template, five film samples were prepared with different assist beam condition. They were named as cBN013, cBN017, cBN020, cBN003 and cBN018 respectively. Table 4.2 summarizes the conditions for making the samples.

The IR absorption spectrum of a typical buffer layer (Fig. 4.11) only shows two sp^2-related absorption bands, indicating that the buffer layer is mainly sp^2-bonded. The IR absorption band of a typical seed layer is similar to that of the top layer of cBN003 deposited at the same I_{assist} (30 mA) and U_{assist} (450 eV). It shows a prominent sp^3-related absorption band, indicating that the seed layer should contain considerable amount of sp^3 structure. Some cBN nucleuses have already formed at conditions for growing the seed layer.

Table 4.2 Deposition conditions and properties of layered structure film samples with different U_{assist} and d_{buf}.

Sample	$t_{\text{buf}}/t_{\text{seed}}/t_{\text{top}}$ (min)	I_{assist} (mA)	U_{assist} (eV)	$d_{\text{buf}}/d_{\text{seed}}/d_{\text{top}}$ (nm)	$\eta_{\text{cBN-IR}}$ (vol.%)	$\sigma_{\text{top}}/H_{\text{top}}/E_{\text{top}}$ (GPa)
cBN013	(10;10;10) /30/90	20/30/30	(200;280;360) /450/250	279/80/1044	0	1.29/3.4/95
cBN017	(10;10;10) /30/90	20/30/30	(200;280;360) /450/300	279/80/830	0	1.23/3.3/89
cBN020	(10;10;10) /30/90	20/30/30	(200;280;360) /450/360	279/80/607	81	7.99/60/730
cBN003	(10;10;10) / 120	20/ 30	(200;280;360) /450	279/ 510	70	6.59/44/587
cBN018	(10;10;10) /30/90	20/30/30	(200;280;360) /450/550	279/80/274	50	4.76/28/372

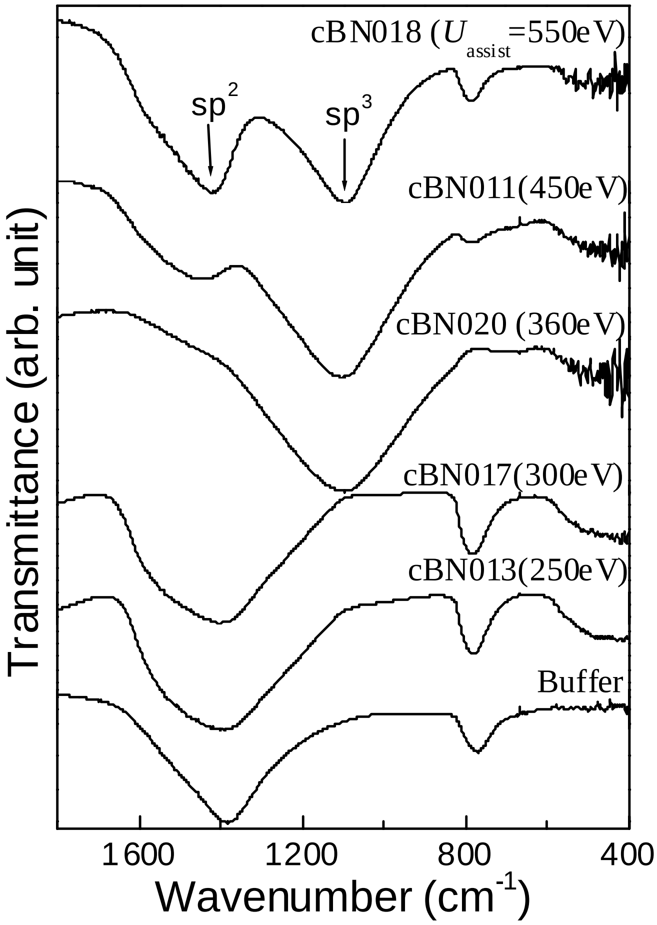

Fig. 4.11 IR absorption spectra of a typical buffer layer, and the top layers of the multilayered samples deposited at different U_{assist} values.

Consider the top layers of these samples. Their thickness d_{top} drops from 1044 to 274 nm when U_{assist} increases from 250 to 550 eV. The data of the cBN content ($\eta_{\mathrm{cBN\text{-}IR}}$) extracted from the IR spectra (Fig. 4.11 and Table 4.2) show that the top layers deposited at low U_{assist} of 250 and 300 eV (cBN013 and cBN017) mainly contain sp^2 phase. Accompanying with the low cBN content, the internal stresses σ_{top}, hardness H_{top} and elastic modulus E_{top} of these two samples have low values in the ranges of 1.23 ~ 1.29 GPa, 3.3 ~ 3.4 GPa, and 89 ~ 95 GPa (Fig. 4.12).

The cBN content of the top layer of cBN020 deposited at a higher U_{assist} of 360 eV increases abruptly to 81 vol.%, corresponding to a sharp on-set of cBN formation (Fig. 4.12). Concomitantly, σ_{top}, H_{top} and E_{top} rise to high levels of 7.99 GPa, 60 GPa and 730 GPa respectively. Though having high value of $\eta_{\mathrm{cBN\text{-}IR}}$ and excellent mechanical properties, the internal stress was so high that cBN020 peeled off shortly after deposition. Therefore, a coating of this type has no practical use.

With the use of higher U_{assist} of 450 and 550 eV (cBN003 and cBN018), $\eta_{\mathrm{cBN\text{-}IR}}$ dropped to 70 and 50 vol.%, and σ_{top} dropped from to 6.59 and 4.76 GPa. The values of H_{top} and E_{top} of cBN003 remained at high levels (44 GPa and 587 GPa), and those of cBN018 dropped to 28 and 372 GPa. Because of having lower levels of compressive stresses compared with that of cBN020, the two samples showed satisfactory adhesion, and did not peel off since the date of deposition. Therefore, the top layer of cBN003 deposited at U_{assist} = 450 eV is identified to be the best compromise between the adhesion and mechanical properties.

A number of mechanisms has been proposed to explain the growth of cBN, including the static stress model [Davis, 1999], dynamic stress model [Matsumoto, 2000; Mirkarimi, 1994], subplantation model [Lifshitz 1989; Robertson 1996], thermal spike model [Hofsäss, 1998] and sputter model [Reinke, 1994; Reinke, 1995; Kulisch, 2003], etc. In this study, we interpret the growth mechanism of the top layer of our films of $U_{\text{assist}} \geq 350$ eV based on a model involving the equilibrium between the generation and relaxation of defects [Davis, 1993; Reinke, 1995; Seitz, 1956]. The model reproduces the observed U_{assist} dependence of σ_{top}.

An ion intruding into the deposit generates defects with a rate of $\zeta\, jU_{\text{assist}}^{1/2}$ [Windischmann, 1991] where j is the ion flux and ζ a proportional constant. Concurrently, the bombarding ions also cause annihilation of defects with a rate of $j(\frac{n}{N})0.016\rho(\frac{U_{\text{assist}}}{U_{\text{o}}})^{5/3}$, where $\rho \approx 1$, U_{o} is the threshold energy to remove a single defect, and n and N are the number densities of the defects and atoms respectively [Seitz, 1956]. The different between the creation and relaxation rates of defects gives the net defect generation rate $R\,(\frac{n}{N})$, where R is rate of atoms incorporating into the films:

$$R\,\frac{n}{N} = \zeta\, j\, U_{\text{assist}}^{1/2} - j\,(\frac{n}{N})0.016\,\rho\,(\frac{U_{\text{assist}}}{U_{\text{o}}})^{5/3} \qquad (4.1)$$

The internal stress in the top layer σ_{top} is assumed to be proportional to the product of $\frac{n}{N}$ and the elastic modulus E_{top}. $\frac{n}{N}$ can be solved from equation (4.1), such that :

$$\sigma_{top} \propto E_{top}\,\frac{n}{N} = \frac{E_{top}\sqrt{U_{assist}}}{\frac{R}{j} + (\frac{0.016\,\rho}{U_o^{5/3}})\,U_{assist}^{5/3}} \tag{4.2}$$

Equation (4.2) is further simplified if $R / j \ll (0.016\ \rho/U_o^{5/3})U_{assist}^{5/3}$. Taking the typical deposition rate of a top layer ≈ 4 nm min^{-1}, the film density ≈ 2 g cm^{-3}, and the average atomic mass = 12.5, R is estimated to be around 10^{19} atoms m^{-1} s^{-1}. The diameter of the assist ion beam is ≈ 3 cm and I_{assist} = 30 mA, such that j is ≈ $2\text{x}10^{20}$ ions m^{-1} s^{-1}. From theses values, R / j is estimated to be about 0.1. On the other hand, taking $\rho \approx 1$, $U_o \approx 3$ eV [McCarty, 1997] and substituting the minimum U_{assist} of 250 eV used in this study, $(0.016\ \rho/U_o^{5/3})U_{assist}^{5/3}$ is about 25. Consequently, R / j is found to drop with U_{assist} in the form of:

$$\sigma_{top} \propto E_{top}\ U_{assist}^{-1.167} \tag{4.3}$$

Equation (4.3) reproduces the observed U_{assist} dependence of σ_{top} for $U_{assist} \geq$ 360 eV (dash line in Fig. 4.12). One important implication of the above discussion is that the change in U_{assist} alters the balance between the creation and annihilation of defects, accompanying with the changes of internal stresses and sp^3 contents. For the compromise between the adhesion and mechanical properties of cBN-rich film, the optimum value of U_{assist} is identified to be 450 eV in this study.

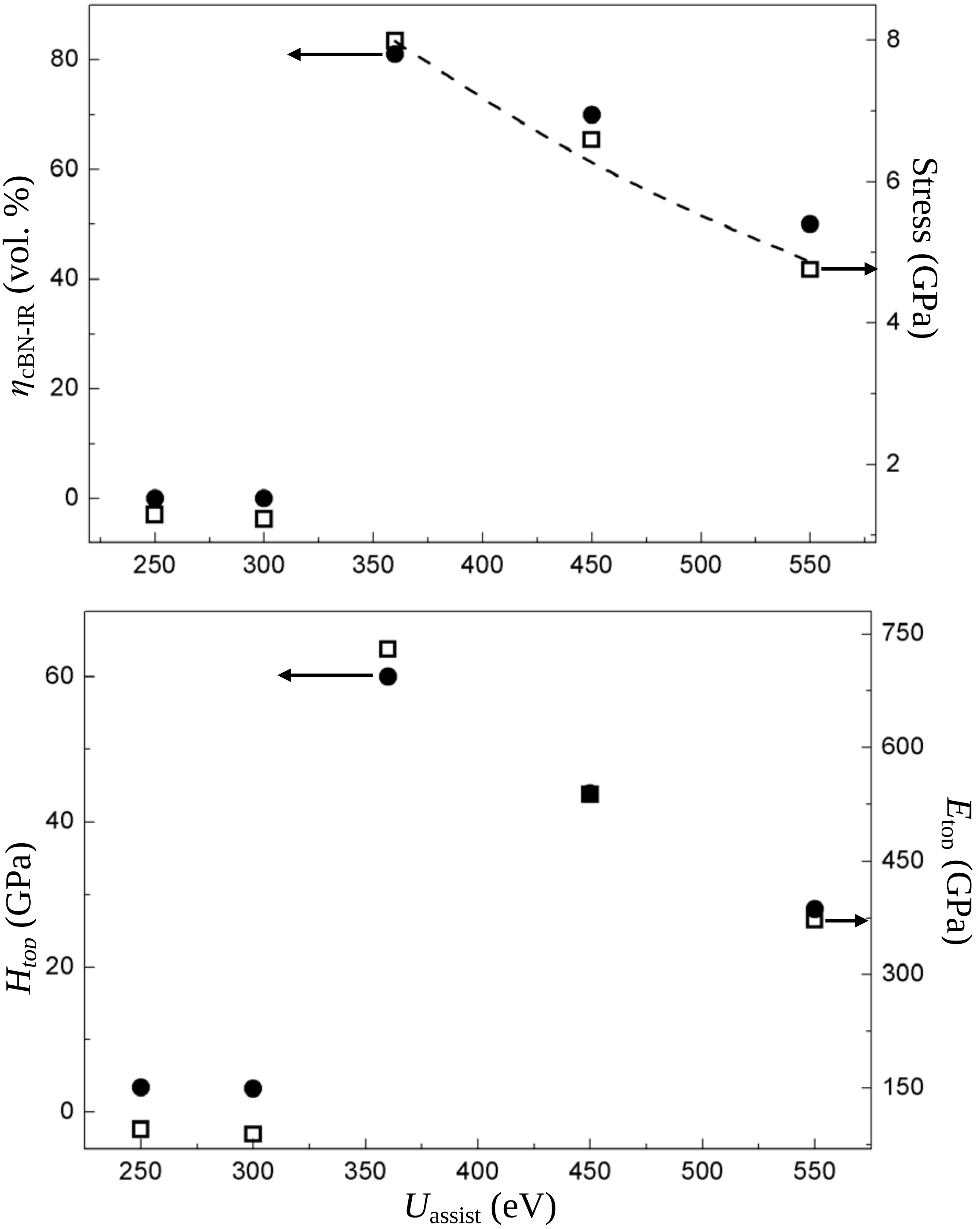

Fig. 4.12 Assist beam energy U_{assist} dependence of (a) the cBN volume fraction η_{cBN-IR} and internal stress σ_{top}; (b) the hardness H_{top} and elastic modulus E_{top} of the top layers of the multilayered samples.

4.5.2 *Appearance of a thin sp^2 surface layer and its implications on the growth mechanisms of the cBN-rich layer*

Referring to Fig. 4.10 (a), a sp^2-bonded BN layer is always found on the surface of cBN-rich layer, where is considered as the growth front of the cBN-rich film [Hofsäss, 1998; Hofsäss, 2002; Lifshitz, 1990].

As described before, the cBN growth is a dynamic process with the momentum transfer from intruding ions to constitutional atoms and the balance between the creation and annihilation of defects.

The momentum transfer also makes possible for the constitutional B and N ions penetrate into the subsurface layer, and contribute to the cBN grain growth. Meanwhile, for intruding ions penetrating into the sub-surface layer, their energies decrease with the penetration depth. We note that the penetration range of particle of 100 – 500 eV is about 1 – 2 nm according to the simulation by TRIM (Fig. 4.4), which is fairly close to the dimension of the surface layer observed [Hofsäss, 1998; Lifshitz, 1990]. While the deeper-penetrated ions may contribute to the cBN grain growth, the shallow penetrated ions are expected to create larger amount of defects than those can be annihilated by the ion-annealing process. The accumulation of these defects eventually leads to lattice damage and phase transformation from cBN to sp^2-bonded BN.

This argument was supported by the result of a recent study, which showed that argon ion irradiation with energy and fluency of 500 eV and 5x10^{16} ions cm^{-2} on a cBN crystal would drive a substantial portion of the cBN phase within the ion penetration depth of 1.1 nm to transform into the sp^2-bonded BN phases [Hui, 2002].

This is consistent with the presented experimental data of film cBN023 (deposited using 450 eV nitrogen ion). Moreover, Hofsäss *et al.* have also observed a sp^2 BN surface layer covering the cBN grains underneath in a film deposited using 5 keV ion beam which is much highly energetic [Hofsäss, 2002].

This argument is further strengthened by the difference observation with introducing N ions at 10 mA and 100 eV to bombard the film surface of Sample cBN023 (Fig. 4.10 (a)) for 10 minutes (Fig. 4.13). The 100 eV nitrogen ions only "cleaned" the film surface region without further introducing any transformation of sp^2-bonded BN on top of cBN. Applying the low energy ion bombardment, the sp^2-bonded BN layer, which is highly defected and loose structure, was easy to be sputtered off. Moreover, this low energy ion bombardment would not cause any phase transformation from cBN to sp^2-bonded BN which was directly observed in Fig. 4.13.

The presence of sp^2-bonded BN surface layer results from the equilibrium between the ion irradiation damage (layer creating) and sputter etching (layer eliminating). Intuitively, controlled conditions have to be achieved, so that the sp^2 bonded surface layer can be within certain thickness, which allows the deep-penetrated B and N species reach the cubic phase and contribute to further growth. The existence of ion energy threshold for cBN growth [Mirkarimi, 1994], the sp^2 bonded BN surface layer observed in samples deposited with high ion energy [Hofsäss, 2002], and the theoretical TRIM calculation [Lifshitz, 1990] support the sub-surface growth model for cBN.

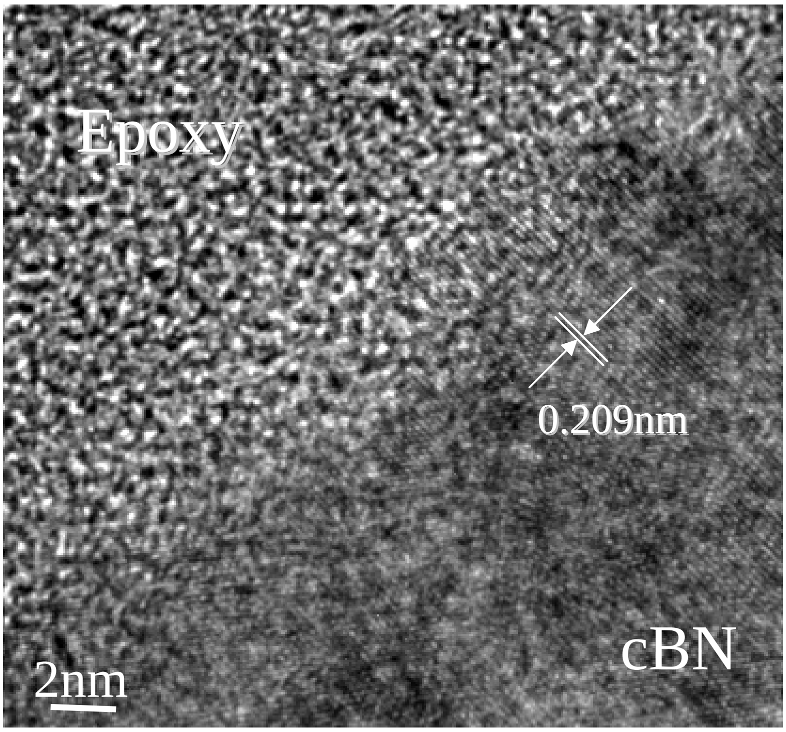

Fig. 4.13 High-resolution TEM image taken from cBN023 after 100eV N_2^+ irradiation, showing the structure of the BN film close to the film top surface. Only cubic boron nitride is observed

Chapter 5

Boride / cBN-Rich Films Prepared by Multilayered Approach

5.1 Motivation of Using Multilayered Approach

Results of Chapter 4 illustrate that the addition of a thick sp^2 BN buffer layer can greatly promote the tolerable thickness of a cBN-rich layer to be deposited on top. However, the presence of such a sp^2-bonded region is still undesired, since it may weaken the linkage between the top cBN-rich layer and the substrate.

The second reason responsible for the poor adhesion of the cBN-rich layer to substrate is the presence of compressive stresses in the deposits. Ion-induced stresses are usually introduced deliberately via ion bombardment to assist the growth of the sp^3 phase, but the presence of strong compressive stresses would be unfavourable to the adhesion of the film to the substrate.

The third reason causing the detachment of a cBN-rich layer from the substrate may be due to the inclusion of surplus boron in the film. The excessive boron atoms could be rather active and tend to react with the moisture from the air [Kim, 1998]. The reaction was supposed to be describable with the formula:

$$\frac{13}{2}O_2 + 8B + H_2O \rightarrow 2[(B_2O_3)_2(OH)], \qquad \Delta G = -2800\text{kJ / mol}$$

Such an oxidation process could lead to drastic volume change and hence accelerates the detachment of the film from the substrate.

In this chapter, we propose a new deposition scheme with the intention to cope with the abovementioned factors. The scheme consisted of the following steps.

(i) First, the substrate was pre-cleaned by an argon ion beam with energy U_{assist} = 600eV and current I_{assist} = 54mA.

(ii) Second, a thick sp^2 buffer layer is deposited on the substrate.

(iii) Then, a zirconium (Zr) metal layer was deposited on the substrate prior to the deposition of the sp^2 BN buffer layer (Fig. 5.1).

(iv) Next, a gradient sp^2-bonded BN buffer layer was deposited at 680°C according to the procedures described in Chapter 4.

(v) A thick cBN-rich layer was then added on top at the same temperature of 680°C.

(vi) An annealing process at 850°C was thus performed for initiating a solid-state reaction between the Zr layer and the soft buffer layer via atomic diffusion process. This procedure plays the central role of the whole deposition scheme, since according to our conjecture, the possible solid-state reaction should lead to the formation of a hard boride layer to replace the original soft Zr layer and the sp^2 BN buffer layer. In addition, the post-annealing process may further eliminate some internal stresses in the layer stack.

(vii) The final procedure was to irradiate the cBN-rich top surface with an N_2^+ beam in order to saturate any possible excessive boron atoms in the cBN-rich layer. Fig. 5.1 shows expected structural transition as described above, and the ideal structure after the completion of the process (right side).

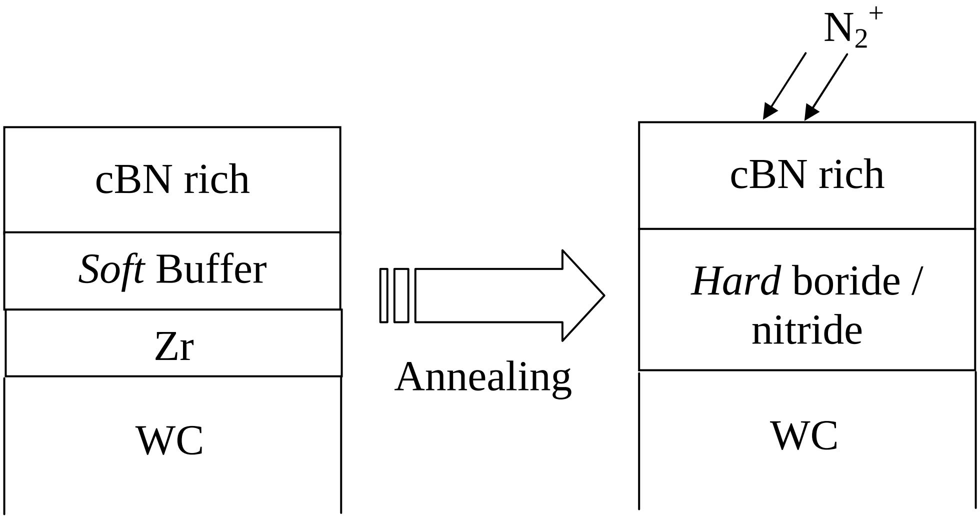

Fig. 5.1 A schematic diagram of the multilayered approach.

5.2 Investigation on the Reaction between the Zr Layer and sp^2 BN Buffer Layer

Referring to the design of the above proposed scheme, interlayer diffusion between the Zr layer and the sp^2-bonded buffer layer may occur in two different steps. They are:

Step (v) deposition of the top cBN-rich layer performed at a relatively high temperature of 680°C for a period of 120 minutes; and

Step (vi) post-annealing of the layer stack at 850°C.

The duration of Step (v) and the thicknesses of the two layers must be carefully assigned in order to prevent premature reaction of the two layers in this step. Otherwise, zirconium atoms would diffuse excessively into the cBN-rich layer in Step (vi). Based on this consideration, we performed a preliminary test to see how fast the two layers react in Step (vi). In the test, we prepared a sample (hBNZr001) consisting of a zirconium layer and an sp^2 BN buffer layer, and then annealed the bilayer at 680°C for 120 minutes to simulate the situation of depositing the top cBN-rich layer. TEM analysis was then performed to see how the layers reacted. The data were found to be useful in assigning the duration and thicknesses of individual layers for the complete deposition scheme as proposed.

The preparation conditions of Sample hBNZr001 are summarized in Table 5.1. In brief, a Zr layer was first deposited, followed by the deposition of a sp^2-bonded BN buffer layer with the same condition as that used for preparing the sp^2-bonded BN buffer layer of cBN023 (Table 4.1 of Chapter 4). The bilayer was then annealed at 680°C for 120 min. These setting simulated the situation for depositing a cBN-rich layer.

Table 5.1 Fabrication conditions of Sample hBNZr001.

Step	Purpose	t (minute)	U_{assist} (eV)	I_{assist} (mA)	T_s (°C)
1	Cleaning	10	600	54	680
2	Zr	60	OFF	OFF	
3.1	Gradient buffer layer	3	200	20	
3.2		3	280	20	
3.3		4	360	20	
4	Annealing	120	OFF	OFF	

Fig. 5.2 shows the image of the cross section of Sample hBNZr001. It is seen that the film has two layers. According to the sequence of deposition procedures, the darker layer in contact with the substrate should undoubtedly be a Zr-rich layer. Since a Zr atom is heavier than a B atom or N atom, it should have a stronger electron scattering power. As such, the contrast of the image would be dominated by the distribution of the Zr atoms. Therefore, the boundary between the dark region and the bright region should be interpreted as the diffusion front of the Zr atoms. Fig. 5.2 also shows the magnified image taken at a point inside the brighter region, which is marked with a letter "*A*". The image shows some fringes having a spacing of 0.366 nm, verifying that the atomic planes are the (0002) basal planes of sp^2-bonded BN. The fringes are roughly perpendicular to the substrate surface, showing preferentially alignment of the basal planes. The bright layer is thus reconfirmed to be sp^2-bonded BN, in accordance with the conditions applied for preparing the BN layer of Sample

hBNZr001. We come to the conclusion that the Zr layer and the buffer layer did not completely react with each other in this process.

In addition, estimated from the coating rate of Zr film and sp^2 BN layer, if no interlayer diffusion occurs in the bilayer, the thicknesses of the Zr and sp^2-bonded BN buffer layer are expected to be 360 and 122 nm respectively. However, according to the cross-sectional TEM image of the sample, the thicknesses of the Zr-containing layer was measured to be 413 nm, which was larger than the reference expected value of 360 nm under the assumption of no diffusion. Moreover, the thickness of the sp^2 layer was 68 nm, smaller than the expected value of 122 nm under the assumption of no diffusion. This suggests that some interlayer diffusion did occur between the two layers, though they did not completely react. Further, it is interesting to note that the sum of the observed thicknesses of the two layers is 481 nm, which is almost equal to the sum of the expected thicknesses of the two layers under the assumption of no interlayer diffusion, i.e. 482 nm. It is suggested that the atoms of the two layers diffused and mix together, while the overall thickness of the two layer structure is not altered.

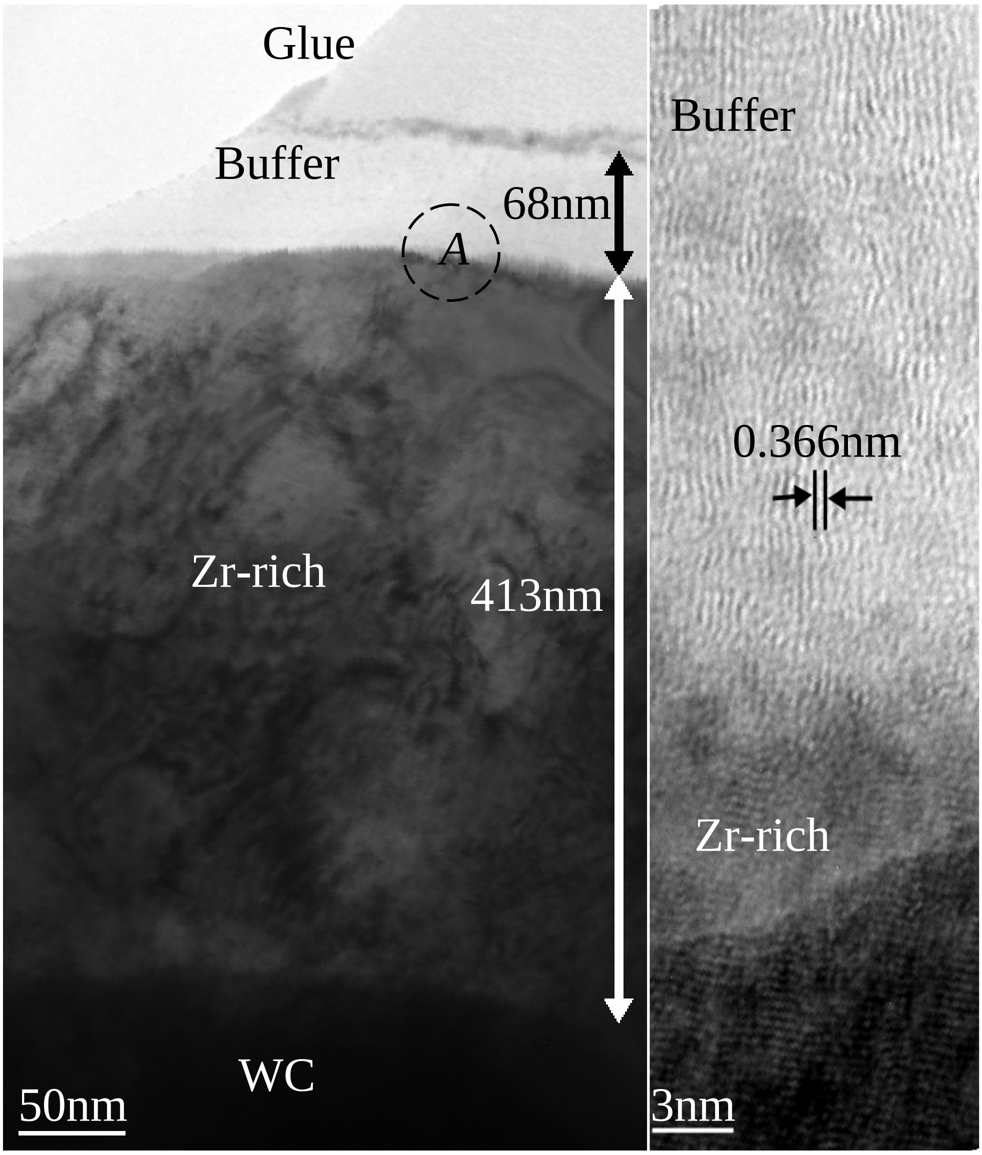

Fig. 5.2 Cross-sectional TEM image (left), and high-magnification image of a region *A* (right) in Sample hBNZr001.

Detailed depth profile analysis of the composition and the chemical states of the elements were carried out with the use of X-ray photoelectron spectroscopy (XPS). To perform a depth profile analysis, an Ar^+ ion beam was used to sputter the film material layer by layer from the top surface towards the interior. Fig. 5.3 shows the results. The left part of the figure presents the depth profile of the elemental composition, from which some details on the diffusion process could be obtained. The carbon and oxygen contents were found to be around 14 and 4 at.%, almost independent of the depth from the film surface. However, their presence does not influence both the structure and properties of the films. Up to a depth corresponding to a total sputtering time of 10 min, the elemental composition is non-stoichiometric, with the B content exceeding the N content. Meanwhile, the B-to-N ratio is approximately a constant. The Zr content is negligibly small. For deeper regions corresponding to longer sputtering time of 10 - 23 min, the boron content drops, while the Zr content increases remarkably. This result gives additional support to the conclusion that the two layers have not been completely reacted in this process.

The right side of Fig. 5.3 shows the change of the chemical structure as a function of depth. The change of the chemical bonding across the boundary of the two layers can be monitored. The Zr-3d photoelectron spectrum collected at a depth corresponding to a sputtering time of 18 min displayed. This depth should correspond to the central point of the intermixing region, at which the B and Zr contents are roughly the same. The Zr-3d photoelectron spectrum of the film sample can be fitted by using a linear combination of the standard Zr-3d spectra of metal Zr, ZrN and ZrB_2, suggesting that the film material at this depth can be regarded as the composite of these three components.

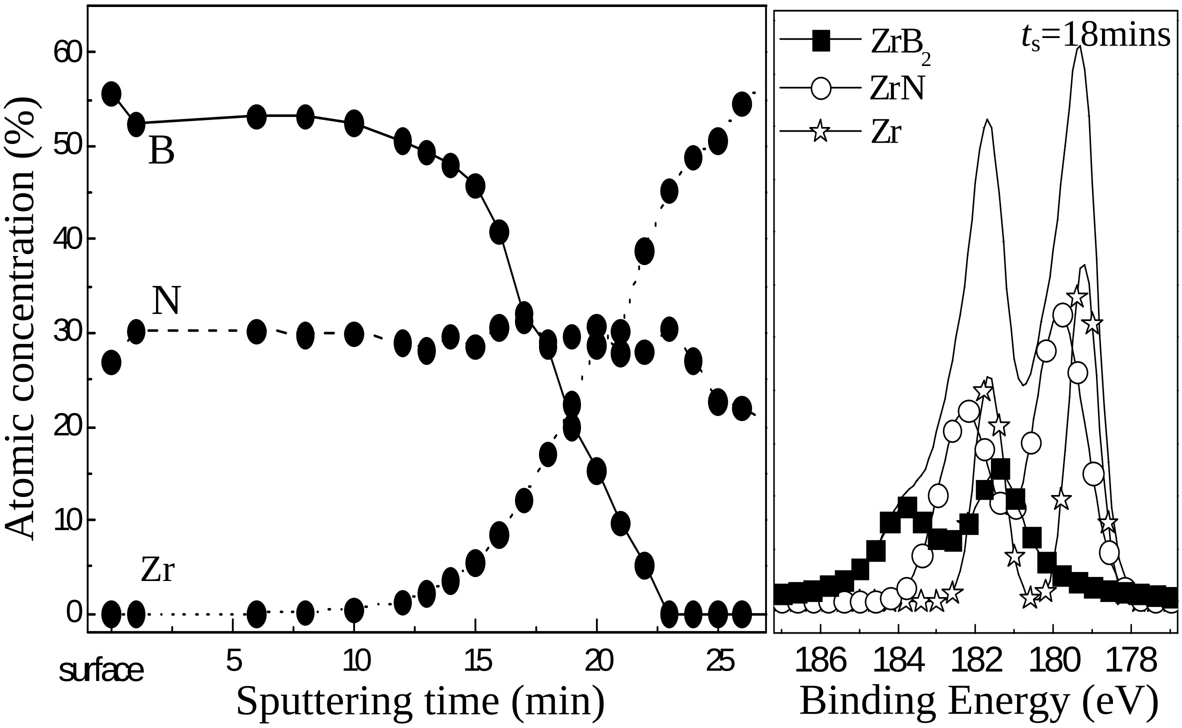

Fig. 5.3 The depth profiles of B, N and Zr in Sample hBNZr001 (left). Zr-3d photoelectron spectrum of hBNZr001 at region of similar B and Zr contents, and the best fit to the spectrum (right).

5.3 Boride / cBN-Rich Films

The results of the previous section show that the Zr layer and the sp^2-bonded BN buffer layer would not completely react at 680^{o}C in a period of 120 minutes. We then fabricated samples by applying the whole proposed multilayered deposition scheme. In this section, we present the results of a typical sample, named as chBNZr001. Detailed preparation procedures are listed as follows. The values of the parameters are listed in Table 5.2.

Step 1: Preparation of tungsten carbide (WC) substrate

Tungsten carbide (WC) was selected as the substrate material, because we wanted to examine the performance of the film deposited on such a standard cutting tool material. To prepare the substrates, WC slices with a thickness of 300 µm were cut from a commercial WC cutting tool bought from a metal shop. According to the XPS analysis, the material contains 6 at.% cobalt (Co) binder. The slices were then properly polished by 0.25 µm diamond paste and cleaned, and loaded into the vacuum chamber. Before deposition, the substrate was heated up to 680^{o}C, and pre-sputtered by Ar$^+$ beam with energy and current of 600 eV and 54 mA, respectively, for a period of 10 minutes.

Step 2: Deposition of a zirconium (Zr) layer for 60 minutes

The substrate was kept at 680^{o}C. A Zr layer was deposited by sputtering a Zr target with an Ar$^+$ ion beam of U_{spu} = 1200 eV and I_{spu} = 70 mA. The assist gun was not turned on. No nitrogen gas was admitted into the chamber to avoid nitridation of the Zr layer.

Step 3: Deposition of a gradient sp^2 BN buffer layer

The substrate was kept at 680°C. The boron target was sputtered with an Ar^+ beam of 1200 eV and 70 mA. Simultaneously, the substrate was bombarded by an assist beam containing Ar^+ and N_2^+ ions with the U_{assist} value increased stepwise from 200, 280 to 360 eV, and the I_{assist} value fixed at 20 mA. The deposition time for this layer was 10 minutes. Ar and N_2 gases were admitted into the assist ion gun with flow rates equal to 15.3 and 12.0 sccm respectively.

Step 4: Deposition of a cBN-rich top layer for 120 minutes

All the parameters used in Step 3 were not changed, except that the assist beam energy and current were increased to 450 eV and 30 mA. A top BN layer was deposited. The process lasted for 120 min, and the deposit was proved to be cBN-rich later on.

Step 5: Post-annealing at 850°C for 60 minutes

In this step, the two ion guns were turned off. The substrate was heated to 850°C for post-annealing. Meanwhile, 5.0 sccm of N_2 gas and 5.0 sccm of Ar gas were admitted into the chamber to keep the deposits in an inert gas atmosphere. This purpose of this step was to activate the solid state reaction between the buffer layer and the Zr layer. We expected to create a new layer consisting of borides and/or nitrides, which if successfully formed could replace the relatively soft gradient sp^2-bonded BN buffer layer so as to enhance the bonding strength between the top cBN-rich layer and WC substrate. We further note that Zr was selected to make the metal layer for this purpose, because it was known to be an effective binder to mix with cBN powders for sintering bulk BN ceramics. The sintered bulk BN sample was reported to contain zirconium boride and zirconium nitride at the grain boundaries [Benko, 1998].

Step 6: Ion bombardment on the surface of the top layer stack with a $N_2^{\pm}$ beam for 3 minutes

A N_2^+ beam of U_{assist} = 100 eV and I_{assist} = 8 mA was generated by admitting 20.0 sccm of N_2 into the assist gun for irradiating the substrate. We expected to initiate reaction between the incident nitrogen ions and any excess boron atoms in the deposits, so as to passivate the reactivity of the deposits with the moisture in the atmosphere.

We expected that after Step 5, the 4-layered structure (including the substrate) as shown in Fig.5.1 (left) would be converted into a 3-layered structure as shown in the same figure (right). The layer would contain a boride composite layer to replace the original sp^2 layer. Some residual stresses would be released during annealing at 850°C. Excess boron possibly existing in the top cBN-rich layer would be exhausted. We further expected that a cBN-rich layer with acceptable adhesion and good mechanical properties would be obtained.

Table 5.2 Fabrication conditions of Sample chBNZr001.

Step	Purpose	t (minute)	U_{assist} (eV)	I_{assist} (mA)	T_s (^{o}C)
1	Cleaning	10	600	54	680
2	Zr	60	OFF	OFF	
3.1	Gradient buffer layer	3	200	20	
3.2		3	280	20	
3.3		4	360	20	
4	cBN-rich top layer	120	450	30	
5	Annealing	60	OFF	OFF	850
6	N_2^+ irradiation	3	100	8	

We now present the results of the characterization of Sample chBNZr001. According to the deposition scheme for preparing chBNZr001, the film is expected to consist of three layers (Table 5.3), namely, a 360-nm Zr layer on top of the WC substrate, a 122-nm sp^2 BN buffer layer, and a 479-nm cBN-rich top layer (Table 5.3). The actual thicknesses of the layers were then examined by TEM technique. Any deviation from the hypothetical values would imply the occurrence of interlayer diffusion.

Table 5.3. Expected and observed layered structures of the samples.

Sample		Substrate	1st layer (nm)	2nd layer (nm)	3rd layer (nm)
hBNZr001	Expected	WC	Zr (360)	sp^2 buffer (122)	
	Observed		Zr-rich (413)	sp^2 buffer (68)	
chBNZr001	Expected	WC	Zr (360)	sp^2 buffer (122)	cBN-rich (479)
	Observed		Zr-rich (775)	----- -----	cBN-rich (72)

Fig. 5.4 shows the cross-section TEM image of the sample. Only two layers are seen. The first layer just adjacent to the substrate is obviously a Zr-containing layer. The top layer shows a brighter contrast, which is expected to be a BN layer. To identify its structure, a selected area electron diffraction (SAED) was taken from a point *B* in this region. The pattern shows diffraction spots attributable to the (111) and (220) planes of the cBN structure. The distribution of the spots further indicates that the cBN grains have preferred orientation, namely with the [111] planes aligned along the growth direction. In addition, the high-magnification image taken at the point *C*, located at the transition region between the Zr-rich and cBN-rich layers, shows that the cBN phase appears quite abruptly without any sign of the sp^2-bonded structure. This gives direct evidence to verify that the sp^2-bonded BN buffer layer deposited in Step 3 has been completely reacted with the Zr layer.

According to the results of hBNZr001 described in Section 5.2, we expect that the Zr layer and sp^2-bonded BN buffer layer in Sample chBNZr001 have not completely reacted with each other just after the Step 4 for depositing the top cBN-rich layer at 680^{o}C for 120 min. Complete reaction between the two layers should occur in Step 5 (post-annealing process at 850^{o}C).

As summarized in Table 5.3, the observed thickness of the Zr-rich layer is 775 nm, much thicker than the expected value of 360 nm under the assumption of no interlayer diffusion. On the other hand, the observed thickness of the cBN-rich layer is 172 nm, much thinner than the expected value of 479 nm under the assumption of no interlayer diffusion. In addition, the overall thickness observed from the TEM image is 947 nm, which is very close to the sum of the expected total thicknesses 961 nm under the assumption of no interlayer diffusion. Combining all these features, it is reasonably to infer that the Zr layer and the sp^2 BN buffer layer have already completely reacted. Because of the stronger electron ability of a Zr atom, we regarded the boundary between the dark and bright regions in the TEM image (Fig. 5.4) as the diffusion front of Zr.

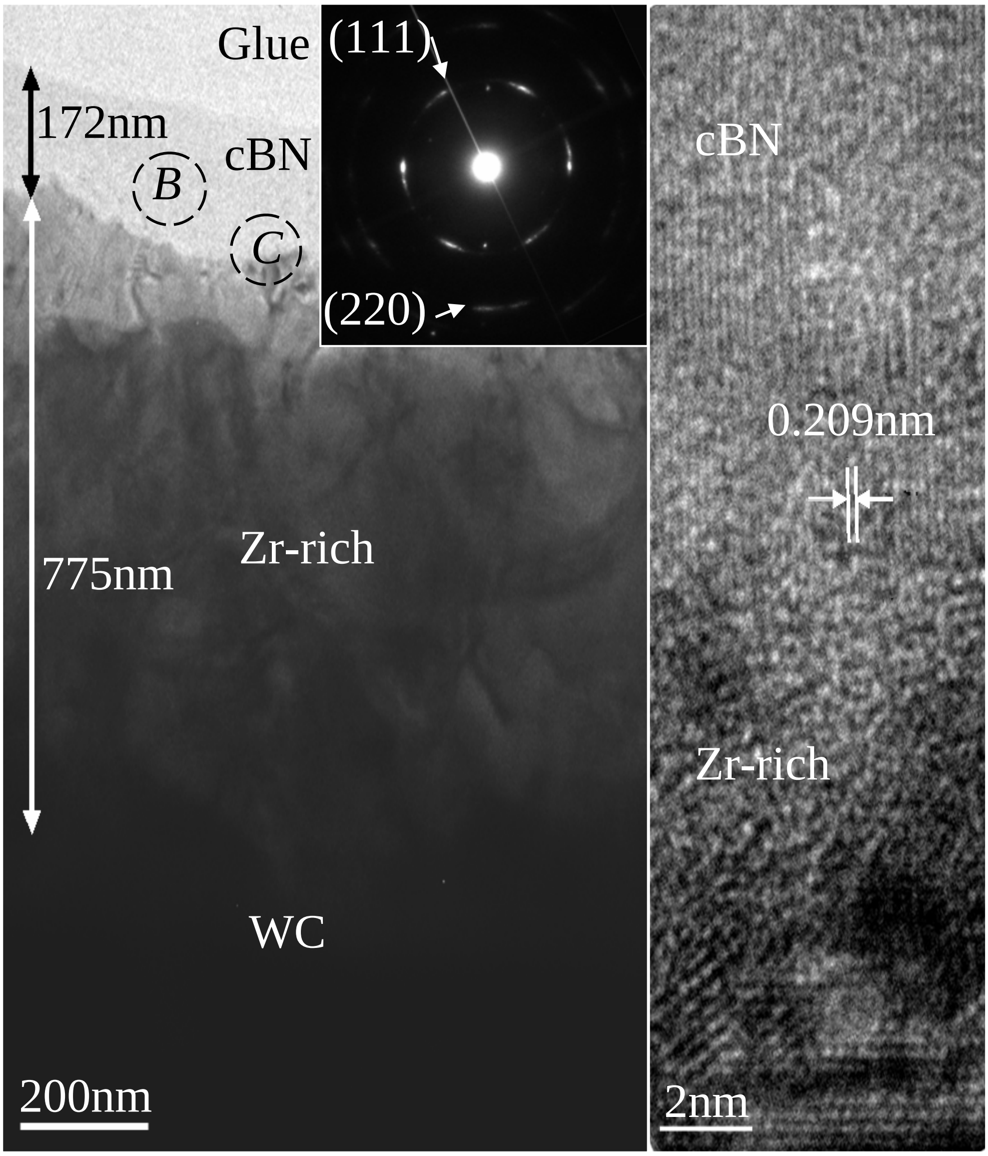

Fig. 5.4 Cross-sectional TEM image (left); electron diffraction pattern of region *B* (top), and high-magnification image (right) of region *C* in chBNZr001.

We then present the results of depth profile analysis. The compositional and structural information on the sample were analysed as functions of depth by using XPS. This was conducted by successive sputtering with an Ar^+ ion beam of 1 keV, with each step lasting for 10 min. The ion-induced damages could be suppressed by post-ion irradiation with the beam energy successively reduced from 500 to 300, and then to 100 eV, each lasting for 1 min.

The relative contents of B, N, C, Zr and W were measured as functions of sputtering time to reflect their variation along the depth. Fig. 5.5 shows the results. We note that 5 at.% of carbon and 10 at.% of oxygen were detected mostly independently from the film surface (not shown), but their seem not to affect both the film structure and properties, and hence are not considered in the discussion. Near the surface of the cBN-rich layer, the B and N contents are about the same, and the Zr content is negligibly small. With increasing depth, both the B and N contents drop, and the Zr content increases on the contrary. The observed progressive change of the elemental composition with increasing depth is suggested to originate from some diffusion processes of the atoms in the layers.

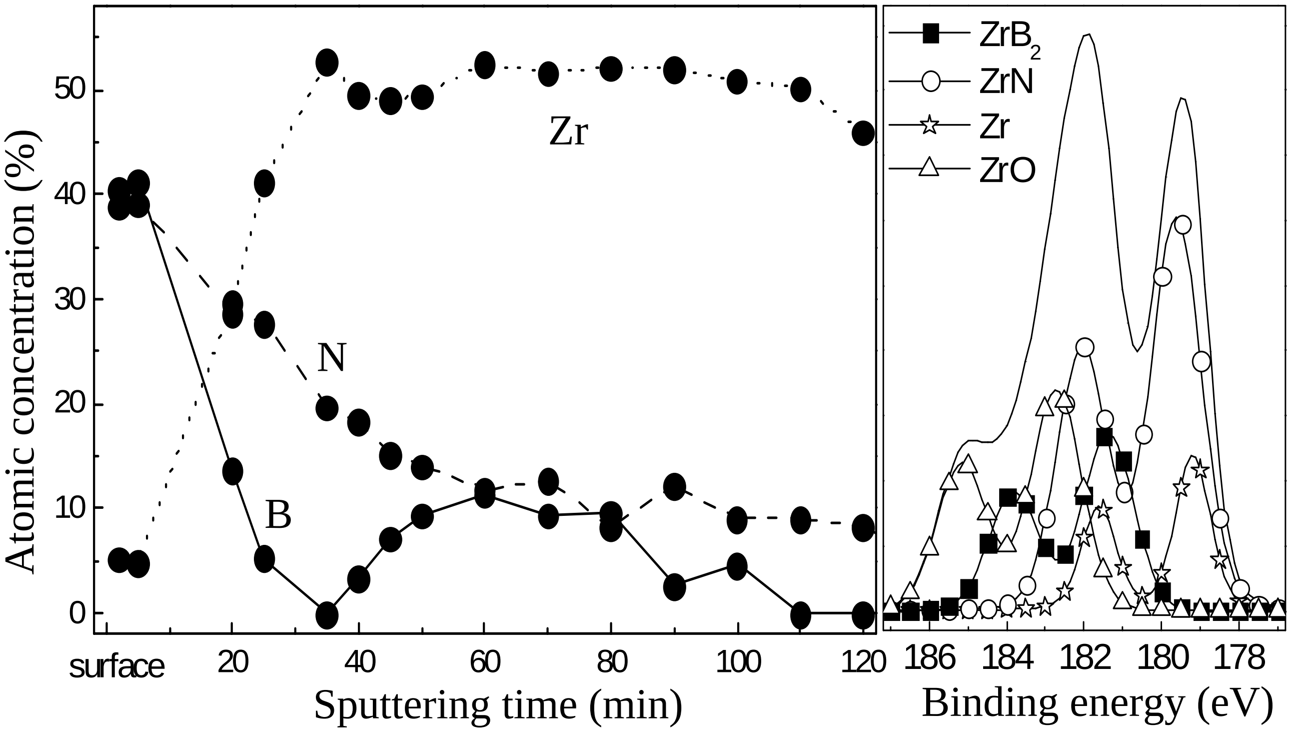

Fig. 5.5 Compositional depth profiles (left), and the fitting to the Zr-3d photoelectron spectrum (right) taken from a point in chBNZr001 having similar B and Zr contents.

It is interesting to point out that the depth profile of B content as shown in Fig.5.5 does not diminish monotonically with increasing depth, but a local hump is observed at depths corresponding to the sputtering time of 40 - 80 min. The range of the hump should cover the locations of the sp^2-BN layer or the cBN-rich layer if no diffusion occurs. The TEM-EELS mapping of B as shown in Fig. 5.6 (a) supports this conjecture. Aggregation of B atoms (presented as a bright area) is found to locate at about 250 – 480 nm below the film surface, falling in the region where a cBN-rich layer is expected to be deposited.

Finally, the chemical structure at the intermixing region was examined by observing the Zr-3d photoelectron spectrum collected from a point where the B and Zr contents are approximately equal (Fig. 5.5). Good fit to the spectrum can be achieved if a model consisting of the standard spectra of metal Zr, ZrN, ZrB_2 and ZrO is used. This result suggests that the material at the intermixing region is indeed a composite consisting of metal Zr, some nitride, boride and oxide. The detected inclusion of oxygen may originate from the residual impurities existing in the chamber. The impurities entered the sample mainly during the high temperature annealing at 850^{o}C. According to the fitting, the Zr atoms are distributed in the four phases in a ratio of 1 : 3.4 : 1.5 : 1.9.

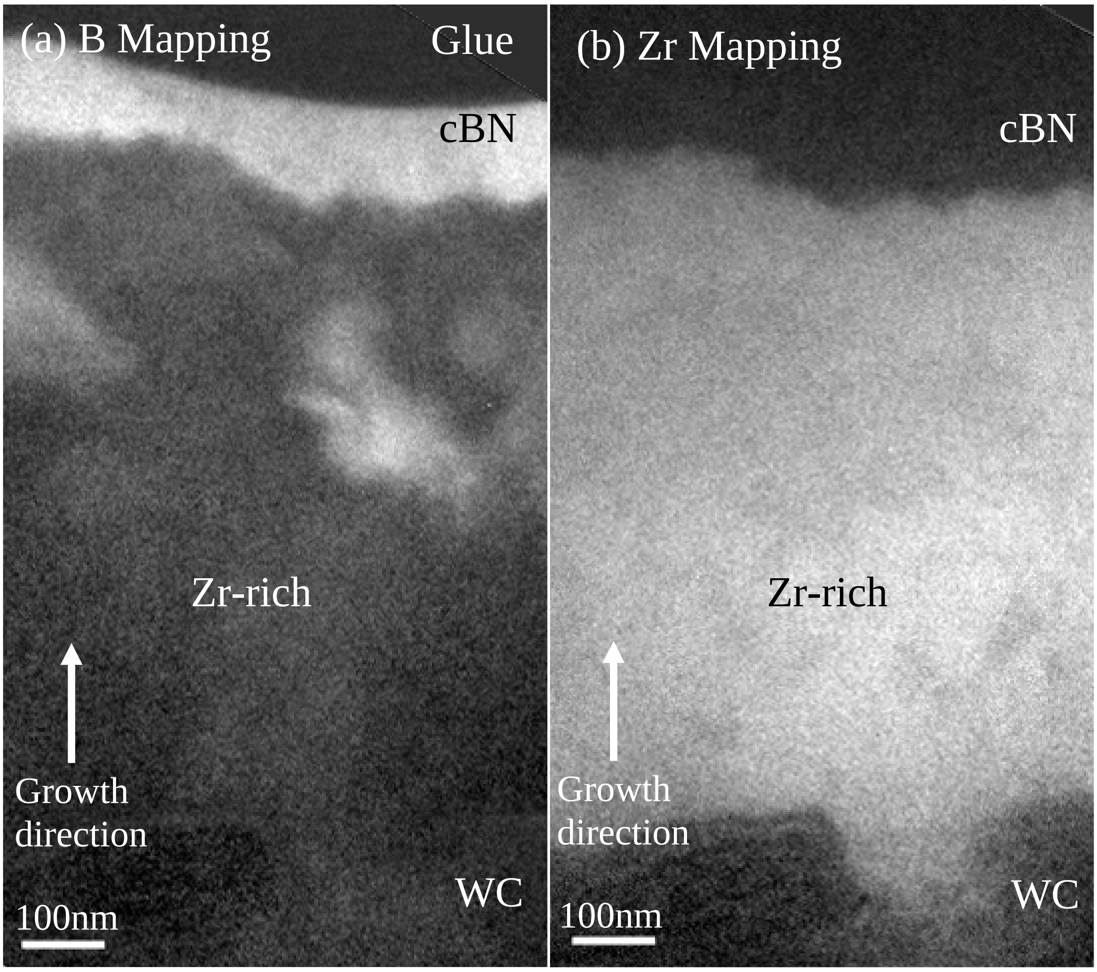

Fig. 5.6 TEM-EELS mappings of B (left) and Zr (right) of Sample chBNZr001.

Chapter 6

Composite Films containing sp^3 BN Nanoclusters

6.1 Motivation of Producing BN films containing sp^3 Nanoclusters

All the methods described in the previous chapters are aimed at producing thick crystalline cBN-rich films having acceptable adhesion to substrates. These schemes are common in applying highly energetic ion assist to force the nucleation and growth of cBN grains, and so it is inevitably to have significant resputtering effect, low deposition rate (e.g. typically 3.6 nm min^{-1} for a cBN-rich layer), and high internal stress level. The last one is directly related to the peeling off problem. In addition, the schemes have been very complicated, and any further modifications would make the processes to be even more difficult to implement. This leads us to ask a fundamental problem that whether crystalline BN film is always necessary in real applications, or whether any non-crystalline BN phase analogous to diamond-like carbon with sp^3 short-range order and acceptable mechanical properties could be fabricated and applicable in some cases.

Unlike diamond-like carbon, non-crystalline BN structure is a new concept conceived by the author, which has not been reported or even proposed by others. This conception is mainly inspired by the accidental finding of some highly disordered “sp^3 nanoclusters” in the 3rd sub-buffer layer of Sample cBN023 (Section 4.4.2, Fig. 4.6). These nanoclusters are formed at a temperature of 680°C, but we further conjecture that similar nano-sized sp^3 structure can be created at lower temperature if appropriate ion assist condition used. The use of low temperature condition is inspired from the P-T phase diagram of the B-N system as shown in Fig. 6.1. Referring to the boundary between the hBN and cBN phases, named as Corrigan-Bundy boundary or C-B line [Corrigan, 1975], one sees that a lower temperature favours the formation of the sp^3 phase at a lower pressure environment. Additional support was from Feldemann, who reported that the cBN films would be produced at room temperature condition [Feldenmann, 1999].

Our proposal, different from Feldemann's scheme, aims at producing nano-sized sp^3 clusters instead of cBN grains at low temperature environment. Experimentally, this can be realized with the substrate to be unheated (substrate heater off). Ion assist is still required as it can produce stresses to emulate the presence of a pressure. If the hypothetical sp^3 nanostructure can be produced, it would be expected to have some advantages as follows.

(i) No substrate heating is required, so that the power consumption of the process is lower and the duration of a deposition cycle is shorter compared to those required for producing a polycrystalline cBN film.

(ii) The film may be a nanocomposite containing both the sp^2 and sp^3 structures. As such the stress level could be lower than that of a polycrystalline cBN film, and the risk of peeling off is less. The film could retain some novel properties of the cBN structure, such as having an appreciable hardness value and chemical inertness.

In this chapter, we present the results of a study for exploring the possibility of producing BN films containing non-crystalline sp^3 structure. The key point is to deposit the films on unheated substrates under appropriate ion assist. The influence of varying the substrate temperature T_s and assist beam energy U_{assist} are also investigated and discussed.

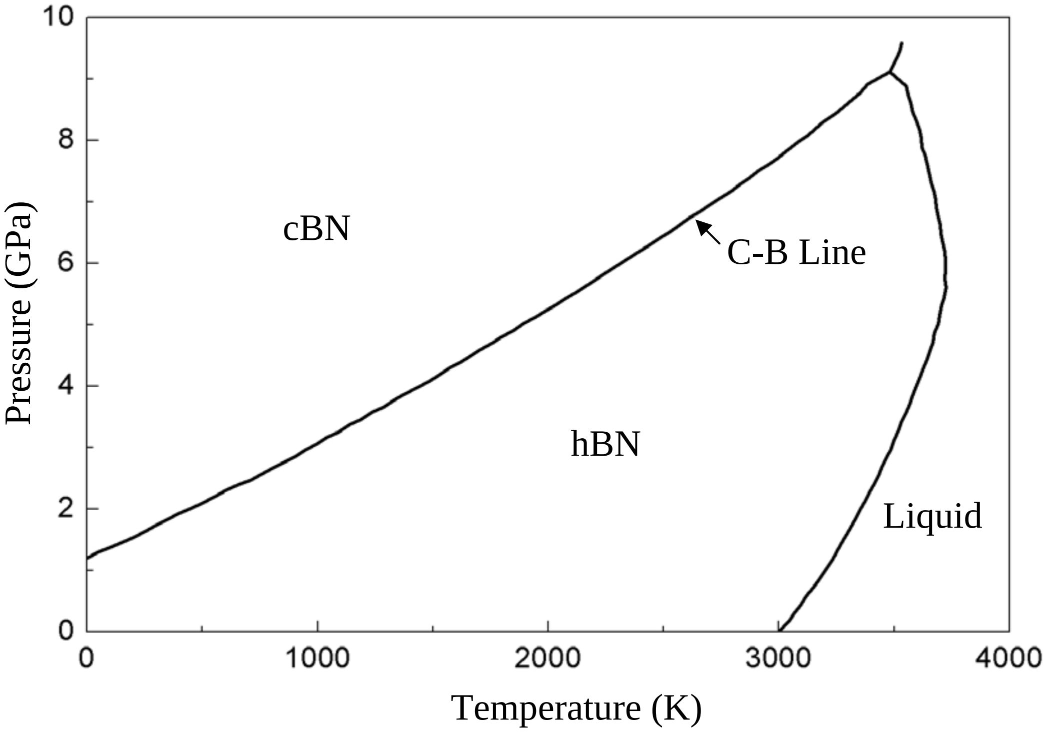

Fig. 6.1 Phase diagram of the boron nitride system. [Corrigan, 1975]

]

6.2 Preparation of BN Films on Unheated Substrates under Ion Assist

The preparation conditions of the samples deposited on unheated substrates for this study are listed in Table 6.1. The deposition runs were all single-step processes, in which the settings of all the parameters were kept constant. Silicon (Si) substrate was first pre-cleaned by an Ar^+ beam of 600 eV and 54 mA. A boron target was then sputtered with an Ar^+ beam of an energy U_{assist} = 1200 eV and current I_{assist} = 70 mA. An assist ion beam containing N_2^+ and Ar^+ ions was directed to bombard the substrate at the same time. The deposition time was typically 60 minutes, except Sample aBN067 which deposition time was 120 minutes. Although the substrate heater was not turned on, the substrate temperature T_{s} was stabilized at 85 - 210$^{\text{o}}$C due to the irradiation by the assist ion beam. Higher assist beam energy U_{assist} causes a higher T_{s}. The lower bound of the T_{s} range was achieved with the use of a water-cooled substrate holder as described in Section 2.1.

Table 6.1 shows the U_{assist} values used to deposition the samples. It was varied in the range of 100 - 550 eV. The properties of the films produced were compared so as to observe the influences due to the change in U_{assist}. In this chapter, we also compare the properties of the samples deposited on unheated substrates with those prepared at higher T_{s} in the range of 350 - 800$^{\text{o}}$C. The preparation conditions and main properties of the samples for the comparison are listed in Table 6.2. The influences of increasing T_{s} on the formation of the hypothetical sp^3 nanostructure are discussed.

Table 6.1 Preparation parameters of the film samples deposited on unheated substrates, and with U_{assist} varying from 100 – 550 eV.

Sample	U_{assist} (eV)	I_{assist} (mA)	T_{s} ($^{\mathrm{o}}$C)	$\eta_{\mathrm{cBN\text{-}IR}}$ (vol.%)	η_{cBN} (vol.%)	H (GPa)	σ (GPa)	d (nm)	Coating rate (nm min^{-1})
aBN059	100	20	112	0	---	9.4	0.9	570	9.51
aBN062	125	20	116	0	---	12.4	1.1	591	9.85
aBN031	150	20	112	0	0.0	12	0.9	520	8.67
aBN063	150	20	118	0	---	12.7	0.9	579	9.66
aBN060	175	20	137	0	---	13.3	1.0	686	11.44
aBN058	200	30	139	0	---	13.3	0.7	626	10.43
aBN057	250	30	145	0	---	13.7	0.9	626	10.43
aBN056	300	30	153	0	---	16.8	1.7	578	9.64
aBN061	330	30	159	0	---	19.1	2.2	591	9.85
aBN073	360	30	85	0	---	19.2	3.1	501	8.36
aBN004	360	30	150	0	32.3	20.6	---	350	5.83
aBN030	360	30	158	0	34.5	19.4	3.0	449	7.48
aBN055	360	30	164	0	25.4	17.3	2.1	441	7.34
aBN041	360	40	170	0	32.4	20	2.0	518	8.63
aBN067	360	30	178	0	---	20.5	6.4	758	6.30
aBN039	450	30	163	0	---	23.5	4.2	319	5.31
cBN024	450	30	169	0	29.2	22.9	3.9	298	6.62
aBN064	450	30	183	0	---	16.9	3.2	556	9.26
aBN069	550	30	210	0	---	14.2	3.0	334	5.57

Table 6.2 Preparation parameters of the film samples deposited at elevated substrate temperatures for comparison.

Sample	U_{assist} (eV)	I_{assist} (mA)	T_s (°C)	η_{cBN-IR} (vol.%)	η_{cBN} (vol.%)	H (GPa)	σ (GPa)	d (nm)	Coating rate (nm min^{-1})
cBN013	250	30	680	0	---	3.4	1.3	1044	11.6
cBN017	300	30	680	0	---	3.3	1.2	830	9.22
aBN034	360	30	350	0	13.9	2.1	1.9	259	4.32
aBN043	360	40	350	0	18.3	4	2.2	446	7.44
aBN035	360	30	680	11.7	25.7	4	1.2	207	3.45
aBN042	360	40	680	0	21.6	4.4	0.5	411	6.85
aBN044	360	30	800	0	---	3.7	0.4	352	5.87
aBN038	450	30	350	7.5	26.5	12.4	1.8	284	4.73
cBN007	450	30	680	40.1	49.0	23.7	---	183	6.1
cBN003	450	30	680	70.3	79.7	44.3	6.6	510	4.25
aBN046	450	30	800	29.9	---	1.7	0.4	459	7.64
cBN018	550	30	680	49.6	---	28	4.8	274	3.04

6.3 Evidences Showing the Presence of sp^3 BN Nanoclusters in BN Films Deposited on Unheated Substrates

According to the results of various structural characterization experiments, it is showed that sp^3 nanoclusters generally exist in the film samples prepared on unheated substrates under certain ion assist. In this section, we present the results of a representative sample aBN030, which exhibit all the common features of the films with this structure.

As shown in Table 6.1, Sample aBN030 was made at a U_{assist} (eV) of 360 eV on unheated substrates. Due to the ion bombardment, T_s was risen to 158^{o}C. The B-to-N ratio was found to be 0.93 : 1, which was close to the stoichiometric ratio of 1 : 1. The cross-sectional dark-field image of the sample (Fig. 6.2 (a)) shows some general features common to all samples deposited at similar conditions. The image maps the sp^2 grains with the (0002) basal planes aligned along the growth direction. Two layers are clearly seen, which are labelled as Layer *A* and Layer *B*, and are measured to be ≈ 239 and 210 nm thick for this particular sample. Layer *A* grew on the substrate first. The electron diffraction pattern (Fig. 6.2 (b)) shows the features of a sp^2-bonded structure, but the diffraction spots are rather diffused indicating that the arrangement of the (0002) planes is relatively random. Without changing any parameters, a spontaneous transition from Layer *A* to Layer *B* is observed. The dark field image of Layer *B* (Fig. 6.2 (a)) shows a brighter contrast, indicating that there are more sp^2 regions with the (0002) planes aligned in the substrate normal direction. This is consistent with the electron diffraction pattern (Fig. 6.2 (c)) where two clear diffraction spots of the sp^2 planes are seen and aligned in a direction in parallel with the substrate surface.

Fig. 6.3 (a) is a high resolution (HR) TEM image taken from a region in Layer *A*. Some regions as labelled by “t” contain fringes having an average spacing of 0.366 nm. They correspond to the sp^2 (0002) basal planes, while curling of the planes is clearly seen. Some nano-sized regions as denoted by “p” are seen, in which no fringe can be observed and the structure appears to be highly disordered. This is regarded as the first evidence showing the possible existence of sp^3 nanoclusters in the film.

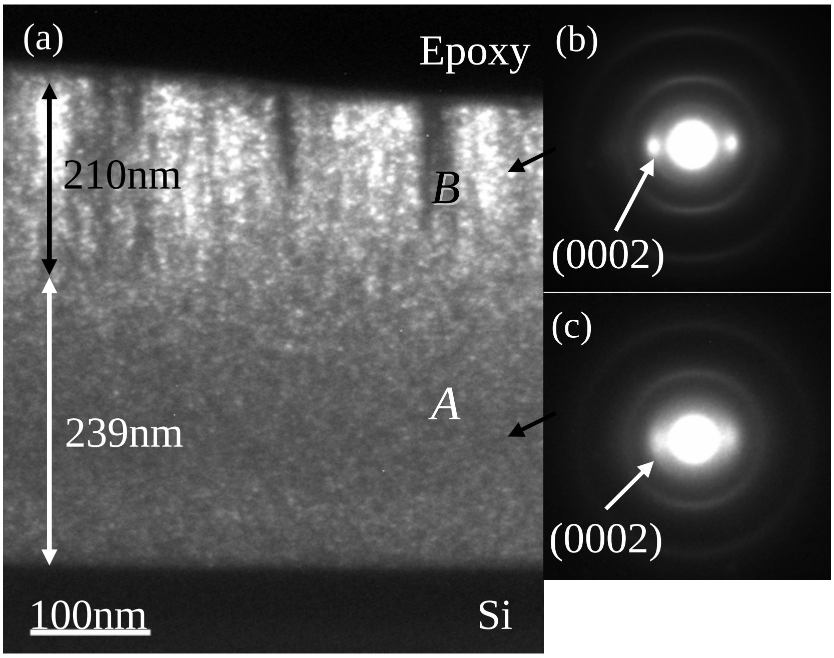

Fig. 6.2 (a) Dark-field image of Sample aBN030 (mapping of the sp^2 grains with (0002) planes aligned along the growth direction). (b) and (c) are the selected area electron diffraction patterns taken from Layer *A* and Layer *B* respectively.

The second evidence supporting the presence of the expected non-crystalline sp^3 nanoclusters is from the results of electron energy loss spectroscopy analysis preformed by using a transmission electron microscope (EELS(TEM)) (Fig. 6.3 (b)). EELS(TEM) is a powerful tool to distinguish the sp^2 structure and sp^3 structure, with a spatial resolution as good as 1 nm. The EELS(TEM) spectra of the p and t regions were taken with the electron beam set at around 1 nm. In these spectra, both the onsets of the B K and N K edges at 188 eV and 401 eV are seen. For the spectrum of region t, a strong π^* peak at ~ 191 eV is seen at around the B K-edge. This peak is associated with the 1s $\rightarrow \pi^*$ transition, and is a signature of the presence of the sp^2-bonded BN structure. On the other hand, for the spectrum taken at the p region, the intensity of the π^* peak decreases greatly. Instead, the peak at 196 eV appears to become stronger. It is identified to be the 1s-σ^* peak (or the σ^* peak) and is a signature of the presence of the sp^3-bonded structure [Takamura, 1999]. Similar conclusion can be obtained by inspecting the near edge structure of the N 1s spectrum. We can therefore conclude that the p region should contain certain volume fraction of sp^3 structure. However, referring to the randomness of the atomic arrangement as seen in the HRTEM picture (Fig. 6.3(a)), we suggest that the sp^3-bonded structure only have very short-range order. This appears to be a new BN structure which has not been reported or even proposed by others. We may name the p regions as “sp^3 nanoclusters”. Typically, a sp^3 nanocluster in this layer is elliptical in shape, with the long and short axes to be around 6 nm and 22 nm respectively, as one can be seen in Fig. 6.3 (a).

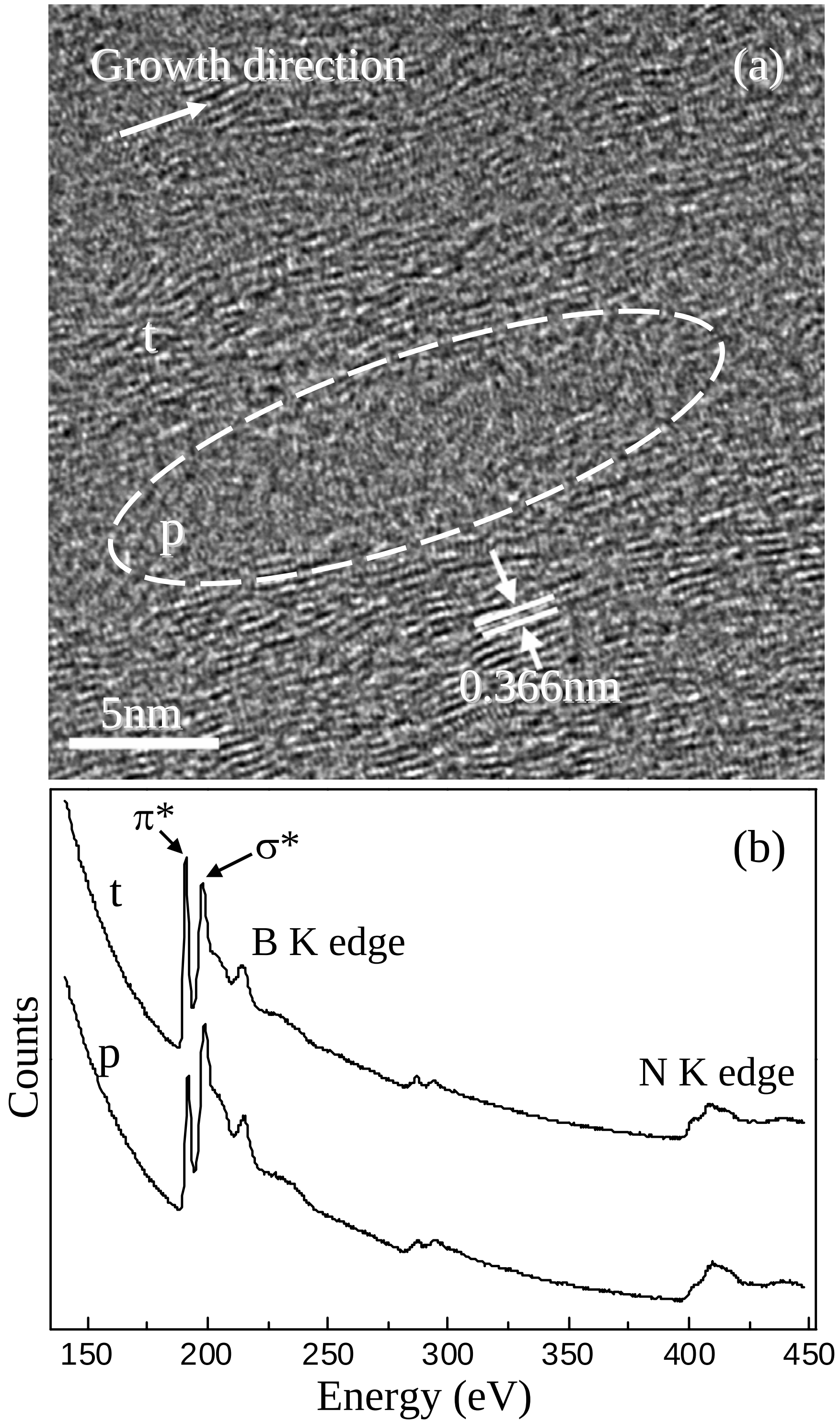

Fig. 6.3 (a) HRTEM picture captured at Layer *A*

(b) TEM-EELS spectra of sp^2-bonded area (t) and highly disordered area (p) in Layer *A*

For Layer *B*, Fig. 6.2 (a) shows that it has a stronger columnar structure. More sp^2-bonded grains are aligned orderly with their (0002) planes in the substrate normal direction. The HRTEM image of Layer *B* (Fig. 6.4) shows that it also has t regions as defined before. This feature is well consistent with the electron diffraction pattern as shown in Fig. 6.2 (c), where the two spots of the (0002) planes are aligned in the direction in parallel with the substrate surface. The third evidence showing the presence of sp^3 nanoclusters comes from the finding of some p regions in Layer *B*. The shape of the p regions in Layer *B* is different from that of Layer *A*. We recall that a p region in Layer *A* is approximately in the shape of an ellipse, but that in Layer *B* is in the shape of a long strip. The strip has a typical width of around 8 nm. The EELS(TEM) spectrum of such a p region is similar to that of a p region in Layer *A* as shown in Fig. 6.3 (b).

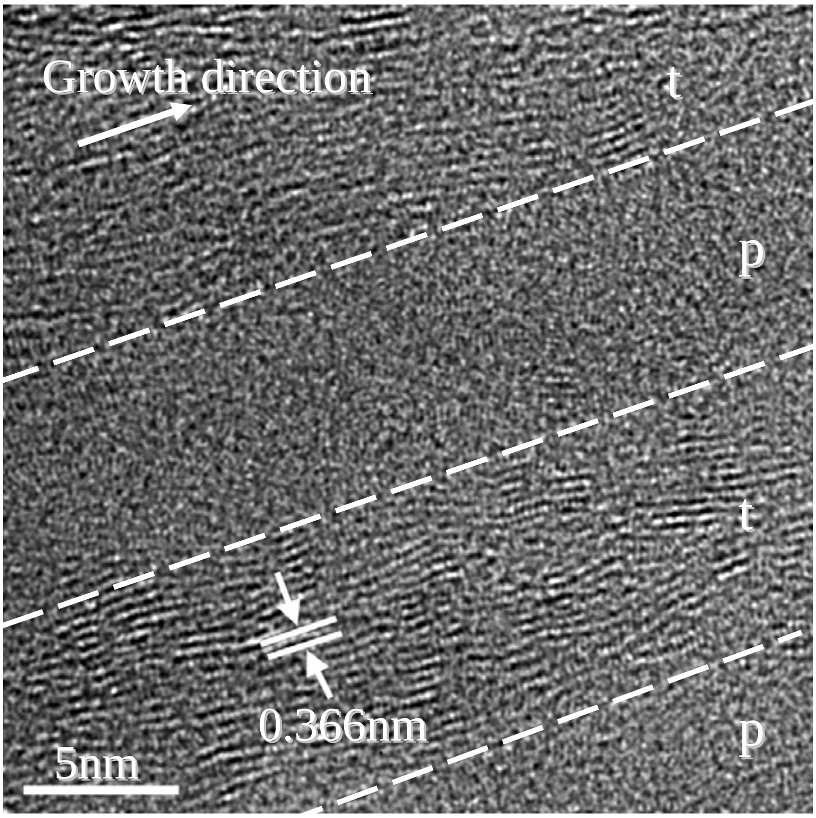

Fig. 6.4 HRTEM picture showing the distribution of sp^2-bonded and highly disordered areas in layer *B*

The fourth evidence showing the presence of the sp^3 nanoclusters in the films is from the measurements of the mechanical properties of the BN films. Nanonindentation tests were performed to measure the film hardness and elastic modulus. The hardness and elastic modulus of a pure sp^2-bonded BN film are typically around 2 GPa and 90 GPa [Hugh, 1996]. However, the hardness and elastic modulus of Sample aBN030 were found to be as high as 19.4 GPa and 203.4 GPa respectively, which are both much higher. It is quite sure that the observed mechanical properties of the BN films deposited on unheated substrates should come from the presence of these sp^3 nanoclusters.

The fifth evidence showing the presence of sp^3 nanoclusters in these samples is from the EELS(XPS) analysis. Employing the EELS(XPS) method as described in Section 2.2.5, the volume fraction of the sp^3 content in these samples can be quantitatively estimated. In this method, N 1s XPS spectrum is recorded first. The curve is best fitted by a linear combination of the three reference EELS(XPS) spectra of the standard specimens, i.e. crystalline cBN, crystalline hBN and aBN. The sp^3 content is estimated from the fitting parameters according to Eq. (2.3). The volume fraction of the sp^3 content η_{cBN} in Sample aBN030 was found to be 35 vol.%, though no cBN grains can be seen in the transmission electron micrographs.

It leaves a question that why the sp^3 contents of the films deposited on unheated substrates derived from the EELS(XPS) method (η_{cBN}) can be as larger as a few tens of vol.%, but those obtained from the infrared absorption ($\eta_{\mathrm{cBN\text{-}IR}}$) data are so low (practically equal to zero, as shown in Table 6.2). We recall that the η_{cBN} value is obtained from fitting the N1s EELS(XPS) spectrum of a sample by referring to the standard spectra of the three reference samples as shown in Fig. 6.5. The IR absorption spectra of all samples deposited on unheated substrates do not show any signature of the sp^3 structure as shown in Fig. 6.6. To give a possible answer to this question, we compare the data of the film samples deposited at different conditions. We first listed their preparation conditions and sp^3 contents derived by using the two methods ($\eta_{\mathrm{cBN\text{-}IR}}$ and η_{cBN}) in Table 6.3. It is further assumed that the hardness value H would increase with the true sp^3 content in a film, and so would be a good indicator to reflect qualitatively the sp^3 content in the sample. With this assumption, the data of $\eta_{\mathrm{cBN\text{-}IR}}$ (solid symbol) and η_{cBN} (hollow symbol) are plotted against the hardness H, as shown in Fig. 6.7.

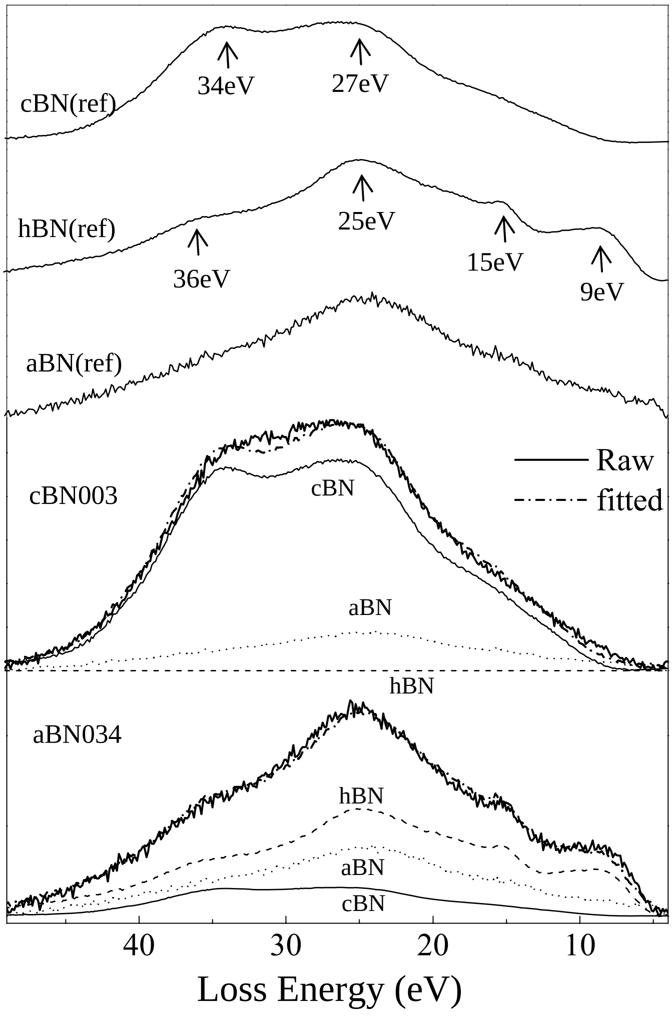

Fig. 6.5 EELS(XPS) spectra of cBN, hBN, aBN references, cBN003 and aBN034.

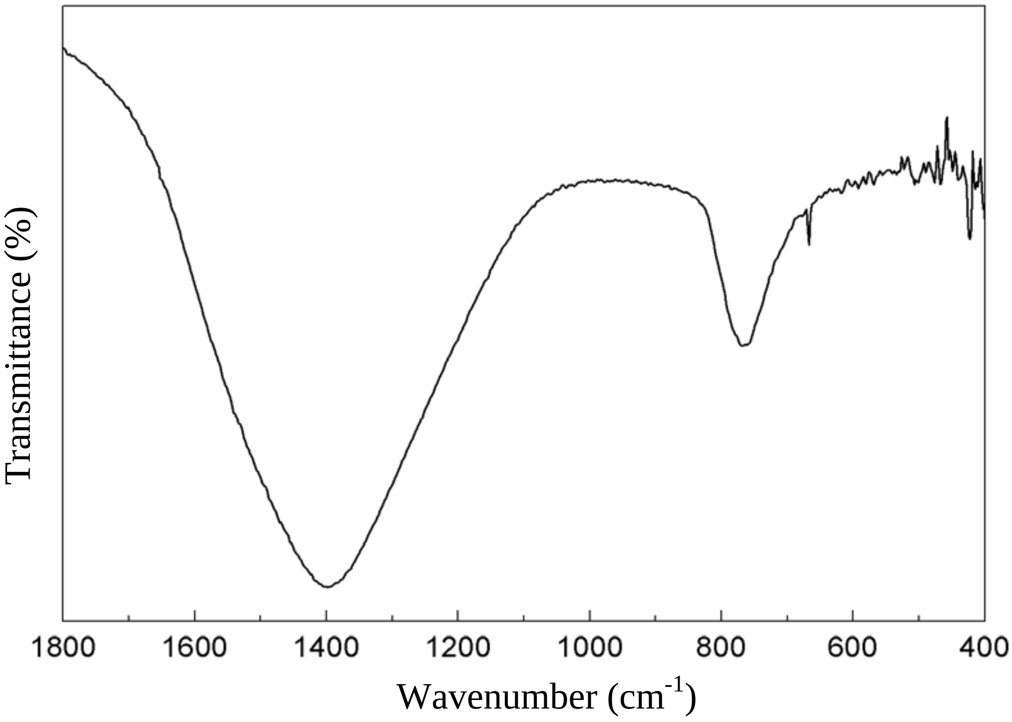

Fig. 6.6 IR absorption spectrum of Sample aBN030

Table 6.3 Deposition conditions, thickness *d*, and estimated contents of different structural phases derived from IR and EELS(XPS) methods.

Sample	U_{assist} (eV)	T_S (^{o}C)	*d* (nm)	B-to-N	$\eta_{\text{cBN}}/\eta_{\text{hBN}}/\eta_{\text{aBN}}$ (%)	$\eta_{\text{cBN-IR}}$ (%)	*H* (GPa)
aBN031	150	112 (unheated)	320	1.2	0 / 0 / 100	0	12.0
aBN030	360	158 (unheated)	449	0.9	35 / 30 / 35	0	19.4
aBN004	360	150 (unheated)	350	1.0	32 / 42 / 26	0	20.6
aBN041	360	170 (unheated)	518	0.9	32 / 11 / 57	0	16.8
aBN043	360	350	446	1.0	22 / 35 / 43	0	4.0
aBN034	360	350	259	1.1	14 / 54 / 32	0	2.1
aBN042	360	680	411	0.9	18 / 67 / 15	0	4.4
aBN038	450	350	284	1.0	27 / 25 / 48	5	12.4
cBN007	450	680	183	1.1	49 /26 / 25	40	23.7
cBN003 (Top)	450	680	510	1.0	79 / 11 / 10	70	44.3

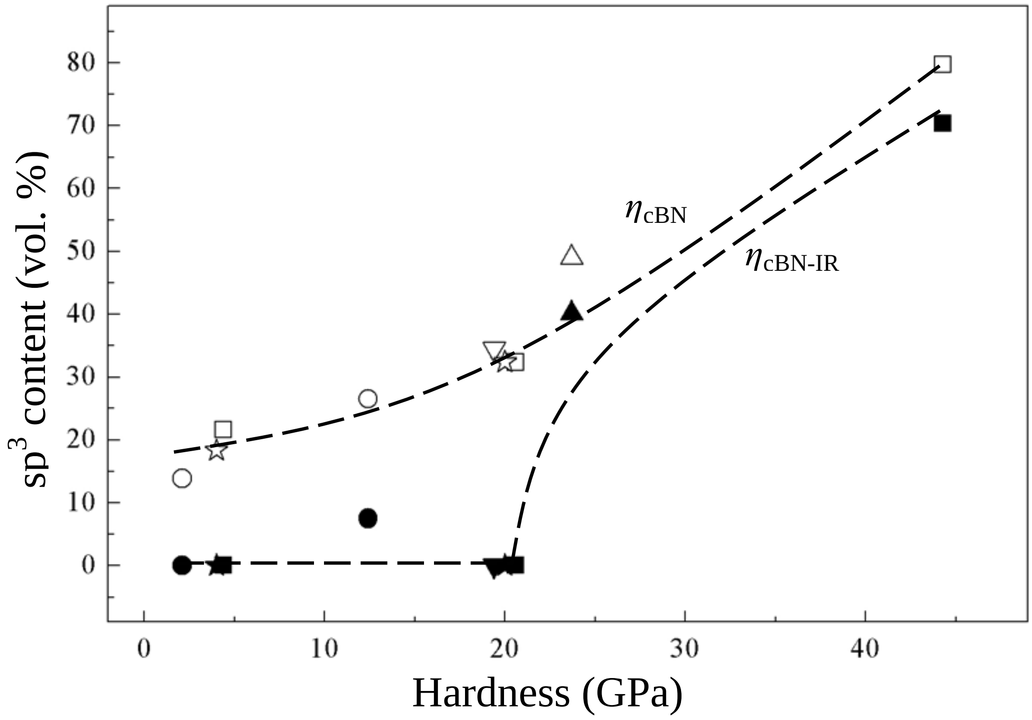

Fig. 6.7. Comparison of the η_{cBN} and η_{cBN-IR} data by using the nanoindentation hardness data as references.

In Fig. 6.7, one sees that when the hardness (H) increases from 2.1 to 19.4 GPa, η_{cBN} increases coherently with H, but $\eta_{\mathrm{cBN\text{-}IR}}$ remains at zero level. It is believed that the hardness value reflects more truly the sp^3 content in the film, but the $\eta_{\mathrm{cBN\text{-}IR}}$ data does not. This is because IR absorption is not sensitive to the presence of sp^3 nanoclusters and so would underestimate the true sp^3 content in a film. This suggestion is supported by the finding of Qian and Shi [Qian, 1998]. They reported that the intensity of the IR absorption peak of zirconia nanoparticles decreased and finally disappeared when the particle size decreased successively. This is known as the size effect of IR absorption measurement as quoted in the literature.

We try to explain this phenomenon from a more fundamental point of view, namely based on Heisenberg uncertainty principle $\Delta x \Delta p \geq \hbar /2$, where Δx is the uncertainty of the position of the detected particles, and Δp is the momentum of the particles in the excitation or emitted beams (i.e. IR photons, X-ray photons or photoelectrons). For the sp^3 nanoclusters, Δx is approximately around 10 nm. Hence, from $\Delta p = h\, \Delta(1/\lambda) \geq \hbar / (2\, \Delta x)$, $\Delta(1/\lambda)$ should exceed 80000 cm^{-1}. Such a broad absorption band is not detectable with a standard IR absorption spectrometer with a detection range of 400 – 4000 cm^{-1}. One expects that no $\eta_{\mathrm{cBN\text{-}IR}}$ can be detected, and IR absorption is not effective in reflecting the true sp^3 content in this case. On the other hand, the EELS(XPS) method does not have this limitation. If the excitation photon energy is U = 1486.6 eV (= $\hbar\, c/\lambda$), then $\Delta U = \hbar\, c\, \Delta(1/\lambda) \sim 1.5$ eV. This energy spread would not affect a normal XPS measurement according to the energy resolution of the machine.

Fig. 6.7 further shows that when H is above 20 GPa, the values of η_{cBN} value and $\eta_{\mathrm{cBN\text{-}IR}}$ value are closer. The data in this region are from the samples deposited at a high substrate temperature T_s = 680°C and a high assist beam energy U_{assist} = 450 eV. In these samples, the cBN grains are relatively larger, as such the IR absorption becomes effective in detecting the sp^3 content. This explains why the EELS(XPS) and IR data are so close.

Finally, it is noted that the $\eta_{\mathrm{cBN\text{-}IR}}$ value measured for a sample is always lower than the η_{cBN} value. This is possibly because some nano-sized sp^3 structure could exist in the film, which contributes to the EELS(XPS) result, but not to the IR result. As such, IR absorption would give an sp^3 content which is constantly lower than that given by an EELS(XPS) analysis.

6.4 Pressure and Temperature Dependence of the Evolution of sp^3 Nanoclusters

Assist beam energy (U_{assist}) and substrate temperature (T_s) are two important parameters affecting the microstructure of a film. The former induces compressive stresses to facilitate the formation of the sp^3 phase, and concurrently causes annihilation of defects to reduce stresses (ion-induced annealing effect). A higher substrate temperature (T_s) can enhance crystallization and internal stress relaxation. These effects coexist and mix together in a deposition process. In this section, we present the results of a systematic study to reveal the influences of the assist beam energy (U_{assist}) and the deposition temperature (T_s) on the formation of the sp^3 nanoclusters. For this purpose, the properties of the samples prepared on unheated substrates and different U_{assist} values from 100 to 550 eV (Table 6.1) show the influences of U_{assist}. Next, the properties of the samples deposited on unheated substrates are compared with those of the samples prepared at high T_s of 350 - 800$^{\mathrm{o}}$C (Table 6.2) in order to reveal the influences of increasing T_s.

Now, we address the influences of the increase in U_{assist} on the microstructures of the samples fabricated on unheated substrates. We start from aBN031, a sample prepared at low U_{assist} = 150 eV (Table 6.1). Its structure has the following features. (i) The cross-sectional TEM image (Fig. 6.8 (a)) shows that there are two layers, labeled by "*A*" and "*B*". Layer *A* is grown directly on the substrate (155 nm), and Layer *B* is on top (165-nm). The transition from Layer *A* to Layer *B* occurred spontaneously during deposition since no parameters were altered in the meantime. (ii) The HRTEM image and electron diffraction pattern of Layer *A* (Fig. 6.8 (b)) show that the layer is highly disordered and sp^{2}-bonded. In fact, this sample is referred to as a reference specimen of the aBN structure in this study. The randomness of the structure is due to use of a low U_{assist} where no strong enough internal stresses are built up to result in more orderly alignment of the basal planes. (iii) The HRTEM image and electron diffraction pattern of Layer *B* (Fig. 6.8 (c)) show that the layer is also sp^{2} bonded, while the basal planes are short and some degree of alignment along the growth direction. For this sample, the sp^{3} content (η_{cBN}) was assumed to be zero. The original HRTEM images of the two layers have been modified with some imaging processes to improve the contrast, and are shown in Fig. 6.9.

The right side of Fig. 6.9 shows the HRTEM images of Sample aBN030 (showed previously in Fig. 6.3 (a) and 6.4), which is deposited at a higher U_{assist} of 360 eV. Compared with Sample aBN031, it also has two layers. However, the alignment of the basal planes is more ordered in the growth direction. Most important, some sp^{3} BN nanoclusters appear proved by the EELS(TEM). The nanoclusters in Layer *A* are elliptical in shape, while those in Layer *B* are in the shape of long strip. This immediate suggests that the effect of increasing U_{assist} are to increase compressive stresses in the layers resulting in better alignment of the basal planes, and to initiate the formation of sp^{3} short-range order which some mechanisms which has not been fully known yet.

Under the ion bombardment with a high U_{assist} value (p. 4-32), sp^{3}-to-sp^{2} transition as well as the annihilation of defects are enhanced, which overwhelm the increase in ion-induced stresses. This causes an overall drop in the internal stresses of the deposits.

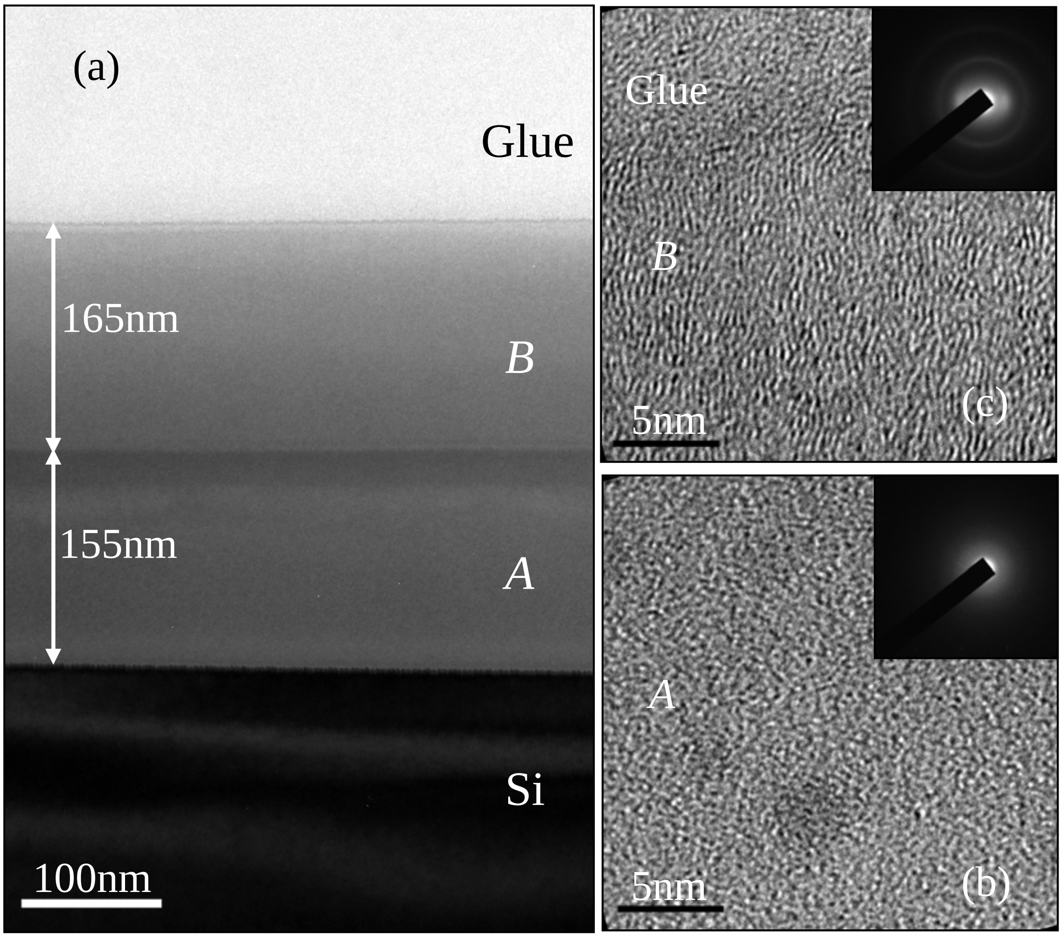

Fig. 6.8 (a) TEM image of Sample aBN031. (b) and (c) HRTEM images and electron diffraction patterns of Layer *A* and Layer *B*.

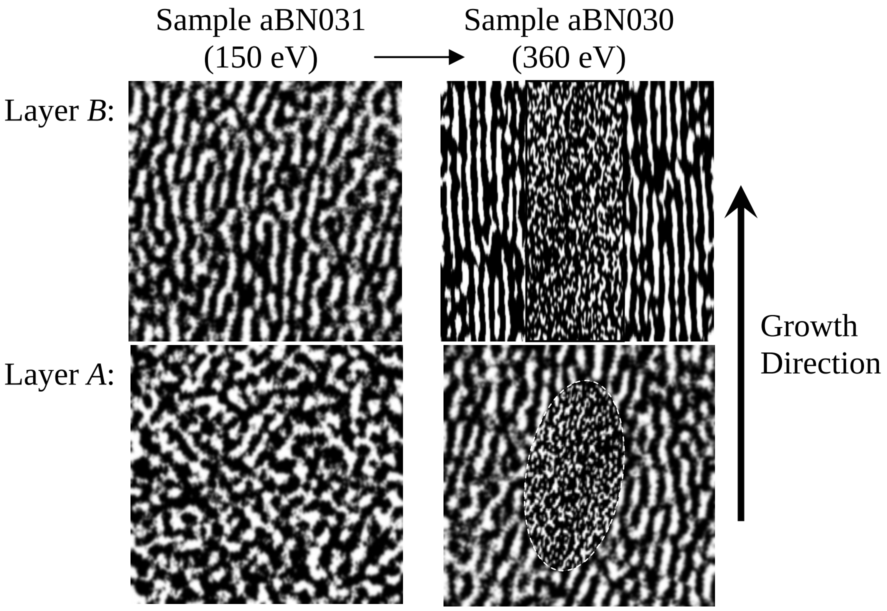

Fig. 6.9 Modified HRTEM images of Layer *A* and Layer *B* of Samples aBN031 and aBN030.

We now address the corresponding behaviour of the mechanical properties. Regarding to the observed bilayer structure, one expects that the measured hardness value may exhibit some indentation depth dependence. Fig. 6.10 shows the indentation depth dependence of the measured hardness of four samples deposited on unheated substrates and with different U_{assist} of 150, 250, 360 and 550 eV. For aBN031, the depth profile of the measured hardness exhibits a dip at about 160 nm, which is approximately at the boundary between Layer *A* and Layer *B*. The dip value of the measured hardness is 8 GPa, and a higher value of 12 GPa near the film surface is measured. With increasing depth, the hardness value approaches 11 GPa, which should be the hardness of the Si substrate. For Sample aBN057 deposited at a higher U_{assist} of 250 eV, there is also a dip in the depth profile of the measured hardness value, but the dip is less prominent. In addition, the hardness values at the dip and the film surface are 10 and 14 GPa, which are all higher than the corresponding values of Sample aBN031 (lower U_{assist} of 150 eV). For Sample aBN030 deposited at U_{assist} of 360 eV, though it still has two layers, but the dip of the hardness profile disappears, while a plateau is seen. Importantly, the measured hardness values at the expected location of the boundary between the two layers and at the top surface of the film are 16 and 20 GPa respectively. Both of them are prominently higher than those of Sample aBN057. This trend confirms that the film hardness would be greatly promoted in coherent with the appearance of the sp^3 nanoclusters as observed. Up to now, the major effect of increasing U_{assist} is to raise the ion-induced compressive stresses, whereas more sp^3 nanoclusters are formed with an increase in the average film hardness. Finally, the depth profile of the hardness of Sample aBN069 deposited at U_{assist} = 550 eV does not show any dip or plateau, and hardness value measured at the film surface is around 14 GPa, lower than that of Sample aBN030. We suggest that at this high U_{assist} level, the ion-annealing effect starts to dominate, which annihilates some ion-induced defects to result in an environment of lower stresses. This is unfavorable to the formation of the sp^3 structure. In addition, according to Hui *et al.* [Hui, 2002], ion bombardment at this energy level can damage the sp^3 phase and result in a structural transition towards the sp^2 phase. As such, one expects that the sp^3 content in Sample aBN069 would be relatively low and the hardness would also drop as a consequence.

Regarding to the complicated depth dependence of the film hardness, it is necessary to specify a definition of the film hardness for the sake of comparison. Thereafter, we define that the average value of the data measured at depths around 10-20% of film thickness from the surface to be the representative hardness of the sample.

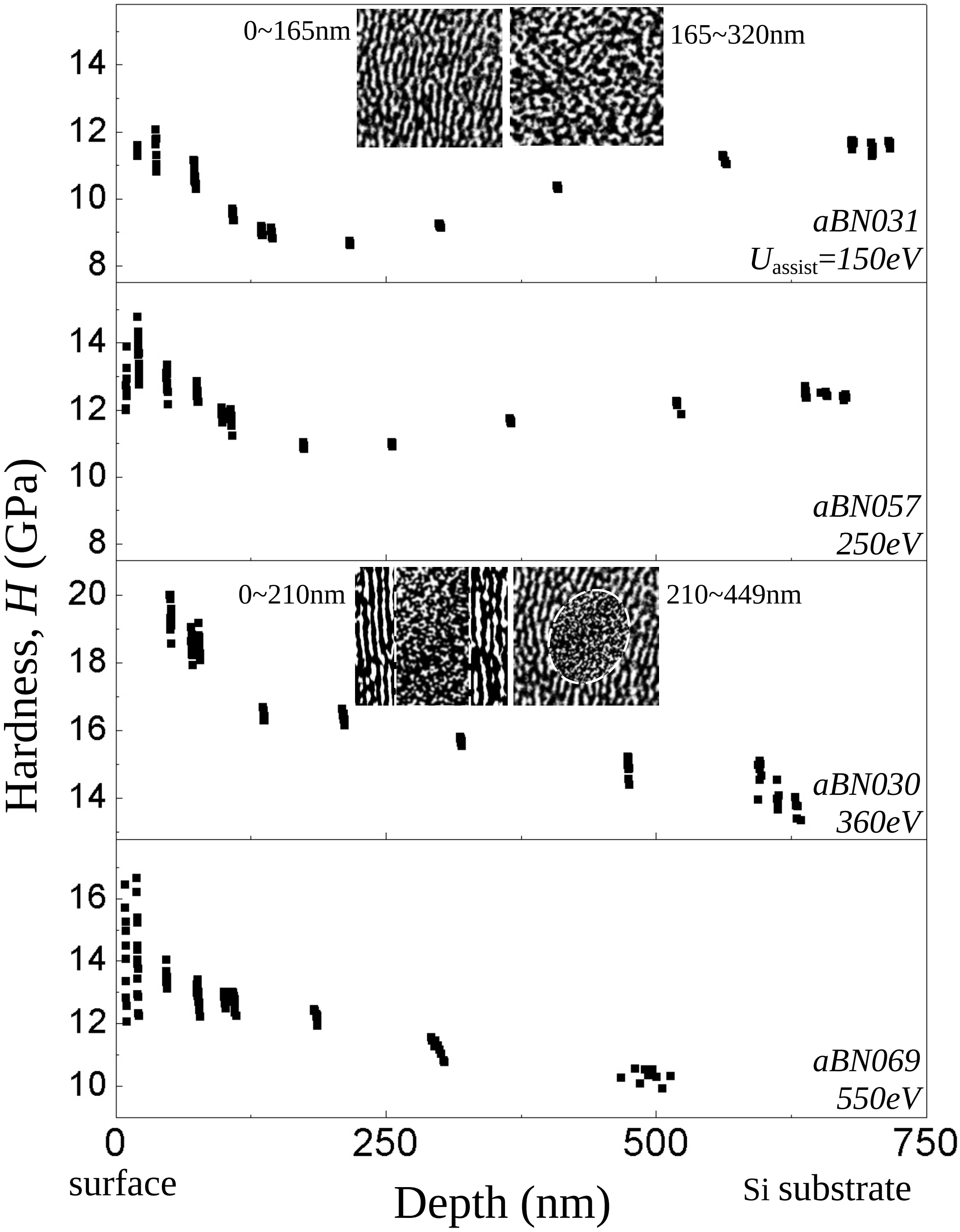

Fig.6.10 The depth profiles of the measured hardness values of the samples deposited at different U_{assist}.

Fig. 6.11 gives the 3-dimensional vision of the sp^3 content measured from the films deposited at different U_{assist} and T_s. Some data points are linked by the solid curves in Fig. 6.11. These curves are re-plotted in Fig. 6.12 to show the U_{assist} dependence of the sp^3 content. The sp^3 contents obtained by EELS(XPS) method (η_{cBN}) are labeled by hollow symbols, and the data obtained by IR absorption ($\eta_{\text{cBN-IR}}$) are labeled by solid symbols. Consider the films deposited on unheated substrates first. At low U_{assist}, both the EELS(XPS) and IR data show that the films do not have any sp^3 content. With increasing U_{assist}, the EELS(XPS) result shows that the sp^3 content in the film rises to reach a maximum of 34.5 vol.% (Sample aBN030). However, the IR result remains to be very small. If we believe that the EELS(XPS) result reflects the true sp^3 content, then the IR result is supposed to lower than the true sp^3 content in the film. Since the TEM image shows that the sp^3 structure exists in the film in the form of nanoclusters, according to the discussion of Section 6.3, it is suggested the sp^3 nanoclusters are too small to be detected by the IR absorption measurement. From this observation, we learn that the use of a higher U_{assist} is necessary for creating sufficiently high stresses to initiate the generation of the sp^3 structure. When U_{assist} increases to 450 eV, the EELS(XPS) data drops to 29.2 vol.%. This reflects that the sp^3 content cannot grow further with increasing U_{assist}, but bombardment by ions of a higher energy would cause damages of the sp^3 phase such that its growth is suppressed. In addition, the EELS(XPS) result is still higher than the IR result, indicating that sp^3 content is still of nanometer size. Consider another group of samples deposited at higher T_s of 680°C. At low U_{assist} of 150 eV, no sp^3 content is observed. With higher U_{assist} of 360 eV, sp^3 content is formed. The EELS(XPS) result is higher than the IR result, where the latter is a non-zero value.

This indicates that some larger cBN grains have formed, but the film still contains considerable sp^3 nanoclusters. Finally, when U_{assist} increases to 450 eV, the results obtained from the two methods rise to a very high level around 70 vol.% and are close from each other, indicating that the sp^3 phase contained in the film is mainly in the form of larger cBN grains, but not in the form of nano-sized clusters.

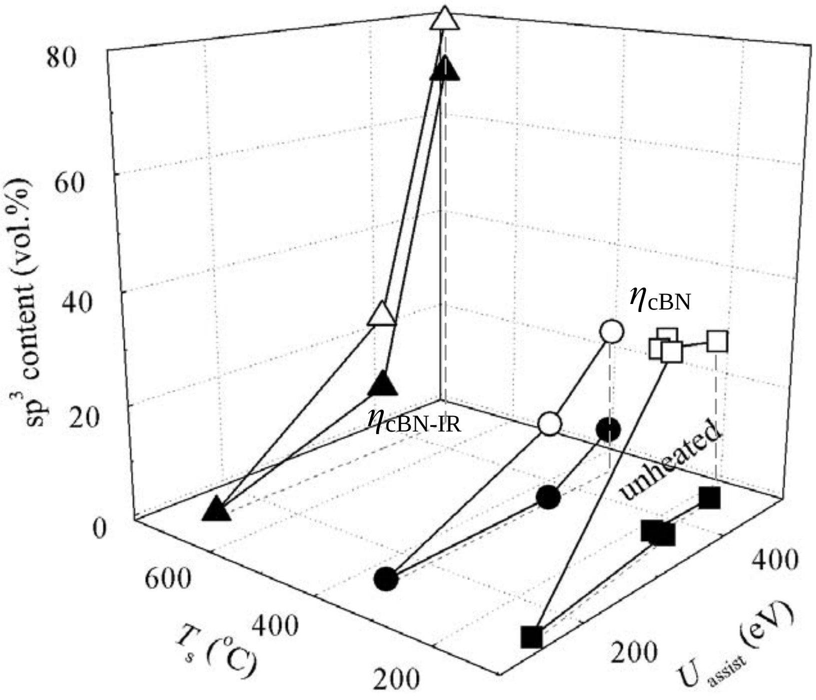

Fig. 6.11 Three-dimensional plot of the sp^3 contents measured by using XPS-EELS (hollow symbols) and IR absorption (solid symbols) against U_{assist} and T_s.

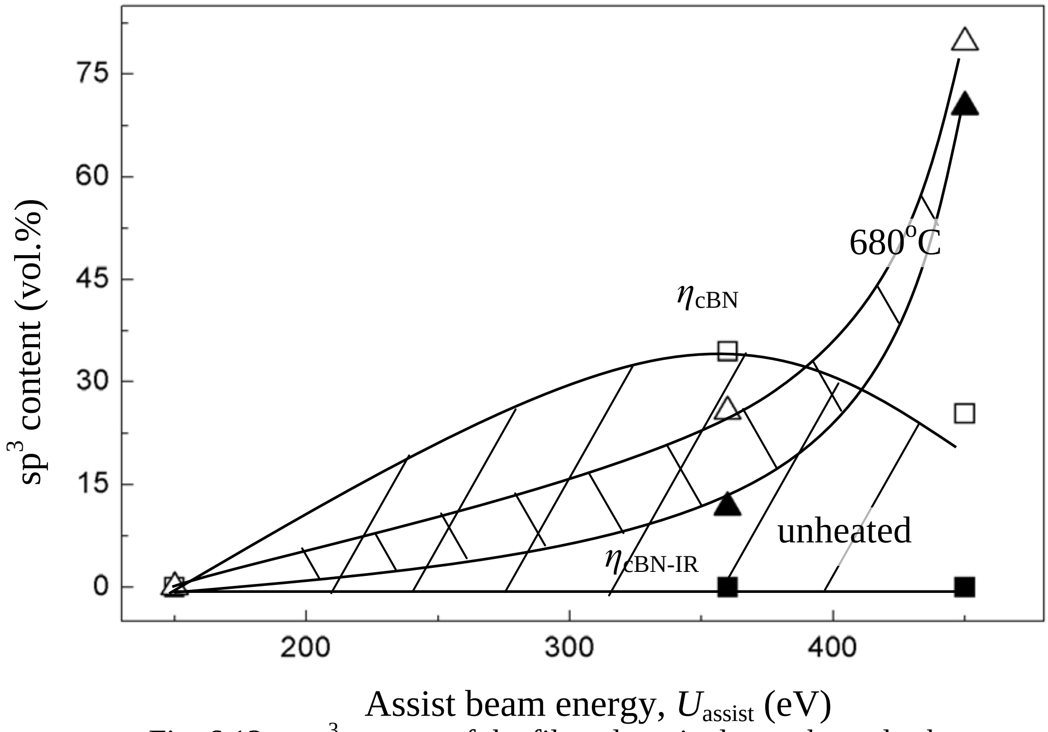

Fig. 6.12 sp^3 content of the films deposited on unheated substrates and 680°C as a function of U_{assist}.

We then inspect the 3-dimensional plot of the film hardness against U_{assist} and T_s (Fig. 6.13). Some data points are linked with solid curves to show the U_{assist} dependence of the film hardness. These curves are re-plotted in Fig. 6.14. For the samples deposited on unheated substrates, the hardness value increases monotonically when U_{assist} increases from 100 to 450 eV and reaches a maximum of 23.5 GPa, in accordance with the increase in the sp^3 content. Further increase of U_{assist} (to 550 eV for example) results in a drop in hardness (to 14.2 GPa). One explanation is that at this high U_{assist} level, ion-beam annealing effect dominates, suppressing ion-induced stress and unfavorable to the formation of the sp^3 structure. Moreover, Hui *et al*. [Hui, 2002] showed that ion bombardment at this energy range would cause severe transformation from the sp^3 phase to the sp^2 phase. Finally, we note that the hardness of the samples deposited at higher T_s of 680^{o}C with U_{assist} from 300 to 360 eV are much softer (hardness = 2.1 – 4 GPa) than those deposited on unheated substrates and the same U_{assist} level, because the higher temperature is unfavorable to the formation of the sp^3 structure according to the P-T phase diagram of BN (Fig. 6.1). Fig. 6.15 and 6.16 show the results of internal stresses in the films, which show some features consistent with the trends of the sp^3 content and film hardness.

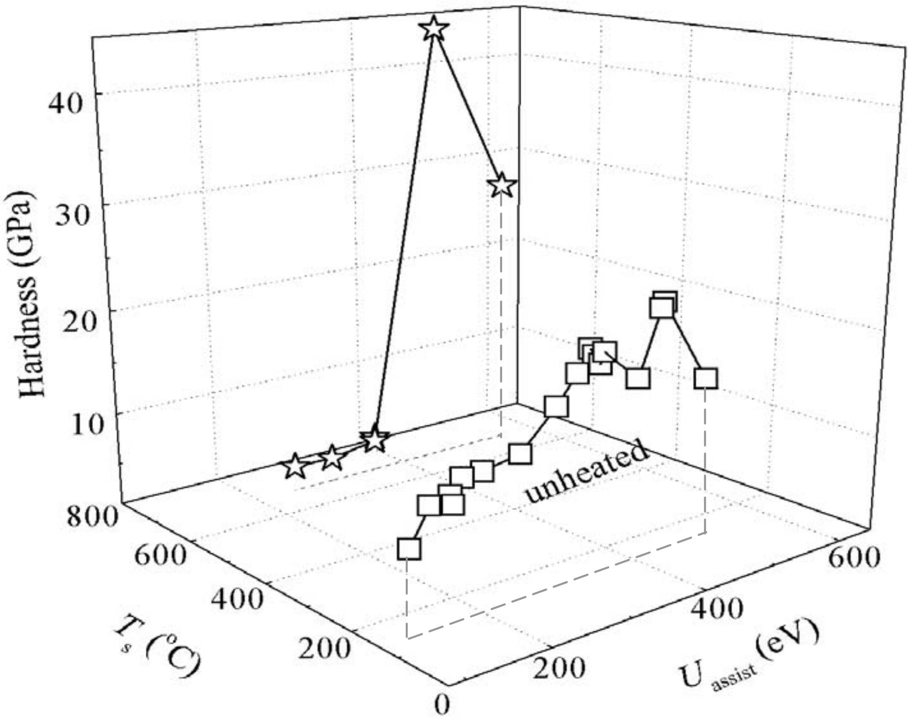

Fig. 6.13 Three-dimensional plot of the film hardness against U_{assist} and T_s.

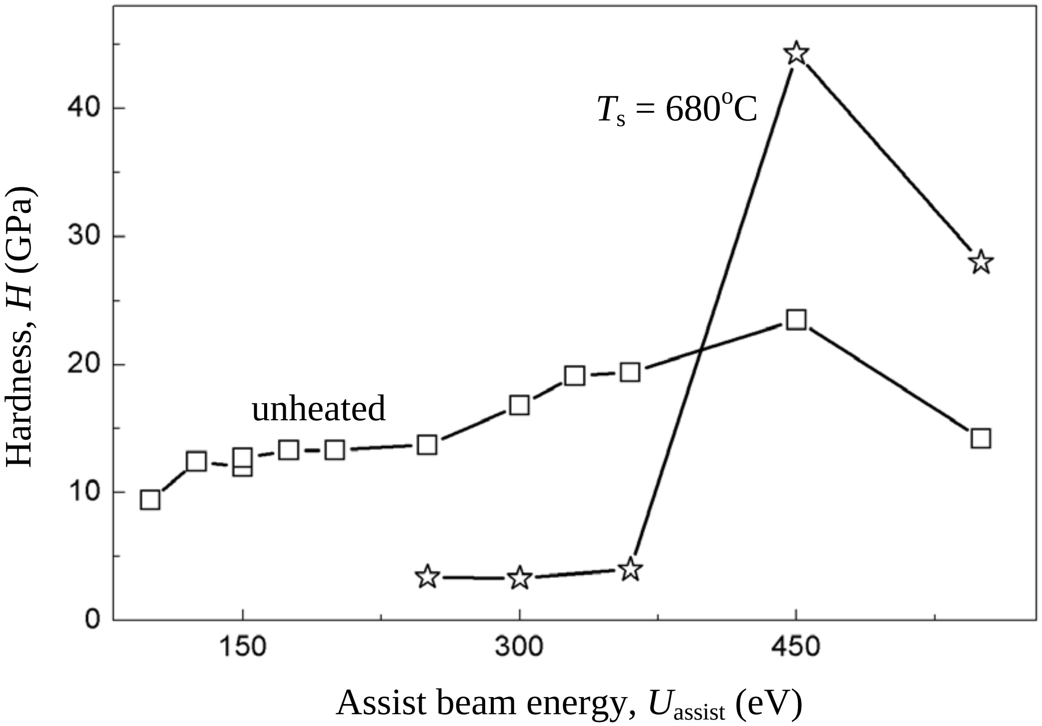

Fig. 6.14 Hardness of the films deposited on unheated substrates and 680°C as a function U_{assist}.

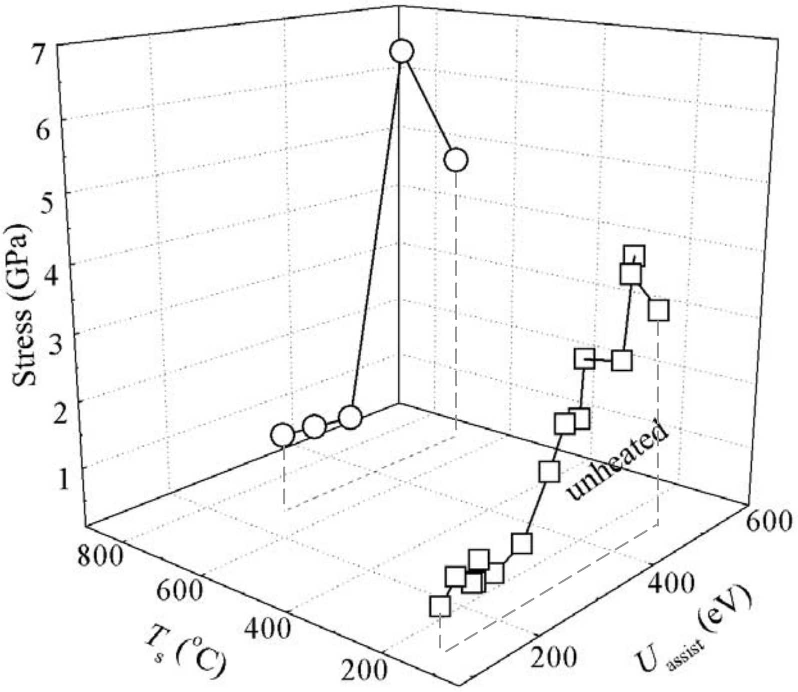

Fig. 6.15 Three-dimensional plot of stress in the films deposited on unheated substrates and 680°C, as a function of U_{assist} and T_s.

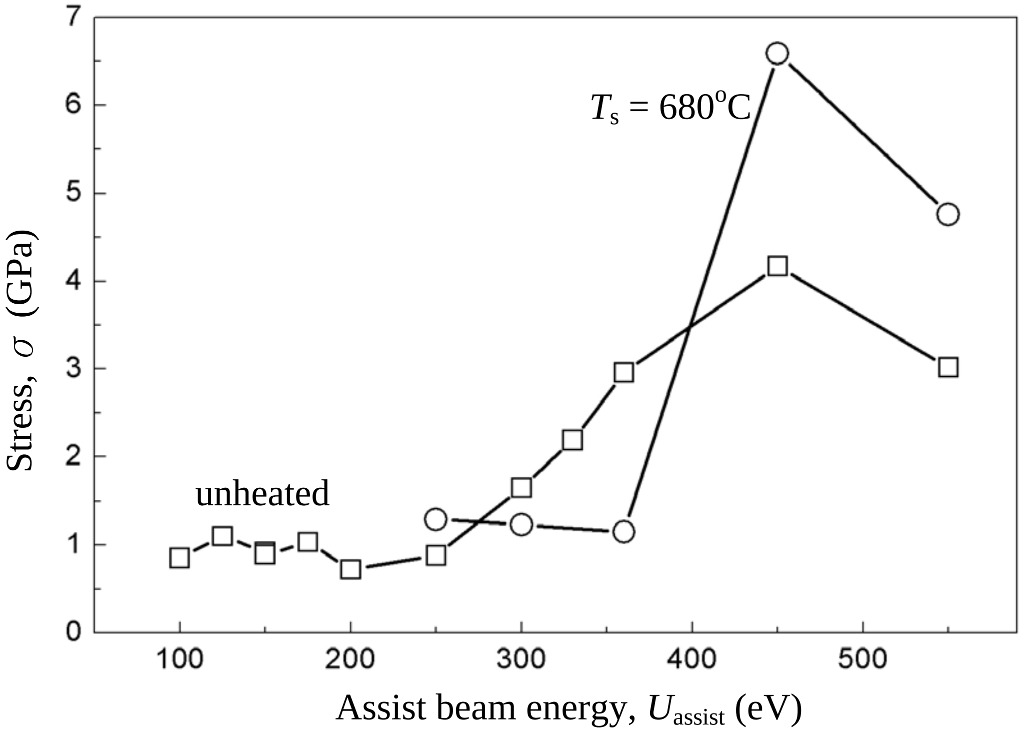

Fig. 6.16 Compressive stress in films deposited on unheated substrates and 680°C as a function of U_{assist}.

We now consider the influence of T_s on the formation of the sp^3 nanoclusters. Fig. 6.17 gives a 3-dimensional vision of the sp^3 contents obtained by using EELS(XPS) (hollow symbols) and IR (solid symbols) as a function of U_{assist} and T_s. Some data points are connected with solid curves, which reflect the T_s dependence of the results and are replotted in Fig. 6.18.

For the samples deposited at a low U_{assist} of 150 eV, no any sp^3 content can detected. When a higher U_{assist} of 360 eV is used, the film deposited on unheated substrate is found to contain around 30 vol.% of sp^3 phase as detected by EELS(XPS), but the FTIR is very near to zero. This indicates that there are conspicuous amount of sp^3 nanoclusters in the films, which are too small to be detected by IR absorption. For higher T_s values, the sp^3 content detected by EELS(XPS) drops slightly. This is consistent with what indicated by the P-T phase diagram of B-N system (Fig.6.1) that a higher temperature is unfavourable to the formation of the cBN phase. Consider the other group of samples deposited at U_{assist} = 450 eV, the sample deposited on unheated substrate still exhibits a sp^3 content around 30 vol.% and the IR result is close to zero because the clusters are small. With increasing T_s, a small drop in the sp^3 content detected by EELS(XPS) is merely seen. For a T_s as high as 680^{o}C, the values of the sp^3 content detected by the two methods get closer, and rise to a level of around 70 GPa. This suggests that nucleation and growth of cBN grains have occurred so as to produce larger cBN grains in the sample.

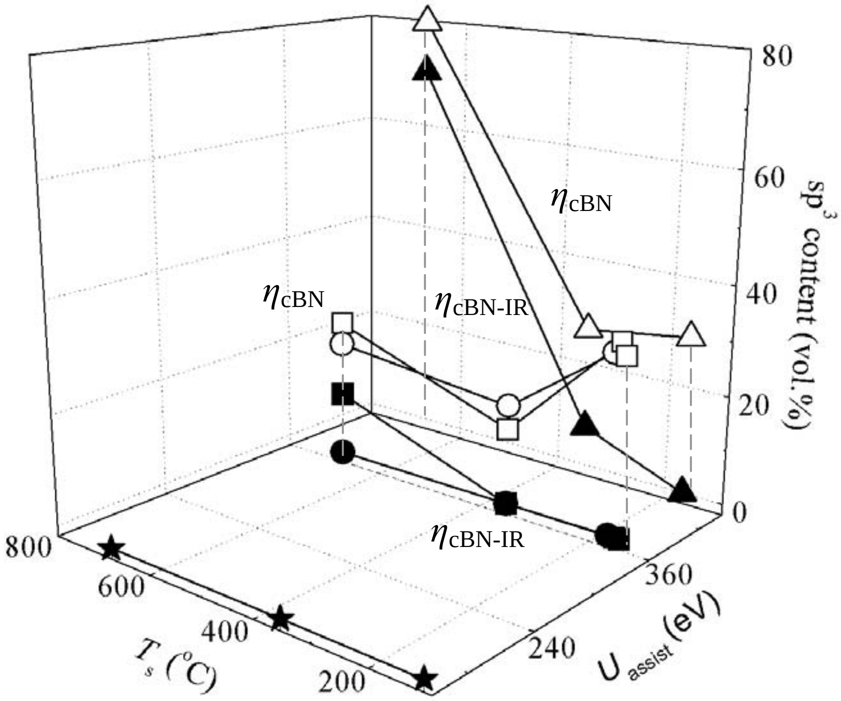

Fig. 6.17 Three-dimensional plot of the sp^3 contents measured by using EELS(XPS) (hollow symbols) and IR absorption (solid symbols) against U_{assist} and T_s.

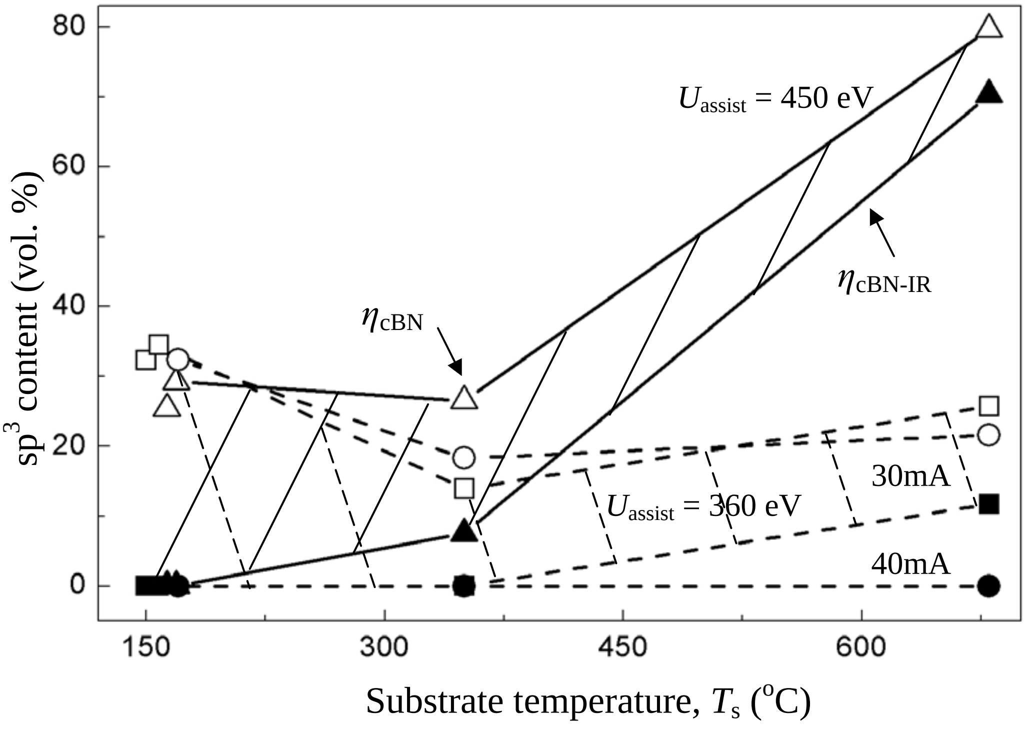

Fig. 6.18 sp^3 contents of films deposited at U_{assist} as a function of T_s.

Fig. 6.19 gives a 3-dimensional vision of the hardness as a function of U_{assist} and T_{s}. Two solid curves are produced to show the T_{s} dependence of hardness of two series of samples deposited at U_{assist} = 360 and 450 eV respectively. Consider the group of the films deposited at U_{assist} = 360 eV first. With increasing T_{s}, the film hardness drops from 20 GPa for the film deposited on unheated substrate to about 3 GPa for the films deposited at T_{s} exceeding 300$^{\mathrm{o}}$C. This suggests that at this low U_{assist} level, sp^3 nanoclusters are formed at low deposition temperature, and when at higher T_{s}, the sp^3 nanoclusters would not form. However, if a higher U_{assist} of 450 eV is used, massive nucleation and the growth of cBN grains occur at higher T_{s} such as 680$^{\mathrm{o}}$C. Fig. 6.21 show the U_{assist} and T_{s} dependence of the stress data in a three-dimensional plot. Some data are linked by solid curves which to show the T_{s} dependence of the stress, which are replotted in Fig. 6.22. All the trends shown in these two figures are consistent with the results of the sp^3 content and film hardness (Fig. 6.17 - 20).

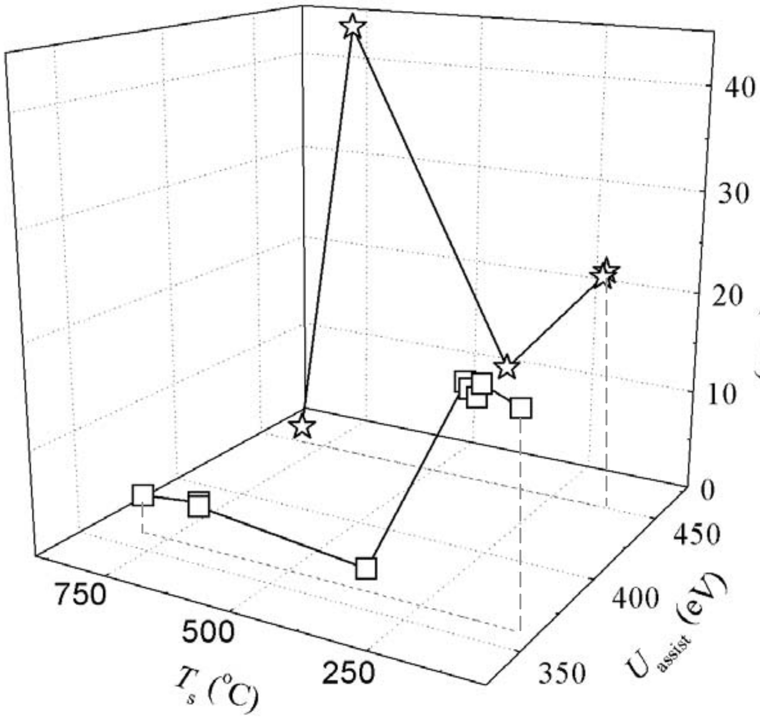

Fig. 6.19 Three-dimensional plot of hardness against U_{assist} and T_s.

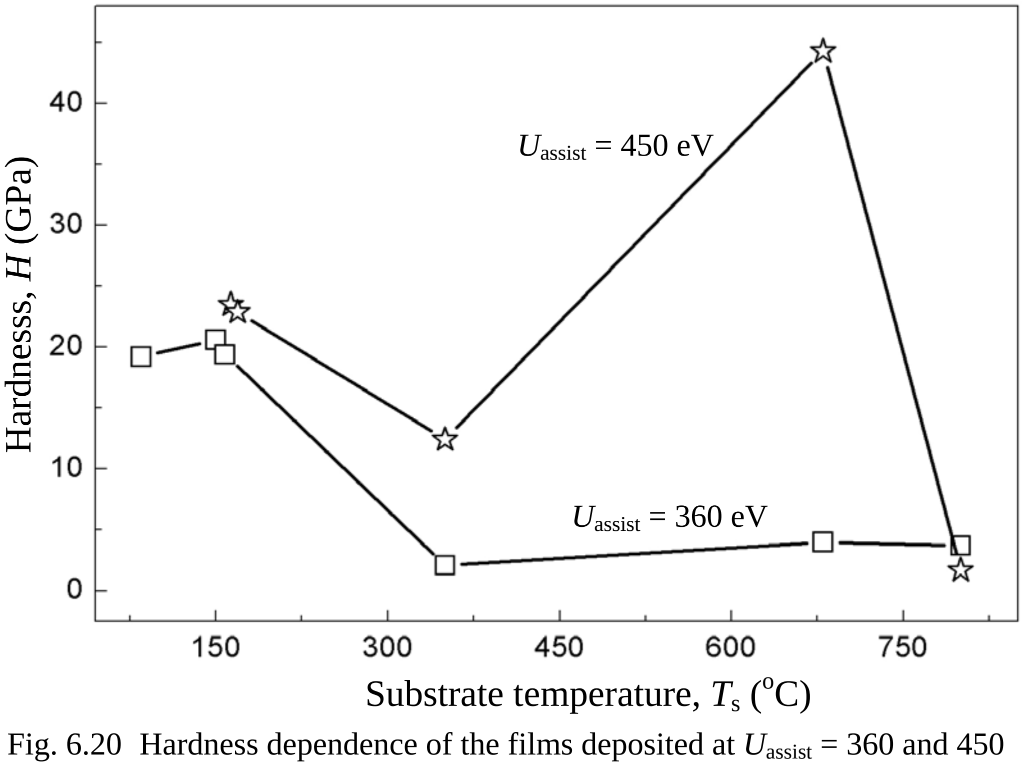

Fig. 6.20 Hardness dependence of the films deposited at U_{assist} = 360 and 450 eV as a function of T_s

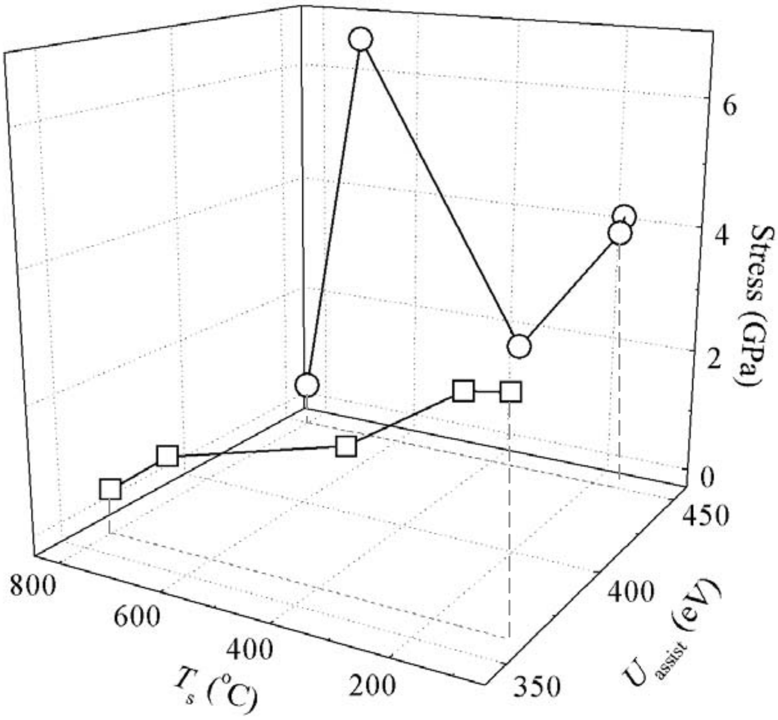

Fig. 6.21 Three-dimensional plot of stress against U_{assist} and T_s.

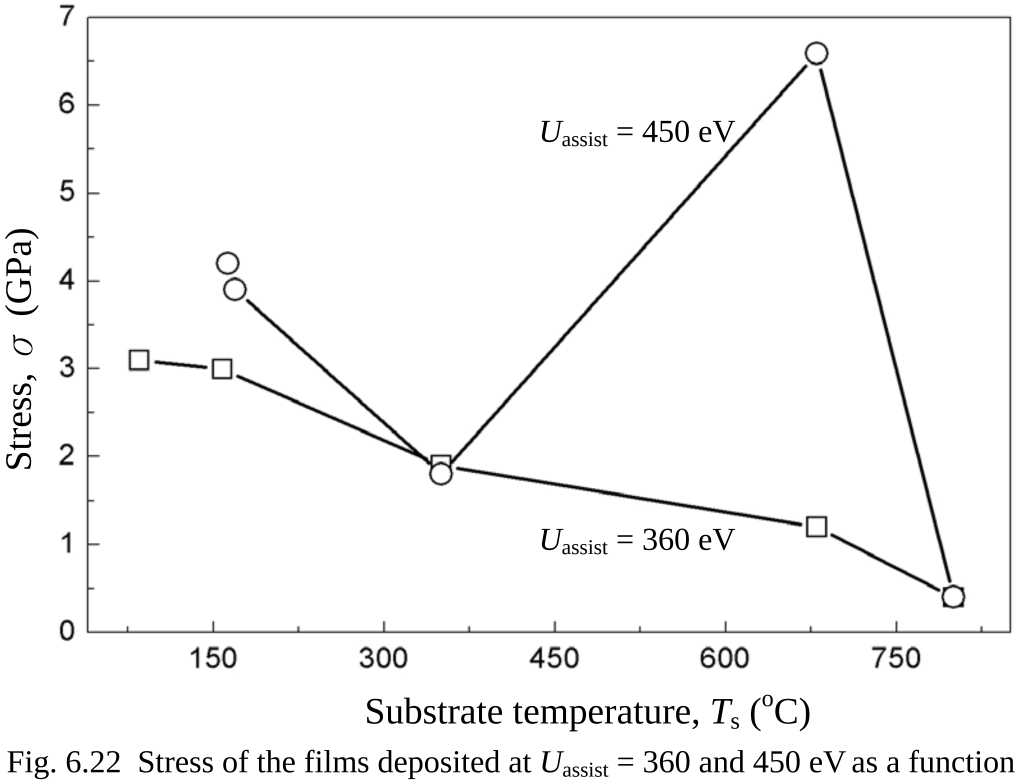

Fig. 6.22 Stress of the films deposited at U_{assist} = 360 and 450 eV as a function of T_s.

Finally, we summarize the most important conclusions obtained from this part of work as follows.

(i) With the use of low $U_{\mathrm{assist},}$ only sp^2 structure is obtained, not matter what value of T_{s} is used.

(ii) On unheated substrates, when U_{assist} is increased to pass some threshold (below or around 360 eV), sp^3 nanoclusters can be formed which make the film to have a high hardness. This is a new BN phase not reported in the past, and may have potential applications. It is also of interest for the study the formation mechanisms of the sp^3 structure. The film produced is actually a composite with sp^3 nanoclusters embedded in a sp^2 BN matrix.

(iii) With U_{assist} ~ 360-450 eV, moderate increase in T_{s} suppresses the formation of sp^3 nanoclusters, in accordance with what predicted from the P-T phase diagram of the B-N system that higher temperature environment is unfavorable to the formation of the cubic phase.

(iv) With U_{assist} ~ 360-450 eV, increase in T_{s} (e.g. to 680$^{\mathrm{o}}$C) would trigger another mode of the growth of sp^3 structure, namely the nucleation and growth of cBN grains, producing a polycrystalline cBN-rich structure.

6.5 Annealing Effects of the BN Films Deposited on Unheated Substrates

The sp^3 nanoclusters observed in this chapter is a new phase, which possesses the following advantages. It contains a high sp^3 content (at least 34.5 vol. %); the internal stress level (3 GPa) is lower than a cBN-rich film of similar thickness; the high hardness is relative high (20-24 GPa); and it can be formed on unheated substrates. These properties suggest that the film material would have potential in applications. One possibility is to use the coating on a cutting tool, as what originally proposed for cBN-rich films but blocked by the peeling off problem. It is then necessary to ask whether the film can remain stable at elevated temperatures as usually required for a coating on a cutting tool. We therefore performed post-annealing tests on the samples to see how their hardness and stresses are changed with increasing annealing temperature.

To select samples for the post-annealing experiment, we refer to the Figs. 6.23 and 24 showing the hardness and stress of the samples deposited on unheated substrates (hollow symbols). When U_{assist} exceeds 250 eV, the two quantities start to rise, indicating the on-set of the formation of the sp^3 nanoclusters, and drop from the maxima when $U_{\text{assist}} > 450$ eV. Based on this primary inspection, we decided to select four samples deposited on unheated substrates with U_{assist} from 360 – 550 eV for the post-annealing experiments They are supposed to contain considerable amount of sp^3 nanoclusters.

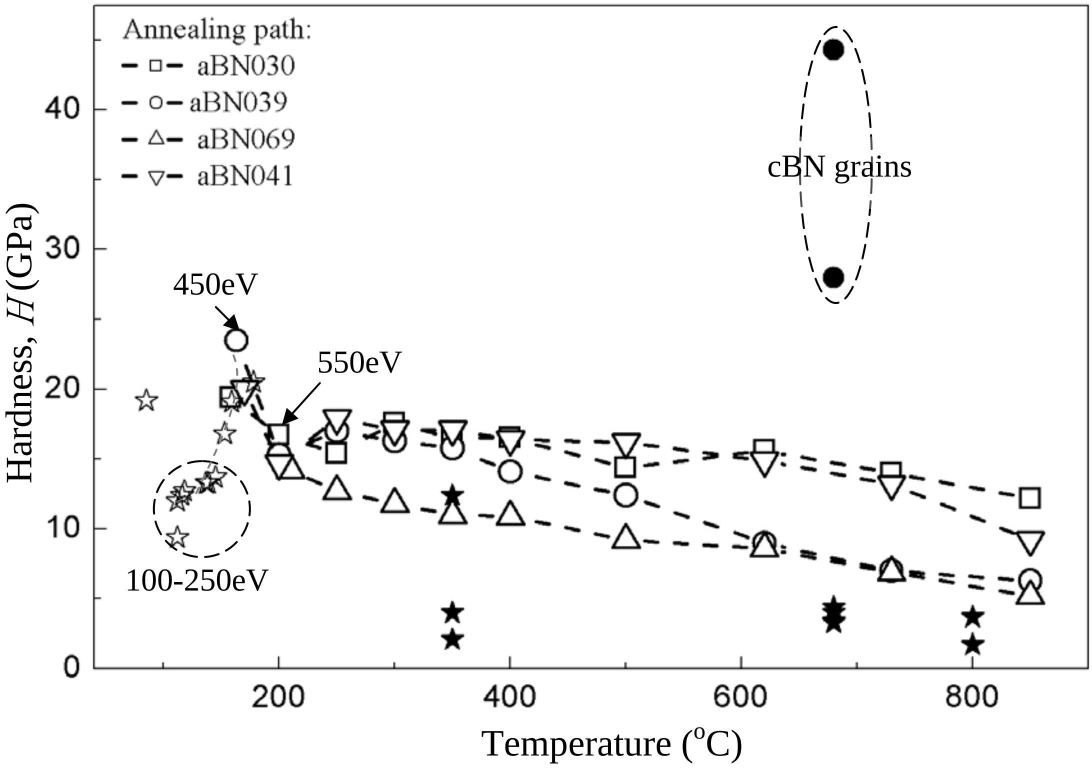

Fig. 6.23 Hardness of four films supposed to contain sp^3 BN nanoclusters as a function of annealing of temperature.

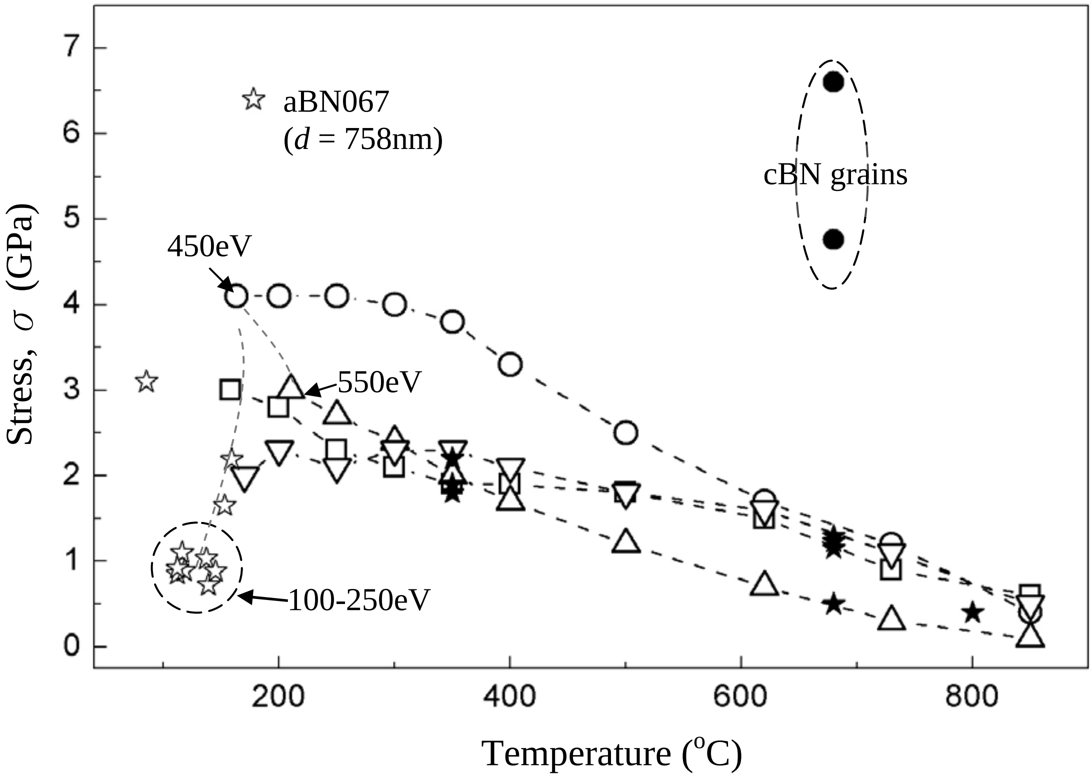

Fig. 6.24 Stress of four films supposed to contain sp^3 BN nanoclusters as a function of annealing of temperature.

The fabrication conditions of the four samples selected for the study, i.e. aBN030, aBN039, aBN069 and aBN041, are listed in more detail in Table 6.4. To conduct the test, a sample was mounted to the substrate holder used for depositing the films. Gas admixture of 20.0 sccm of N_2 and 10.0 Ar gases was admitted into the system. Annealing was conducted in successive steps at 200, 250, 300, 350, 400, 500, 620, 730 and 850^{o}C, each lasted for 1 hour. Results of the sp^3 content, hardness and stresses etc. measured after each annealing step are listed in Table 6.4.

The annealing effects are expressed in terms of the annealing temperature dependence on the hardness and compressive stresses of the films, as shown in Fig. 6.23 and 24. These two quantities were investigated because they were closely related to the content of the sp^3 phase. As shown in Fig. 6.23, the hardness of all samples decreases gradually with the increasing annealing temperature. As summarized in Table 6.4, the hardness drops from 14.2 - 23.5 GPa before annealing to 5.2 - 12.2 GPa after annealing at 850^{o}C. The compressive stress also drops from a level of 2 – 4.1 GPa to 0.1 – 0.6 GPa. These results illustrate that at least part of the sp^3 nanoclusters are not thermally stable, but would be transformed into the sp^2 phase after being heated. Therefore, the nanoclusters would be more or less metastable. The EELS(XPS) results (η_{cBN}) give further support to this conjecture. As seen in Table 6.4, the sp^3 content η_{cBN} drops from 25.4 – 34.5 vol.% to 17.3 – 20 vol.% after annealing at 850^{o}C.

In Fig. 6.23 and 24, we also show the data of the films deposited at high T_s and low U_{assist} which are known to be sp^2-bonded (denoted by "★"); and those deposited at high T_s and U_{assist} which are known to be polycrystalline cBN films (denoted by "●"). Although the stress value of the samples is relaxed to approach the as-deposited sp^2 films, but the hardness of the film still remains high. Especially, the two samples deposited at U_{assist} = 360 eV have higher hardness after annealing, exhibiting a more superior thermal stability. This result reflects that the sp^3 nanoclusters are not completely transferable to sp^2 structure, while on the other hand the films containing sp^3 nanoclusters may have sufficiently good thermal stability for certain applications.

Table 6.4 Results of aBN030, aBN039, aBN069 and aBN041 after annealing at different temperatures.

Sample	U_{assist} (eV)	I_{assist} (eV)	T_s (°C)	$\eta_{\text{cBN-IR}}$ (vol. %)	η_{cBN} (vol. %)	H (GPa)	σ (GPa)	d (nm)	Coating rate (nm*min^{-1})
aBN030	360	30	26 - 158	0.0	34.5	19.4	3.0	321	5.35
	Annealed at 200°C, 1hr			0.0		16.7	2.8		
	Annealed at 250°C, 1hr			0.0		15.4	2.3		
	Annealed at 300°C, 1hr			0.0		17.6	2.1		
	Annealed at 350°C, 1hr			0.0	↓	16.5	1.9		
	Annealed at 400°C, 1hr			0.0		16.5	1.9		
	Annealed at 500°C, 1hr			0.0		14.4	1.8		
	Annealed at 620°C, 1hr			0.0		15.6	1.5		
	Annealed at 730°C, 1hr			0.0	20.0	14.0	0.9		
	Annealed at 850°C, 1hr			0.0		12.2	0.6		
aBN039	450	30	30 - 163	0.0	25.4	23.5	4.1	319	5.31
	Annealed at 200°C, 1hr			0.0		15.3	4.1		
	Annealed at 250°C, 1hr			0.0		17.0	4.1		
	Annealed at 300°C, 1hr			0.0		16.3	4.0		
	Annealed at 350°C, 1hr			0.0	↓	15.8	3.8		
	Annealed at 400°C, 1hr			0.0		14.1	3.3		
	Annealed at 500°C, 1hr			0.0		12.4	2.5		
	Annealed at 620°C, 1hr			0.0		9.0	1.7		
	Annealed at 730°C, 1hr			0.0	17.3	7.0	1.2		
	Annealed at 850°C, 1hr			0.0		6.3	0.4		
aBN069	550	30	25 - 210	0.0	NIL	14.2	3.0	334	5.57
	Annealed at 250°C, 1hr			0.0		12.7	2.7		
	Annealed at 300°C, 1hr			0.0		11.8	2.4		
	Annealed at 350°C, 1hr			0.0		11.0	2.0		
	Annealed at 400°C, 1hr			0.0		10.9	1.7		
	Annealed at 500°C, 1hr			0.0		9.2	1.2		
	Annealed at 620°C, 1hr			0.0		8.6	0.7		
	Annealed at 730°C, 1hr			0.0		6.9	0.3		
	Annealed at 850°C, 1hr			0.0		5.2	0.1		

Sample	U_{assist} (eV)	I_{assist} (eV)	T_s (^{o}C)	$\eta_{cBN\text{-}IR}$ (vol. %)	η_{cBN} (vol. %)	H (GPa)	σ (GPa)	d (nm)	Coating rate (nm*min^{-1})
aBN041	360	40	23 - 170	0.0	32.4	20.0	2.0	518	8.63
	Annealed at 200^{o}C, 1hr			0.0		14.7	2.3		
	Annealed at 250^{o}C, 1hr			0.0		17.9	2.1		
	Annealed at 300^{o}C, 1hr			0.0		17.1	2.3		
	Annealed at 350^{o}C, 1hr			0.0	↓	17.1	2.3		
	Annealed at 400^{o}C, 1hr			0.0		16.4	2.1		
	Annealed at 500^{o}C, 1hr			0.0		16.2	1.8		
	Annealed at 620^{o}C, 1hr			0.0		14.9	1.6		
	Annealed at 730^{o}C, 1hr			0.0	20.0	13.2	1.1		
	Annealed at 850^{o}C, 1hr			0.0		9.2	0.5		

6.6 Discussions on the Growth Mechanisms of sp^3 Nanoclusters

The sp^3 nanostructure observed in this study is a new BN phase which has not been reported in literature. Therefore, its formation mechanism is of great interest. Knowledge on how it is formed may provide important clues towards more fundamental understanding on the growth mechanisms of polycrystalline cBN structure, which up to date have not been completely understood. In this section, we investigate the possible formation mechanisms of the sp^3 structure by using two theories, i.e. thermal spike theory and stress theory, which are two of the most important existing theories in this field of study. We investigated the applicability of the methods by seeing that whether the features of the nanoclusters observed from experiments would be consistent with the predictions from these theories.

6.6.1 Thermal spike model

Thermal spike model was proposed to explain the growth of the cBN phase [Hahn, 1997, Seitz, 1956]. It is not clearly specified whether the theory is applied to the nucleation process of cBN or the growth of cBN grains, which appear at different stages in a deposition process. In this section, we attempt to investigate whether the theory can be able to explain the features of the sp^3 nanoclusters as observed experimentally. We calculate the size of a thermal spike as predicted from the theory to see whether it is comparable with the average size of a nanocluster in our sample.

An ion intrudes into the film surface and collides with the atoms along its track. The kinetic energy Q is consumed to create a local disturbance of the surrounding atoms (thermal spike) and is converted into the vibration energy of the atoms. The local temperature rises drastically, and atomic rearrangement occurs subsequently. If the number of rearrangements exceeds the number of atoms in the spike volume, a sp^2 to sp^3 transition would occur. If the condensation is fast enough, a highly disordered structure is formed, in which the coordination number of an atom would be higher or lower than that in a stoichiometric state.

The Fourier's law [Kittel, 1980] describing the energy current density is $J = -D \text{ grad } T$, where $D = C/(\rho c)$ is the diffusion coefficient, C the thermal conductivity, ρ the density, c the special heat and T the temperature. Combining with the continuity equation of energy, one obtains $\partial T / \partial t = D \text{ div (grad } T)$. The solution is:

$$T(r, t) = \frac{Q}{8\pi^{3/2}\rho c} \frac{1}{(Dt)^{3/2}} \exp(\frac{-r^2}{4Dt}) \qquad (6.1)$$

The parameters involved in this equation for the hBN and cBN structures are listed in Table 6.6 respectively. In particular, temperature is a concept in macroscopic scale, and so the distance r in the calculation cannot be smaller than the nearest neighbour distance, i.e. 2.5 and 3.6 Å. The size of thermal spike is estimated by plotting the temperature profiles at different times after the intruding ion stops completely. The results are plotted in Figs. 6.25 and 26 for hBN and cBN with the use of Eq. (6.1). The radius of a thermal spike size is assumed to be equal to the maximum value of r at which the temperature can just reach the melting point of the materials, i.e. $\approx 3000^{\circ}$C.

Table 6.6 Properties of hBN and cBN [Hugh, 1996]

	hBN	cBN
Q (eV)	360	450
c (J/kg·k)	885	510
ρ (kg/m^3)	2100	3490
C (W/m·k)	30	550
D (m^2/s)	$1.61\text{x}10^{-5}$	$3.09\text{x}10^{-4}$
r_o (Å)	2.5043	3.6153

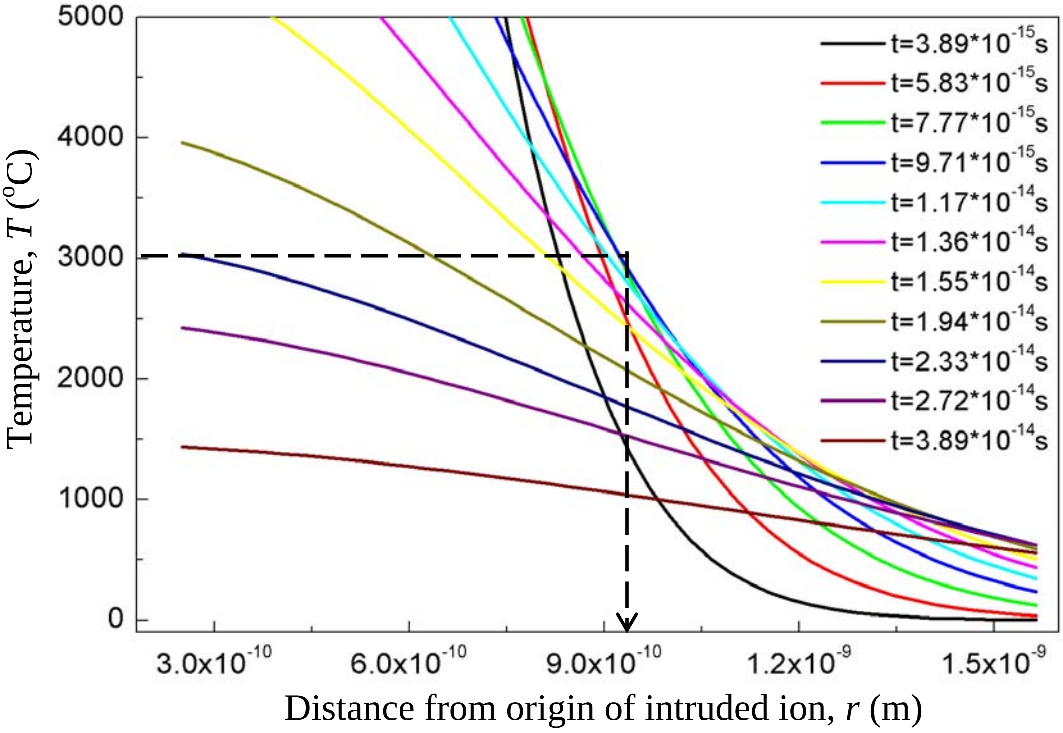

Fig.6.25 Temperature profiles at different times in hBN created by an intruding ion.

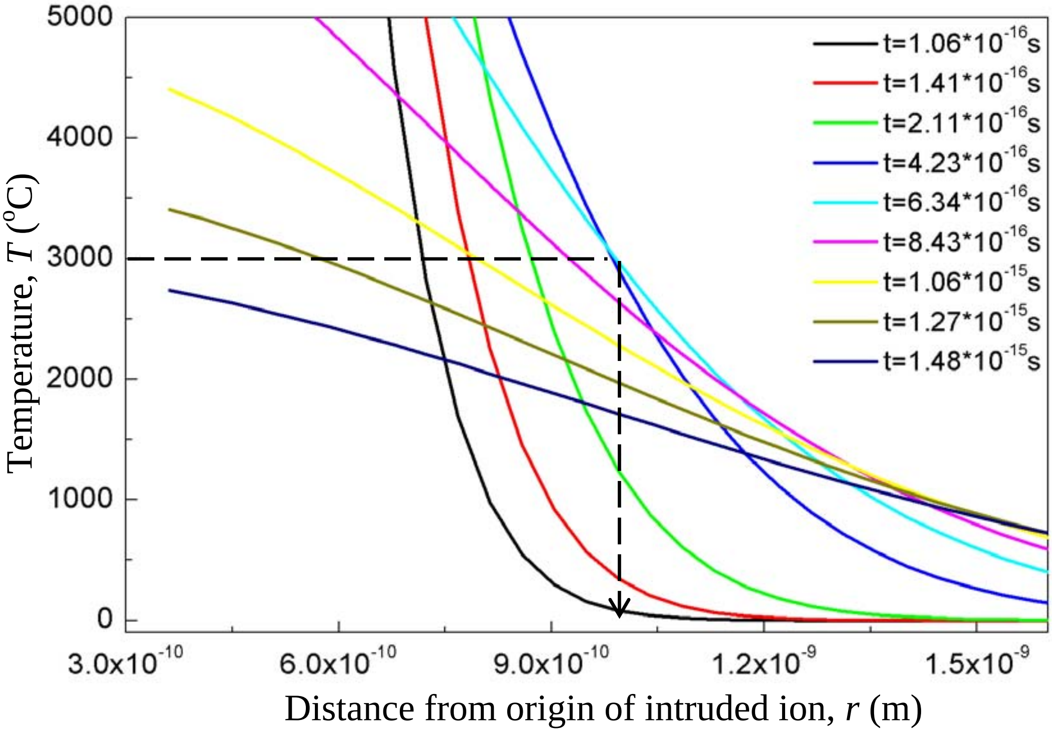

Fig. 6.26 Temperature profiles at different times in cBN created by an intruding ion.

The size of a thermal spike is estimated to be < 2 nm for an ion energy of 360 eV, which is much smaller than the range of the size of the nanoclusters observed, i.e. 7 – 14 nm. In fact, the discrepancy between the small thermal spike size as predicted and a typical cBN grain is widely noticed and is claimed to be the result of a non-zero ionicity of the B-N system [Hahn, 1997]. However, a formal formulation is not worked out yet. It is also claimed that amorphous BN cannot exist [Hahn, 1997], which appears to be different from what we have observed in this study.

The above calculation is for a single ion only, but in our case, the ion current density used for surface assist is so large that the thermal spikes created by the ions would severely overlap. For a 3-cm Kaufman gun and a beam current of 30 mA, the ion flux is 2.65x10^{16} ions cm^{-2} s^{-1}. Hence the distance between two centres of two nearest thermal spikes is ~ 0.07 nm, which is much smaller than the size of a thermal spike predicted theoretically. In fact, the thermal spike theory should predict the formation of a uniform layer because of the severe overlapping of the thermal spikes, and so inconsistent with the fact observed experimentally. In fact, the nanoclusters in the film are separated. Therefore, the thermal spike theory cannot explain the growth mechanism of the sp^3 nanoclusters.

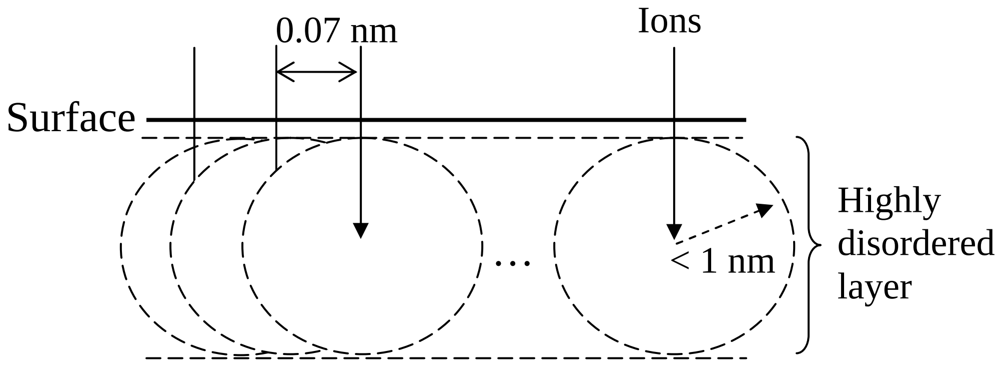

Fig.6.27 Scheme diagram showing severe overlapping of thermal spikes under the real ion assist condition.

6.6.2 Stress model

The stress model is another theory proposed to explain the growth mechanism of the cBN structure [Davis, 1999]. When ion induced stress is accumulated to a threshold volume, the sp^2 basal planes start to buckle and transform to become the (111) planes of the cBN phase. An *ab initio* calculation [Yu, 2003] gives more delicate description of the transitions between four polytypes of BN, name cBN, wurtzite BN (wBN), hBN and rBN. When pressure is applied to the sp^2-bonded basal planes of rBN, arranged in the "A B C A B C...." sequence, the average volume occupied by one atom is reduced from the unstressed state of ~ 8.6 $Å^3$, and the free energy is increased concomitantly. At a pressure ~ 15 GPa, the basal planes start to buckle, and the volume occupied per atom decreases to 6.2 $Å^3$. At this moment, a transition to a dilated cBN structure takes place, which is driven by a drastic reduction in both pressure and free energy. The energy barrier for such a phase transformation is ~ 0.8 eV per atom. The transition would be accompanied by a relaxation of compressive stress in the film, implying that these should be no causal correlation between the presence of hard BN and the presence of a high compressive residual film stress. Transition from the sp^2 hBN structure to the sp^3 wBN could occur based on similar analysis, except that the energy barrier and stress requirement are higher, i.e. ~ 1.4 eV per atom and 30 GPa respectively. However, for thin film case, the difference between the rBN-to-cBN transition and hBN-to-wBN transition is not so clear, because the material is very defective.

It is proposed that the formation of the sp^3 nanoclusters is better explained by the stress model rather than the thermal spike model. We like to point out the following conjectures and suggestions.

(i) The internal stress is built up in a highly dynamic manner with the presence of ion bombardment. As such, fluctuation of stresses may occur. Some local regions may accidentally accumulate sufficiently pressure to initiate the transition to the sp^3 structure. This explains why the nanoclusters observed are distributed separately rather than having a uniform sp^3 bonded layer.

(ii) According to Yu's theory [Yu, 2003], compressive stresses would be released associated with the sp^2-to-sp^3 transition. One may imagine that such a stress relaxation process occurs at the region surrounding a nanocluster at the moment when it is formed. This process limits the maximum size of a nanocluster in the range of 7 – 14 nm as observed.

(iii) The sp^3 nanoclusters are more or less metastable according to the annealing experiments. The temperature and pressure dependences of the free energy of such a metastable state are in general not the same as that of the thermal equilibrium state, and could be at some local minima related to a highly disordered sp^3 atomic network. Once it is heated and surpasses some small potential barrier, the material would transit towards the sp^2 structure.

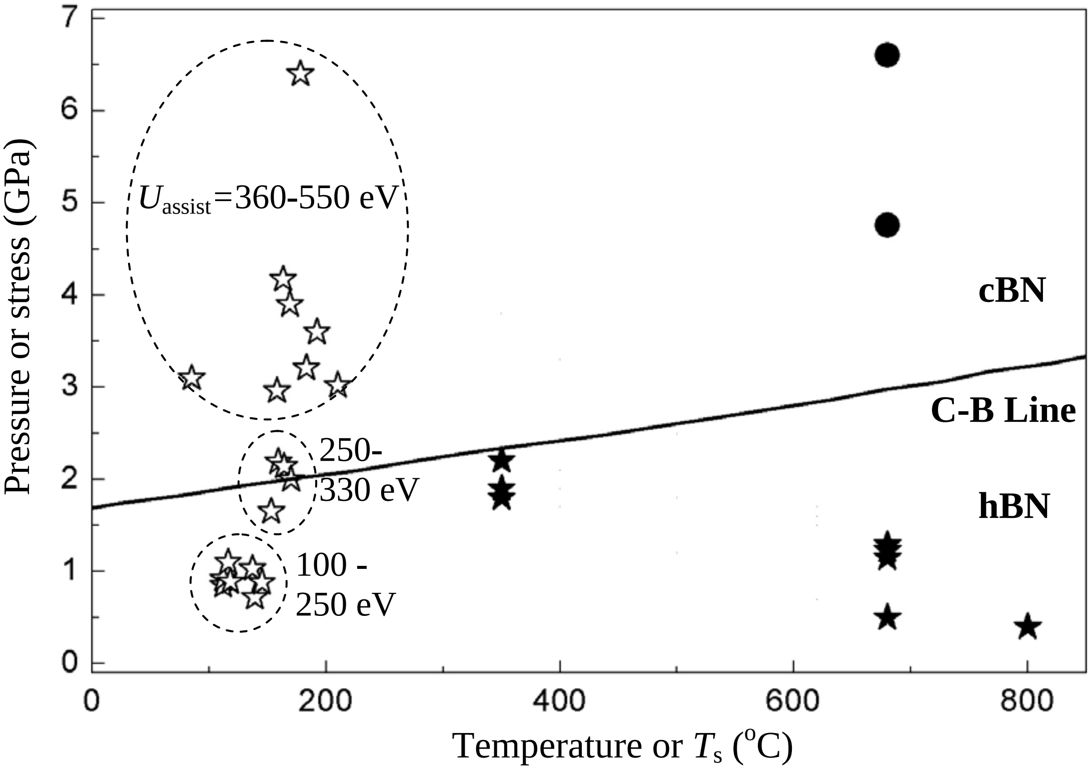

Fig. 6.28 Plot of the stress and substrate temperature of film samples in the P-T phase diagram of the B-N system. ☆ : Samples deposited at unheated conditions (with sp^3 nanoclusters for U_{assist} = 360-550 eV); ★: mainly sp^2 BN; ●: mainly polycrystalline cBN.

Chapter 7

Conclusions

In this project, several deposition schemes were designed and used in a logical sequence for the purposes of (i) fabricating and characterizing thick cBN-rich films with acceptable adhesion to substrates; (ii) investigating the possible mechanisms resulting in the microstructures as observed; and (iii) exploring the possibility of forming non-crystalline sp^3-bonded BN phase which has not been reported by other authors in this field.

In the study, a dual ion beam deposition (DIBD) technique was used to prepare samples. The film structure and composition were investigated by using IR absorption, XPS and TEM techniques. In addition, EELS analysis with the use of XPS and TEM systems were conducted. The EELS(XPS) technique is further developed in the study to quantitatively analyse the volume concentrations of different BN phases in a film sample, by assuming that a BN film would normally consist of a cBN phase, a hBN phase, and an aBN phase. This method was shown to be effective, especially in detecting nano-sized sp^3 structure. EELS(TEM) is important to verify the presence of nano-sized non-crystalline BN phase in a region as tiny as 1 nm. The mechanical properties were studied with the use of nanoindentation techniques and stress measurements through the determination of the radius of curvature of the film.

The major results obtained from the four deposition schemes are summarized as follows:

1. Single-step process

   We applied a single-step process to fabricate boron nitride films in which all the parameters were not changed during the deposition. The purpose was to show the widely reported maximum sustainable thickness of cBN-rich films with good adhesion to substrates, i.e. 200 nm. Results shows that the maximum sustainable thickness of the cBN-rich films prepared by our own DIBD system is 183 nm, confirming that the finding agrees with that reported in the literature.

2. Multilayered deposition process

   We deposited a gradient sp^2-bonded BN buffer layer with thickness 480 nm on the substrate prior to the deposition of a cBN-rich layer in order to increase the maximum sustainable thickness of the cBN-rich layer. It was found that the addition of a buffer layer and the use of appropriate assist ion beam energy were helpful to support a much thicker cBN-rich layer on top. The thickest cBN-rich layer achieved was 643 nm thick, and the film did not peel off over year after deposition. The cBN content in this layer is 87 vol.%, and the hardness is 57 GPa. We suggest that the thick gradient sp^2-bonded BN buffer is relatively deformable, and hence some stresses would be released during the growth of the cBN-rich top layer so as to allow a thicker cBN-rich layer with acceptable adhesion to grow on top. In addition, the optimum assist beam energy was identified to be 450 eV (at 680^{o}C). The growth process was affected by both the generation and annihilation of defects. A 2 nm thick sp^2 BN layer was found to appear on the growth front of the cBN-rich layer, which can be removed by 100-

eV ion irradiation. This result illustrates that the growth of the cBN-rich layer is actually a joint result of defect generation, ion annealing and resputtering processes.

3. <u>An advanced multilayer process with subsequent annealing process</u>

   This process was proposed to deal with three major reasons causing the poor adhesion of a cBN-rich film. They are (i) the appearance of a weak sp^2-bonded BN layer prior to the cBN nucleation; (ii) high compressive stresses that evolve during the deposition of the cBN-rich layer, and (iii) possible existence of excessive B causing reaction of the film materials with the moisture in the atmosphere. The process was designed to produce a layered structure of cBN-rich layer/gradient buffer layer/Zr/substrate, which was then post-annealed at 850^{o}C for 60 minutes in order to drive the reaction between the gradient buffer layer and Zr layer. Results of the XPS depth profile analyses and TEM analyses showed that the zirconium reacted with the sp^2-bonded buffer layer completely to from a zirconium boride / zirconium nitride composite. This result indicates the success of removing the sp^2-bonded layer via solid-state reaction.

4. <u>Ion assist deposition of film on unheated substrates</u>

   It was found that the film deposited on unheated substrates using an assist beam energy U_{assist} exceeding a threshold ≈ 360 eV was a composite containing sp^3 nanoclusters with sizes of 7-14 nm. The nanoclusters are embedded in a sp^2-bonded BN matrix. To characterize the samples, IR absorption was not sensitive enough to detect the nano-sized sp^3 clusters. However, the presence of sp^3 nanoclusters was verified by the results of high resolution TEM, EELS(XPS) data, EELS(TEM) data, hardness and stress measurements. In particular, the sp^3

content is over 30 vol.%, and the hardness is 20 GPa, as compared to 0.9 GPa for pure sp^2-bonded BN. The study of the dependence on the film structure on the assist beam energy (U_{assist}) and substrate temperature (T_{s}) verified that (i) at low U_{assist} (100 – 250 eV), the films were sp^2-bonded, and no sp^3 structure was found; (ii) at low T_{s} and when U_{assist} exceeded a threshold of $\approx$ 360 eV, sp^3 nanoclusters started to appear; (iii) with a mild increase in T_{s} the formation of sp^3 nanoclusters was suppressed in accordance with the P-T phase diagram of the B-N system, or with further increase in U_{assist} the content of sp^3 structure dropped because of the damages induced by severe ion bombardment; (iv) at higher T_{s} and U_{assist}, the formation of sp^3 structure entered another mode, namely, massive nucleation followed by the growth of cBN grains. The sp^3 nanocluster is a new BN phase which has not been reported by others. It was found to be partially thermal unstable, since after annealing in the temperature range of 200 – 850$^{\text{o}}$C, both the internal stress and hardness dropped but they were higher than the values of the films deposited at the same U_{assist} and at the temperature equal to the annealing temperature. According to the temperature distribution described in the thermal spike model, the size of these grains was found to be around 2 nm. However, the bombarding ions density was very high; the separation between two ions was ~ 0.07 nm which was much smaller than the thermal spike size. Thus, the thermal spike model is not suitable to be used to explain the formation of the sp^3 nanoclusters. Instead, the stress model seems to be more suitable for explaining the formation of the nanoclusters observed.

References

Anderson, P.M., Foecke, T. and Hazzledine, P.M. “Dislocation-based deformation mechanisms in metallic nanolaminates”. *MRS Bulletin*, Vol. 24, pp.27-33 (1999).

Banhart, F., Zwanger, M. and Muhr, H.-J. “The formation of curled concentric-shell clusters in boron nitride under electron irradiation” *Chemical Physics Letters*, Vol. 231, pp.98-104 (1994).

Benko, E., Morgiel, J., Czeppe, T. and Barr, T. “Microstructure and hardness of cBN-Zr Composite”. *Journal of the Europen Ceramic Society*, Vol. 18, pp.389-393 (1998).

Brazhkin, V.V., Lypin, A.G. and Hemley, R.J. “Harder than diamond: dreams and reality”. *Philosophical Magazine A*, Vol. 82, pp.231-253 (2002).

Cardinal, G.F., Medlin, D.L., Mirkarimi, P.B., McCarty, K.F. and Howitt, D.G. “Orientation-dependence of elastic strain energy in hexagonal and cubic boron nitride layers in energetically deposited BN films”. *Journal of Vacuum Science and Technology A*, Vol. 15, pp.196-200 (1997).

Cardinale, G.F., Mirkarimi, P.B., McCarty, K.F., Klaus, E.J., Medlin, D.L., Clift, W.M. and Howitt, D.G. “Effects of ambient conditions on the adhesion of cubic boron nitride films on silicon substrates”. *Thin Solid Films*, Vol. 253, pp.130-135 (1994).

Carvalho, S., Rebouta, L., Cavaleiro, A., Rocha, L.A., Gomes, J. and Alves, E. “Microstructure and mechanical properties of nanocomposite (Ti, Si, Al)N coatings”. *Thin Solid Flms*, Vol. 398-399, pp. 391-396 (2001).

Chen, Y.-H., Kitty Lee, W., Chiou, W.-A., Chung, Y.-W. and Leon Keer, M. “Synthesis and structure of smooth, superhard TiN/SiNx multilayer coatings with an equiaxed microstructure” *Surface and Coating Technology,* Vol. 146-147, pp.209-214 (2001).

Collazo-Davila, C., Bengu, E., Leslie, C. and Marks, L.D. “Formation of BN nanoarches: Possibly the key to cubic boron nitride film growth.” *Applied Physics Letters*, Vol. 72, pp.314-316 (1997).

Collazo-Davila, C., Bengu, E., Marks, L.D. and Kirk, M. “Nucleation of cubic boron nitride thin films”. *Diamond and Related Material*, Vol. 8 pp.1091-1100 (1999).

Corrigan, F.R. and Bundy, F.P. “Direct transitions among the allotropic forms of boron nitride at high pressures and temperatures”. *The Journal of Chemical Physics*, Vol. 63, pp.3812-3820 (1975).

Davis, C.A. “A simple model for the formation of compressive stress in thin films by ion bombardment”. *Thin Solid Films*, Vol. 226, pp.30-34 (1993).

Djouadi, M.A., Mortet, V., Khandozhko, S., Jouan, P.Y. and Nouet G. “Dynamic stress investigations for cubic boron nitride films deposited by triode sputtering technique”. *Surface and Coatings Technology*, Vol. 142-144, pp.899-905 (2001).

Donner, W., Dosch, H., Ulrich, S., Ehrhardt, H. and Abernathy D. “Strain relaxation of boron nitride thin films on silicon”. *Applied Physics Letters*, Vol. 73, No. 6, pp.777-779 (1998).

Feldermann, H., Merk, R. and Hofsäss, H. “Room temperature growth of cubic boron nitride”. *Applied Physics Letters*, Vol. 74, No.11, pp.1552-1554 (1999).

Fitz, C., Fukarek W. and Möller, W. “Stress relaxation and phase stability of cubic boron nitride films during ion post implantation and annealing”. *Thin Solid Films*, Vol.408, pp155-159 (2002).

Guiot, E., Benayoun, S., Nouet, G., Djoudi, M., Masri, P. and Lambertin, M. “Formation and growth of cBN films in various conditions: improvement of the adherence”. *Diamond and Related Materials*, Vol. 10, pp.1357-1362 (2001).

Hahn, J., Richter, F., Pintaske, R., Röder, M., Schneider, E. and Welzel, Th. “Formation of c-BN thin films under reduced ion impact”. *Surface and Coatings Technology*, Vol. 92, pp.129-134 (1997).

Helmersson, U., Todorova, S., Barnett, S.A., Sundgren, J.-E., Markert, L.C. and Greene, J.E. “Growth of single-crystal TiN/VN strained-layer superlattices with extremely high mechanical hardness". *Journal of Applied Physics*, Vol. 62, pp.481-484 (1987).

Hofsäss, H., Feldermann, H., Eyhusen, S. and Ronning, C. "Fundamental role of ion bombardment for the synthesis of cubic boron nitride films". *Physical Review B*, Vol. 65, article 115410 (2002).

Hofsäss, H., Feldermann, H., Merk, R., Sebastian, M. and Ronning, C. "Cylindrical spike model for the formation of diamondlike thin films by ion deposition". *Applied Physics A*, Vol. 66, pp.153-181 (1998).

Hofsäss, H., Ronning, C., Griesmeier, U. and Gross, M. "Cubic boron nitride films grown by low energy B^+ and N^+ ion beam deposition". *Applied Physics Letters*, Vol. 67, No. 1, pp.46-48 (1995).

Hofsäss, H., Ronning, C., Griesmeier, U., Gross, M., Reinke, S., Kuhr, M., Zweck, J. and Fischer, R. "Characterization of cubic boron nitride films grown by mass separated ion beam deposition". *Nuclear Instruments and Methods in Physics Research Section B: Beam Interactions with Materials and Atoms*, Vol. 106, pp.153-158 (1995).

Hugh, O. and Pierson "Covalent Nitrides: Properties and General Characteristics". *Handbook of refractory carbides and nitrides properties: Characteristics, processing and Applications*, Noyes Publications, Westwood, N.J., pp.235-247 (1996).

Hui, Y.Y., Wong, K.W. and Lau, W.M. "Quantitative study of ion bombardment induced phae transformation of cubic boron nitride by reflective electron energy-loss spectroscopy". *Journal of Vacuum Science and Technology A*, Vol. 20, pp.1774-1778 (2002).

Ichiki, T., Amagi, S. and Yoshida, T. "Initial stage of cubic boron nitride film growth from vapor phase". *Journal of Applied Physics*, Vol. 79, pp.4381-4387 (1996).

Ilias, S., Stambouli, V., Pascallon, J., Bouchier, D. and Nouet, G. "Microstructure and stress investigations of cubic boron nitride thin films" *Diamond and Related Materials*, Vol. 7, pp.391-396 (1998).

Inagawa, K., Watanabe, K., Saitoh, K., Yuchi, Y. and Itoh, A. "Structure and properties of cBN film deposited by activated reactive evaporation with a gas activation nozzle". *Surface and Coatings Technology*, Vol. 39/40, pp.253-264 (1989).

Johansson, M.P., Ivanov, I., Hultman, L., Münger, E.P. and Schütze, A. "Low-temperature deposition of cubic BN:C films by unbalanced direct current magnetron sputtering of a B_4C target". *Journal of Vacuum Science and Technology A*, Vol.14, No.6, pp.3100-3107 (1996).

Kester, D.J., Ailey, K.S. and Davis, R.F. "Deposition and characterization of boron nitride thin films". *Diamond and Related Materials,* Vol. 3, pp.332-336 (1994).

Kester, D.J., Ailey, K.S., Davis, R.F. and More, K.L. "Phase evolution in boron nitride thin films". *Journal of Materials Research,* Vol. 8, pp.1213-1216 (1993).

Keunecke, M., Yamamoto, K. and Bewilogua, K. "Mechanical and tribological properties of cBN films on silicon and tungsten carbide substrates". *Thin Solid Films,* Vol. 398-399, pp.142-149 (2001).

Kim, I.H., Kim, S.H. and Kim, K.B. "Delamination mechanism in relation to adhesion of cubic boron nitride". *Journal of Vacuum Science and Technology A*, Vol. 16, No. 4, pp.2295-2299 (1998).

Kittel, C. and Kroemer, H. *Thermal Physics, 2nd edition*, W.H. Freeman and Company, San Francisco, pp.389-438 (1980).

Klett, A., Freudenstein, R. and Kulish, W. "Dependence of the stress of c-BN films on the major deposition parameters: theoretical and experimental studies" *Thin Solid Films*, Vol. 398-399, pp.130-136 (2001).

Kulisch, W. and Ulrich, S. "Parameter spaces for the nucleation and the subsequent growth of cubic boron nitride films". *Thin Solid Films,* Vol. 423, pp.183-195 (2003).

Kulisch, W., Freudenstein, R., Klett, A. and Plass, M.F. "A concept for the deposition of adherent cubic boron nitride films". *Thin Solid Films*, Vol. 377-378, pp.170-176 (2000).

Li, Q., Bello, I., Marks, L.D., Lifshitz, Y. and Lee, S.T. "Orientation effects in tBN / cBN interfaces: A transmission electron microscopic study". *Applied Physics Letters,* Vol. 80, No. 1, pp.46-48 (2002).

Li, Q., Marks, L.D., Lifshitz, Y., Lee, S.T. and Bello, I. "Controlling the nucleation environment of cBN films and their related properties". *Physical Review B*, Vol. 65, article 045415 (2002).

Li, Q., Zhang, R.Q., Marks, L.D., Zhang, W.J. and Bello, I. “Reactivity of different tBN environments serving as reaction sites in cBN film deposition”. *Diamond and Related Materials*, Vol. 11, pp.1416-1421 (2002).

Lifshitz, Y., Kasi, S.R. and Rabalais, J.W. “Subplantation model for film growth from hyperthermal species: Application to Diamond”. *Physical Review Letters*, Vol. 62, No. 11, pp.1290-1293 (1989).

Lifshitz, Y., Kasi, S.R. and Rabalais, J.W. “Subplantation model for film growth from hyperthermal species”. *Physical Review B*, Vol. 41, pp.10468-10480 (1990).

Litvinov, D. and Clarke, R. “In situ texture monitoring for growth of oriented cubic boron nitride films”. *Applied Physics Letters*, Vol. 74, No. 7, pp.955-957 (1999).

Litvinov, D. and Clarke, R. “Reduced bias growth of pure-phase cubic boron nitride”. *Applied Physics Letters*, Vol. 71, No. 14, pp.1969-1971 (1997).

Litvinov, D., Taylor II, C.A. and Clarke, R. “Semiconducting cubic boron nitride”. *Diamond and Related Materials*, Vol. 7, pp.360-364 (1998).

Loh, K. P., Sakaguchi, I., Nishitani-Gamo, M., Taniguchi, T. and Ando, T. “Surface structure of single-crystal cubic boron nitride (111) studied by LEED, EELS, and AES”. *Physical Review B*, Vol. 56, pp.R12791-R12794 (1997).

Loh, K.P., Sakaguchi, I. and Nishitani-Gamo, M. “Hydrogen-induced surface structuring of a cubic boron nitride (100) face studied by low-energy electron diffraction and electron spectroscopic techniques”. *Physical Review B*, Vol. 57, pp. 7266-7274 (1998).

Makowiecki, D.M., Jankowski, A.F., McKernan, M.A. and Foreman, R.J. “Magetron sputtered boron films and Ti/B multilayer structures”. *Journal of Vacuum Science and Technology A*, Vol. 8, pp.3910-3913 (1990).

Matsumoto, S. and Zhang, W. “High-rate deposition of high-quality, thick cubic boron nitride films by bias-assisted DC jet plasma chemical vapor deposition”. *Japanese Journal of Applied Physics*, Vol.39, pp.L442-L444 (2000).

Matsumoto, S. and Zhang, W. “The introducing of fluorine into the deposition of BN: a successful method to obtain high-quality, thick cBN films with low residual stress”. *Diamond and Related Materials*, Vol. 10, pp.1868-1874 (2001).

McCarty, K.F. and Medlin, D.L. “How plastic deformation can produce texture in graphitic films of boron nitride, carbon nitride, and carbon” *Diamond and Related Materials*, Vol. 6, pp.1219-1225 (1997).

McKenzie, D.R., Cockayne, D.J.H. and Muller, D.A. “Electron optical characterization of cubic boron nitride thin films prepared by reactive ion plating”. *Journal of Applied Physics*, Vol. 70, No. 6, pp.3007-3012 (1991).

McKenzie, D.R., McFall, W.D., Sainty, W.G., Davis, C.A. and Collins, R.E. “Compressive stress induced formation of cubic boron nitride”. *Diamond and Related Materials*, Vol. 2, pp.970-976 (1993).

Mirkarimi, P.B., McCarty, K.F. and Medlin, D.L. “Review of advances in cubic boron nitride film synthesis”. *Materials Science and Engineering*, R21, pp.47-100 (1997).

Mirkarimi, P.B., McCarty, K.F., Medlin, D.L., Wolfer, W.G., Friedmann, T.A., Klaus, E.J., Cardinale, G.F. and Howitt, D.G. “On the role of ions in the formation of cubic boron nitride films by ion-assisted deposition”. *Journal of Materials Research*, Vol. 9, pp.2925-2938 (1994).

Mirkarimi, P.B., Medlin, D.L., McCarty, K.F., Dibble, D.C. and Clift, W.M. “The synthesis, characterization, and mechanical properties of thick, ultrahard cubic boron nitride films deposited by ion-assisted sputtering”. *Journal of Applied Physics*, Vol. 82, No.4, pp.1617-1625 (1997).

Murakawa, M. and Watanabe, S. “The synthesis of cubic BN films using a hot cathode plasma discharge in a parallel magnetic field”. *Surface and Coatings Technology*, Vol. 43/44, pp.128-136 (1990).

Musil, J. and Poláková, H. “Hard nanocomposite Zr-Y-N coatings, correlation between hardness and structure”. *Surface and Coatings Technology*, Vol. 127, pp.99-106 (2000).

Nix, W.D. “Mechanical properties of thin films”, *Metallurgical Transactions A*, Vol. 20A, pp.2217-2245 (1989).

Oliver, W.C. “An improved technique for determining hardness and elastic modulus using load and displacement sensing indentation experiments”. *Journal of Materials Research*, Vol. 7, No. 6, pp.1564-1583 (1992).

Ong, C.W., Zhao, X.-A., Chan, K.F., Ng, Y.M., Chan, P.W., Choy, C.L. and Kwok, R.W.M. “Effects of carbon incorporation on the structure and mechanical properties of cubic boron nitride films”. *Thin Solid Films*, Vol. 307, pp.152-155 (1997).

Panayiotatos, Y., Logothetidis, S., Handrea, M. and Kautek, W. “Homogeneous and amorphous sputtered sp^3-bonded BN films at RT: a stress, spectroscopic ellipsometry and XPS study”. *Diamond and Related Materials*, Vol. 12, pp.1151-1156 (2003).

Panayiotatos, Y., Patsalas, P., Charitidis, C. and Logothetidis, S. “Mechanical performance and growth characteristics of boron nitride films with respect to their optical, compositional properties and density”. *Surface and Coatings Technology*, Vol. 151-152, pp.155-159 (2002).

Park, K.S., Lee, D.Y., Kim K.J. and Moon, D.W. “Growth mechanism of cubic boron nitride thin films by ion beam assist sputter deposition”. *Journal of Vacuum Science and Technology A*, Vol. 15, pp.1041-1047 (1997).

Qian, Z. and Shi, J.L. “Characterization of pure and doped zirconia nanoparticles with infrared transmission spectroscopy”. *Nanostructured Materials*, Vol. 10, pp.235-244 (1998).

Rebouta, L., Tavares, C.J., Aimo, R., Wang, Z., Pischow, K., Alves, E., Rojas, T.C. and Odriozola, J.A. “Hard nanocomposite Ti-Si-N coatings prepared by DC reactive magnetron sputtering”. *Surface and Coatings Technology*, Vol. 133-134, pp. 234-239 (2000).

Reinke, S., Kuhr, M. and Kulisch, W. “Mechanisms in ion induced c-BN growth”. *Diamond and Related Materials*, Vol. 3, pp.341-345 (1994).

Reinke, S., Kuhr, M., and Kulisch, W. “Investigation of stress and adhesion of cubic boron nitride films”. *Diamond and Related Materials,* Vol. 5, pp.508-513 (1996).

Reinke, S., Kuhr, M., Kulisch, W. and Kassing, R. “Recent results in cubic boron nitride deposition in light of the sputter model”. *Diamond and Related Materials*, Vol. 4, pp.272-283 (1995).

Riedel, R. “Novel ultrahard materials”. *Advanced materials,* Vol. 6, No.7/8 (1994).

Robertson, J. “Deposition mechanism of cubic boron nitride”. *Diamond and Related Materials,* Vol. 5, pp.519-524 (1996).

Schütze, A., Bewilogua, K., Lüthje, H., Kouptsidis, S. and Jäger, S. “Cubic boron nitride films prepared by reactive r.f. and d.c. sputtering from different boron containing targets”. *Surface and Coatings Technology*, Vol. 74-75, pp.717-722 (1995).

Seitz, F. and Koehler, J.S. “Displacement of atoms during Irradiation”. *Solid State Physics: Advances in Research and Applications,* Vol. 2, pp.305-442 (1956).

Shinn, M., Hultman, L. and Barnett, S.A. “Growth, structure, and microhardness of epitaxial TiN/NbN superlattices”. *Journal of Materials Research,* Vol. 7, pp.901-911 (1992).

Takamura, Y.Y., Tsuda, O., Ichinose, H. and Yoshida, T. “Atomic-scale structure at the nucleation site of cubic boron nitride deposited from the vapor phase”. *Physical Review B,* Vol. 59, No. 15, pp.10351-10355 (1999).

Tarrio, C. and Schnatterly, S.E. “Interband transitions, plasmons, and dispersion in hexagonal boron nitride”. *Physical Review B*, Vol. 40, No. 11, pp.7852-7859 (1989).

Tougaard, S. “Quantitative analysis of the inelastic background in surface electron spectroscopy”. *Surface and Interface Analysis,* Vol.11, pp.453-472 (1988).

Tougaard, S. “Universality Classes of Inelastic Electron Scattering Cross-sections”. *Surface and Interface Analysis*, Vol.251, pp.137-154 (1997).

Tougaard, S. and Chorkendorff, I. “Differential inelastic electron scattering cross sections from experimental reflection electron-energy-loss spectra: Application to background removal in electron spectroscopy”. *Physical Review B,* Vol.35, pp.6570-6577 (1987).

Tougaard, S. and Kraaer, J. “Inelastic-electron-scattering cross sections for Si, Cu, Ag, Au, Ti, Fe, and Pd”. *Physical Review B*, Vol.43, pp.1651-1611 (1991).

Trehan, R., Lifshitz, Y. and Rabalais, J.W. “Auger and X-ray electron spectroscopy studies of hBN, cBN, and N_2^+ ion irradiation of boron and boron nitride”. *Journal of Vacuum Science Technology A*, Vol. 8, No. 6, pp.4026-4032 (1990).

Ulrich, S., Scherer, J., Schwan J., Barzen, I., Jung, K. and Ehrhardt, H. “Radio frequency ion plating-induced phase transition from h-BN to nanocrystalline c-BN”. *Diamond and Related Materials*, Vol. 4, pp.288-291 (1995).

Vepřek, S. and Reiprich, S. “A concept for the design of novel superhard coatings”. *Thin Solid Films*, Vol. 268, pp.64-71 (1995).

Vepřek, S., Haussmann, M. and Reiprich, S. “Superhard nanocrystalline W_2N/amorphous Si_3N_4 composite materials”. *Journal of Vacuum Science and Technology A*, Vol. 14, pp.46-51 (1996).

Vepřek, S., Niederhofer, A., Moto, K., Bolom, T., Männling, Nesladek, P., Dollinger, G. and Bergmaier, A. “Composition, nanostructure and origin of the ultrahardness in nc-TiN/a-Si_3N_4/a- and nc-$TiSi_2$ nanocomposities with H_v = 80 to $\geq$ 105 GPa”. *Surface and Coatings Technology*, Vol. 133-134, pp.152-159 (2000).

Walter, H., Bewilogua, K., Schütze, A. and Maassen, T. “Improvement of the adhesion of sputter-deposited cubic boron nitride films”. *Diamond and Related Materials*, Vol. 8, pp.110-113 (1999).

Weertman, J.R., Farkas, D., Hemker, K., Kung, H., Mayo, M., Mitra, R. and Swygenhoven, H.V. “Structure and mechanical behaviour of bulk nanocrystalline materials”. *MRS Bulletin*, Vol. 24, pp.44-50 (1999).

Weissmantel, S and Reisse, G. “Pulsed laser deposition of cubic boron nitride films at high growth rates”. *Diamond and Related Materials*, Vol. 10, pp.1973-1982 (2001).

Widmayer, P., Ziemann, P., Ulrich, S. and Ehrhardt, H. “Phase stability and stress relaxation effects of cubic boron nitride thin films under 350 keV ion irradiation”. *Diamond and Related Materials*, Vol. 6, pp.621-625 (1997).

Windischmann, H. “Intrinsic stress in sputtered thin films”. *Journal of Vacuum Science and Technology A*, Vol. 9, pp.2431-2436 (1991).

Xu, Y.N., Ching, W.Y. “Calculation of ground-state and optical properties of boron nitrides in the hexagonal, cubic, and wurtzite structures”. *Physical Review B*, Vol. 44, pp.7787-7798 (1991).

Yamada-Takamura, Y., Tsuda, O., Ichinose, H. and Yoshida, T. “Atomic-scale structure at the nucleation site of cubic boron nitride deposited from the vapour phase”. *Physical Review B*, Vol. 59, pp.10351-10355 (1999).

Yang, H.S., Iwamoto, C. and Yoshida, T. "Nanostructures of the turbostratic BN transition layer in cubic BN thin films deposited by low-pressure inductively coupled plasma-enhanced chemical vapor deposition". *Journal of Applied Physics*, Vol. 91, No. 10, pp.6695-6699 (2002).

Yu, W.J., Lau, W.M., Chan, S.P, Liu, Z.F. and Zheng, Q.Q. "*Ab initio* study of phase transformations in boron nitride". *Physical Review B*, Vol. 67, 014108 (2003).

Zhao, X.-A., Ong, C.W., Chan, K.F., Ng, Y.M., Tsang, Y.C., Choy, C.L. and Chan, P.W. "Physical properties of dual ion beam deposited $(B_{0.5-x}Si_x)N_{0.5}$ films". *Journal of Vacuum Science and Technology A*, Vol. 15, No. 4, pp.2297-2306 (1997).

Appendix

Sample Tables

Table 1: Films / Si; $T_s = 680^oC$

Sample	I_{spu} / U_{spu} (mA / eV)	I_{assist} / U_{assist} (mA / eV)	t (min)	d (nm)	$\eta_{cBN\text{-}IR}$ (vol.%)	H (GPa)	E (GPa)	Coating rate (nm min^{-1})
cBN009	70/1200	30/450	5	19	22	10.7	153.3	3.80
cBN008	70/1200	30/450	10	27	29	10.9	162.9	2.70
cBN007	70/1200	30/450	30	183	43	23.7	233.7	6.10
cBN006	70/1200	30/450	60	362	56	Peel-off		6.03
cBN005	70/1200	30/450	90	507	64	Peel-off		5.63
cBN004	70/1200	30/450	120	658	65	Peel-off		5.48

Table 2: Films / sp^2 buffer / Si; $T_s = 680^oC$

Sample	I_{assist} (mA)	U_{assist} (eV)	$t_{buf}/t_{seed}/t_{top}$ (min)	d_{buf} /d_{seed} /d_{top} (nm)	$\eta_{cBN\text{-}IR}$ (vol.%)	$\sigma_{top}/H_{top}/E_{top}$ (GPa)
cBN013	20/30/30	(200;280;360) /450/250	(10;10;10) /30/90	279/80/1044	0	1.29/3.4/95
cBN017	20/30/30	(200;280;360) /450/300	(10;10;10) /30/90	279/80/830	0	1.23/3.3/89
cBN020	20/30/30	(200;280;360) /450/360	(10;10;10) /30/90	279/80/607	81	7.99/60/730
cBN003	20/ 30	(200;280;360) /450	(10;10;10) / 120	279/ 510	70	6.59/44/587
cBN018	20/30/30	(200;280;360) /450/550	(10;10;10) /30/90	279/80/274	50	4.76/28/372

Table 3: Film / Zr / WC + Annealing; $T_\mathrm{s} = 680^{\mathrm{o}}$C

Sample	I_assist (mA)	U_assist (eV)	t (min)	d (nm) before annealing	d (nm) after annealing
hBNZr001	--/ (20;20;20)	--/ (200;280;360)	60/ (3;3;4)	Zr:360/ buffer:122	Zr:413/ buffer:68
chBNZr001	--/ (20;20;20)/ 30	--/ (200;280;360)/ 450	60/ (3;3;4)/ 120	Zr:360/ buffer:122/ cBN-rich:479	Zr-rich:755/ buffer:--/ cBN-rich:72

Table 4: Film / unheated Si ; $t = 60$ min

Sample	U_assist (eV)	I_assist (mA)	T_s ($^{\mathrm{o}}$C)	$\eta_\mathrm{cBN\text{-}IR}$ (vol.%)	η_cBN (vol.%)	H (GPa)	σ (GPa)	d (nm)	Coating rate (nm min^{-1})
aBN059	100	20	112	0	---	9.4	0.9	570	9.51
aBN062	125	20	116	0	---	12.4	1.1	591	9.85
aBN031	150	20	112	0	0.0	12	0.9	520	8.67
aBN063	150	20	118	0	---	12.7	0.9	579	9.66
aBN060	175	20	137	0	---	13.3	1.0	686	11.44
aBN058	200	30	139	0	---	13.3	0.7	626	10.43
aBN057	250	30	145	0	---	13.7	0.9	626	10.43
aBN056	300	30	153	0	---	16.8	1.7	578	9.64
aBN061	330	30	159	0	---	19.1	2.2	591	9.85
aBN073	360	30	85	0	---	19.2	3.1	501	8.36
aBN004	360	30	150	0	32.3	20.6	---	350	5.83
aBN030	360	30	158	0	34.5	19.4	3.0	449	7.48
aBN055	360	30	164	0	25.4	17.3	2.1	441	7.34
aBN041	360	40	170	0	32.4	20	2.0	518	8.63
aBN067	360	30	178	0	---	20.5	6.4	758	6.30
aBN039	450	30	163	0	---	23.5	4.2	319	5.31
cBN024	450	30	169	0	29.2	22.9	3.9	298	6.62
aBN064	450	30	183	0	---	16.9	3.2	556	9.26
aBN069	550	30	210	0	---	14.2	3.0	334	5.57

Table 5: Film / Si ; T_s = 350 – 800^{o}C ; t = 60 min

Sample	U_{assist} (eV)	I_{assist} (mA)	T_s (^{o}C)	η_{cBN-IR} (vol.%)	η_{cBN} (vol.%)	H (GPa)	σ (GPa)	d (nm)	Coating rate (nm min^{-1})
cBN013	250	30	680	0	---	3.4	1.3	1044	11.6
cBN017	300	30	680	0	---	3.3	1.2	830	9.22
aBN034	360	30	350	0	13.9	2.1	1.9	259	4.32
aBN043	360	40	350	0	18.3	4	2.2	446	7.44
aBN035	360	30	680	11.7	25.7	4	1.2	207	3.45
aBN042	360	40	680	0	21.6	4.4	0.5	411	6.85
aBN044	360	30	800	0	---	3.7	0.4	352	5.87
aBN038	450	30	350	7.5	26.5	12.4	1.8	284	4.73
cBN007	450	30	680	40.1	49.0	23.7	---	183	6.1
cBN003	450	30	680	70.3	79.7	44.3	6.6	510	4.25
aBN046	450	30	800	29.9	---	1.7	0.4	459	7.64
cBN018	550	30	680	49.6	---	28	4.8	274	3.04